NASA Technical Memorandum 100163

Numerical Simulation of Subsonic and Transonic Propeller Flow

Aaron Snyder
Lewis Research Center
Cleveland, Ohio

April 1988

NASA

NUMERICAL SIMULATION OF SUBSONIC AND TRANSONIC PROPELLER FLOW

Aaron Snyder
National Aeronautics and Space Administration
Lewis Research Center
Cleveland, Ohio 44135

SUMMARY

The numerical simulation of three-dimensional transonic flow about a system of propeller blades is investigated. In particular, it is shown that the use of helical coordinates significantly simplifies the form of the governing equation when the propeller system is assumed to be surrounded by an irrotational flow field of an inviscid fluid. The unsteady small disturbance equation, valid for lightly loaded blades and expressed in helical coordinates, is derived from the general blade-fixed potential equation, given for an arbitrary coordinate system. The use of a coordinate system which inherently adapts to the mean flow results in a disturbance equation requiring relatively few terms to accurately model the physics of the flow. Furthermore, the helical coordinate system presented here is novel in that it is periodic in the circumferential direction while, simultaneously, maintaining orthogonal properties at the mean blade locations. The periodic characteristic allows a complete cascade of blades to be treated, and the orthogonality property affords straightforward treatment of blade boundary conditions. An ADI numerical scheme is used to compute the solution to the steady flow as an asymptotic limit of an unsteady flow. As an example of the method, solutions are presented for subsonic and transonic flow about a 5 percent thick bicircular arc blade of an eight bladed cascade. Both high and low advance ratio cases are computed, and include a lifting as well as nonlifting cases. The nonlifting solutions obtained are compared to solutions from an Euler code.

E-3725

ACKNOWLEDGMENTS

The author gratefully acknowledges the support of the many individuals who were helpful in this commitment. In particular, special recognition is given to Dr. Gerald Englert who contributed much of the fundamental development for Chapter IV. Also, special appreciation is given to Dr. John Adamcyck who first suggested to the author that the small disturbance approach could be applied successfully to solving propeller flow. In addition, Mr. Mark Celestina and Mr. Richard Mulac are acknowledged for their help in providing the Euler solution results, which were used for the comparison solutions. Finally, the author wishes to express his appreciation to his two advisors, Dr. Kenneth DeWitt and Dr. Theodore Keith, both of whom offered helpful guidance and encouragement.

TABLE OF CONTENTS

LIST OF FIGURES

LIST OF TABLES

NOMENCLATURE

A	function relating periodic helical coordinates to Cartesian coordinates
A_i	Jacobian matrix defined in Eq. (3.20)
$A_1, A_2, \ldots, A_8$	coefficients of small disturbance equation, Eq. (7.1)
$\bar{a}$	undisturbed fluid velocity vector in general rotating coordinate system
a_o	nonnegative constant, Eq. (6.9)
B	function relating ξ to z, Eq. (6.3)
C	constant in Eq. (3.5)
$\mathscr{C}$	initial curve
C_1, C_2	constants determining u_1 and u_2 in Eq. (3.5)
C_P	power coefficient
C_T	thrust coefficient
c	speed of sound
D	propeller diameter
$\mathscr{D}$	domain for conservation laws
D_Y	special difference operator in mean flow direction
d, m, n	transonic similarity parameters
E	damping function in helical coordinate system specification, Eq. (6.6)
e	specific internal energy
F	function defining blade surface
F_o, F_u	lower and upper blade functions
F, G	flux vectors of conservation equation
$\bar{f}$	general flux vector

G	general solution to Eq. (3.5)
g	determinant of the metric tensor
g_{ij}, g^{ij}	covariant and contravariant metric tensor components
h	specific enthalpy; blade profile parameter
h_o, h_u	lower and upper blade profiles
J	Jacobian of coordinate transformation; advance ratio of propeller, $J = V/(nD)$
K	transonic similarity parameter, Eq. (3.26)
k	ratio of specific heats
ℓ	blade chord
M	radially dependent Mach number of free-stream
M_R	Mach number of propeller tip at $r = R$
M_T	circumferential Mach number of propeller tip
M_∞	free-stream Mach number for two-dimensional flow
N	number of ADI iterations; general point on grid
N_B	number of blades in cascade
n	rate of revolution of propeller; time step of ADI iteration
$\hat{n}$	outward normal from surface
P, Q, R	variable coefficients of quasi-linear P.D.E.
p	fluid pressure
q	fluid velocity; source distribution
q'	perturbation velocity
R	radius of propeller
r	radius from axis of rotation; second helical coordinate
ρ	radius from origin
S	surface bounding domain
s	directional coordinate; parameter such as arc length varying along characteristic curves

t	time
t_{max}	maximum thickness of blade
Δt_i	time step of ADI at i^{TH}-iteration
Δt_{max}	maximum time step of ADI procedure
Δt_{min}	minimum time step of ADI procedure
U	helical velocity
U_∞	uniform upstream velocity, axial free-stream velocity
u	independent variable in Eq. (3.5)
u,v,w	fluid velocities in x,y,z-directions
u^j	unknown j^{th}-quantity in conservation equation
u_1,u_2	solutions to Eq. (3.5)
V	advance speed of propeller; axial speed of fluid relative to propeller
$\bar{V}$	advance velocity of propeller; relative velocity between inertial and rotating frames
v_s	shock velocity
v_1	velocity inside final slipstream
W	column vector of unknown u^j
X,Y,Z	Cartesian coordinates in inertial frame
x,y,z	Cartesian coordinates in rotating frame
x^1,x^2,x^3	Cartesian coordinates corresponding to x,y,z
y^1,y^2,y^3	helical coordinates corresponding to γ,r,ξ
(Greek)	
α	angle of attack
α_i	angle of incidence
α_o	angle of zero lift
β	advance angle of helical curve
Γ	circulation function

γ, r, ξ	helical coordinates
$\bar{\gamma}, \bar{r}, \bar{\xi}$	uniform computational coordinates
Δ	increment operator
δ	ratio of maximum blade thickness to chord length, $\delta = t_{max}/\ell$
$\delta_\gamma, \delta_{\gamma\gamma}, \ldots, \delta_{r\xi}$	finite difference operators
ε	inverse of blade aspect ratio, $\varepsilon = \ell/R$
ε_I	streamwise switching operator
ε^{ijk}	permutation symbol
η	efficiency
ϑ	circumferential angle about axis
λ	advance ratio, $\lambda = V/(\Omega R)$
λ^+, λ^-	forward and rearward characteristics
υ	diffusion coefficient
ξ_m	half the distance between neighboring blades
$\bar{\xi}$	ξ as measured from nearest blade
π	ratio of circumference of circle to diameter
ρ	fluid density
τ	parameter which is constant along characteristics
Φ	total velocity potential
φ	perturbation velocity potential
Ω	rotational speed of propeller
ω	frequency of airfoil motion

Subscripts and superscripts

I,J,K	nodal indices of computational mesh
i,j,k	indices for tensor quantities
L.E.	leading edge
n,n+1	value at time step n and n+1

net	overall
T.E.	trailing edge
*	value at first intermediate time step
**	value at second intermediate time step
'	derivative of quantity

Special symbols

0+	positioned slightly above upper blade surface
0-	positioned slightly below lower blade surface
∇	gradient operator
∇^2	laplacian operator
~	scaled quantity
| |	absolute value
[ ]	jump in quantity across shock

I. INTRODUCTION

The rapid rise of computer capability has greatly influenced the methodology for attacking complex problems in engineering and science. The trend toward the numerical formulation and solution of problems has grown and will undoubtedly expand in the future. In the areas of fluid mechanics and heat transfer, this approach is known as computational fluid dynamics (CFD).

The application of computational fluid dynamics methods toward the simulation of the flow surrounding high-speed propellers is the subject of this work.

Many examples of both steady and unsteady flows of practical interest are well approximated by various forms of the governing equations of fluid mechanics. The recent marked advance in computer capabilities and the rapid growth of efficient and accurate numerical methods have allowed a number of difficult flow problems to be examined.

In the past, analytical and experimental methods were the two main avenues for obtaining aerodynamic solutions. While analytical methods are still being enhanced and often give quick solutions, they suffer the drawback of being limited to simple configurations. On the other hand, wind-tunnel experiments can handle complicated configurations, but are limited to certain flow ranges and require expensive models and extensive test times. Nevertheless, the wind tunnel has served as the primary tool for the development of aerodynamic configurations. Shapes can be tested and modified in light of pressure and force measurements.

Analytical methods are generally limited to simpler isolated components and partially owe their usefulness to the fact that efficient aerodynamics can only be achieved with well ordered flows. Consequently, simplified mathematical models are often adequate replacements for the full set of governing equations. This was utilized with great success in many important applications. For example, often purely inviscid flow assumptions for irrotational flow, in which the velocity can be formulated in terms of a gradient of a scalar, have proven sufficient. However, both the limitations of the analytical techniques as well as the costs of the wind tunnel studies are all too apparent as the features of the flow fields become more complex. This is especially true for the prediction of transonic flows. Thus, a need for alternative solution methods was created.

The growing area of computational fluid mechanics offers an attractive complementary alternative to analytical methods or experimentation by providing details of the flow physics as well as data beyond the experimental range while affording configuration optimization. The use of computational methods to provide solutions about rotating propellers is one illustration of the ability of these techniques to solve a complicated set of nonlinear partial differential equations and associated boundary conditions.

Coinciding with the arrival of increasingly powerful CFD methods, was the emergence of renewed interest in propellers which offer large performance improvements for aircraft that cruise in the high subsonic speed range. The reason for this is that for lifting surfaces, to a first approximation, the efficiency is proportional to the Mach number of the approaching flow times the lift to drag ratio. The lift to drag

ratio rises monotonically with Mach number until a sharp drop-off occurs at high subsonic free-stream Mach numbers. Thus, it pays to increase the speed as much as possible until losses associated with increased drag become prohibitive.

The very high propulsive efficiencies of the advanced free air propeller coupled with the need to reduce fuel costs has led to a rebirth in propeller research programs. These programs have introduced changes that have altered advanced high-speed turboprops considerably from their low-speed turboprop counterparts. The most notable changes are the use of eight to ten thin, highly swept, small-diameter blades instead of two to four longer, thicker, and unswept conventional blades. These changes allow propellers to operate efficiently in the transonic flow regime. However, they require sophisticated computational methods in order to predict and calculate their aerodynamic characteristics. This is mainly due to the increased three-dimensionality of the flow field encompassing these low aspect ratio blades and to the rise of mathematical nonlinearity in the flow model which is associated with their transonic tip speeds. Also, their thin structural design makes the blades prone to flutter. This is a source of unsteadiness which must be considered in addition to the inherent unsteadiness of the transonic regime.

Improvements in present techniques are needed to provide accurate solutions for unsteady three-dimensional transonic flows about propellers. The use of numerical methods offers the potential for solving complex equations in intricate geometries such as those which exist in the case of simulating flow about rotating propeller blades. However, as with any method, limits exist on the capabilities. These

limits involve the speed and memory of the computers and the availability of efficient algorithms as well as considerations of robustness and affordability. For a given problem, judgment dictates the trade-off between the suitability of a particular model and the feasibility of the calculation. This is very much the same dilemma as faced when using a theoretical approach.

It is generally accepted that the full Navier-Stokes equations, which satisfy conservation of mass, momentum and energy in a viscous heat conducting fluid, provide a complete description of most flows of interest to CFD. The unsteady compressible Navier-Stokes equations are a mixed set of hyperbolic-parabolic equations; for unsteady incompressible flow they are a mixed set of elliptic-parabolic equations; for steady compressible flow, they are a set of hyperbolic-elliptic equations. In the latter case, due to the effect of the different character of the numerical schemes required for hyperbolic and elliptic terms, the equations are often cast in the unsteady form and marched to a steady solution. At high Reynolds number, the unsteady compressible Navier-Stokes equations are difficult to solve due to the large difference in magnitude between the inertial and viscous forces. The large inertial forces of the hyperbolic terms can impose small time steps in order to meet accuracy or stability requirements. This time-step limitation generally severely retards the effects of viscosity associated with the parabolic terms of the equation. The consequence is that excessive computer time is needed to resolve the flow.

The solution of the Navier-Stokes equations for general three-dimensional, time-dependent, turbulent flow is a distant goal. Candidates for the near future include certain averaged forms of the

Navier-Stokes equations. The one most likely to find application to aerodynamics is the Reynolds-averaged form. Here the the turbulent terms are averaged with respect to time and the stresses are determined by empirical closure formulas. Other more advanced forms of modeling exist such as the large eddy simulation model. In this case the full time-dependent Navier-Stokes equation is used to calculate the development of large scale turbulent eddies. These eddies are anisotropic and highly structured. A process analogous to Reynolds averaging is used to model the subscale turbulence. Although interesting results have been reported, computational time for the solution of either the Reynolds averaged model or large eddy simulation model is exorbitant for general use.

Current progress in aerodynamic design has relied mainly on the approach fostered by Prandtl, whereby viscous effects can be considered to be confined to a relatively thin region, called a boundary layer, adjacent to solid surfaces and their wakes; the entire remaining external flow can be regarded as being inviscid. This method effectively splits the flow into two distinct but coupled regions. The forms of the governing equations have quite different characteristics and demand different solution methods. This allows a considerable savings in computer time and storage since all the viscous terms are neglected in the inviscid region and only the viscous terms normal to the wall are retained in the boundary layer. In addition, the momentum equation is simplified in the viscous region and as a consequence the normal pressure gradient is neglected. Special boundary-layer type marching techniques are available which offer additional savings in computation time and storage. Much attention has been focused on

providing the correct representation of the viscous-inviscid coupling and the proper matching of their solutions at the interface of the regions. In many cases it is not acceptable to use two sets of equations. These cases include flows with strong coupling between the outer inviscid region and the boundary layer, such as found in a supersonic flow around a blunt body or in flows containing strong shocks. In these instances it would not be valid to neglect the normal pressure gradient when forming the normal momentum equation. As a consequence boundary layer techniques are often inadequate.

Another set of equations which are approximations to the Navier-Stokes equations and which are valid for both the inviscid and viscous regions, are receiving considerable recent attention. These are known as the thin-layer Navier-Stokes equations. They simplify the complete Navier-Stokes equations by neglecting the viscous terms containing derivatives parallel to a solid surface, as in the boundary layer formulation, but retain all the other terms in the momentum equation; thus, the pressure gradient in the direction normal to a surface is not neglected. The use of the thin-layer Navier-Stokes equations allows the robust calculation of separated and reverse flows and flows containing significant normal pressure gradients. In many instances the thin-layer equations can be treated by the same efficient boundary-layer type marching techniques that are employed in solving the boundary layer equations.

Sets of equations, each of somewhat different form and similar to the thin layer Navier-Stokes equations, are obtained if only the streamwise viscous terms are omitted from the Navier-Stokes equations. These forms are called the parabolized Navier-Stokes equations, and the

differences in the forms depend on their derivation and whether terms such as the streamwise pressure gradient are retained in the streamwise momentum equation. The thin layer and the parabolized equations are equivalent for two-dimensional flows. However, efforts to develop efficient solution procedures are hampered by the fact that different forms generally require different strategies due to the nature of the equations or characteristics of the flow.

Very useful inviscid forms of the governing equations exist. Currently, solutions of the Euler equations, obtained from the Navier-Stokes equations by neglecting all the viscous terms, are solved routinely for two-dimensional flows and even three-dimensional codes are emerging. Wider use has been made employing the full potential and small disturbance forms of the potential equation for inviscid, irrotational flows. While the Euler equations are valid for rotational flows, the potential formulations are not, and thus, the latter are not strictly valid when entropy producing discontinuities such as shocks exist. On the other hand, many instances occur where the departure from purely irrotational flow is slight, such as the flow around thin bodies or in the case of shocks which are sufficiently weak as to generate little entropy or vorticity.

In general, considering the flow around an aerodynamic surface to be inviscid allows the lift to be calculated quite accurately. The drag, on the other hand, depends substantially on frictional stresses as well as the distribution of the normal pressure over the surface. Frictionless flow theory can be used for the determination of the drag component arising from the normal pressure components whereas an

appropriate skin friction coefficient must be used to obtain an estimate of the total drag.

A number of numerical codes are currently being developed to calculate propeller flow. These solve either the full potential or Euler equations. Although these equations accurately model the flow, they are computationally more expensive and are more complicated to code than the small disturbance equation.

A computer program was developed (Refs. 1 to 4) to simulate the flow over blade-tips of helicopter rotors. This code solves the small disturbance equation (Ref. 5) appropriate to a helicopter in forward flight. In particular, results were obtained that showed the code was able to track the development of a shock and its subsequent propagation upstream. The successful application of the small disturbance code in this manner indicated that the same approach could be applied to the propeller problem.

The fact that turboprops operate at high subsonic cruise speeds means that at least the tip region of each blade will be embedded in a transonic helical flow. Shocks may likely exist ahead of, or on, the blades, depending on the flight speed and propeller design. Shocks of high strength indicate large wave drag. Efficient flight dictates that only weak shocks are acceptable, which implies little entropy generation. The potential formulation should provide a good approximation to the Euler equations as long as the shock strengths are less than that of a normal shock with an upstream Mach number less than about 1.3. Presently, turboprops that have helical Mach numbers slightly less than 1.0 at the hub to about 1.12 at the tip are being designed. It is reasonable to expect that the shock strength is

sufficiently weak near the blade tips, where three-dimensional relief effects occur. Hence, that the potential formulation is adequate. Furthermore, the use of a perturbation potential in place of a full potential significantly simplifies the formulation of the problem.

Although many similarities exist between the equations developed for the helicopter rotor and the propeller problem, fundamental differences exist between the two. These differences demand that special consideration be made in accurately treating each type of flow. For example, in the case of the helicopter rotor, the flow field as observed in a coordinate system attached to the blade remains unsteady even if blade flutter is ignored. However, when the axis of rotation for a propeller coincides with its flight direction, a steady flow results with a blade attached coordinate system. This allows the steady problem to be examined separately from the flutter or gust problem. With the goal of using the numerical algorithm developed for the rotor code to the propeller problem, several concerns need to be addressed. Many of these concerns are naturally handled by using a suitable coordinate system.

The key to simplifying the potential formulation of the propeller problem is the use of the helical free-stream direction as the primary direction. This provides an accurate primary flow upon which a perturbation can be superposed. The use of a helical flow, which inherently captures the flow curvature, results in a marked improvement over using an axial flow as the primary flow direction. The optimum flow to base a perturbation about is the exact flow; helical flow much more closely approximates the exact flow about a rotating and advancing propeller than does axial flow.

Since the helical flow direction captures the fundamental properties of propeller flow, relatively few terms are needed in the resulting disturbance equation to provide accurate modeling of the flow. In fact, no more terms are needed than when using Cartesian coordinates for the rotor problem. In addition, due to the similar nature of the two problems, the terms in the two sets of disturbance equations correspond identically except for their coefficients. Thus, the propeller equation is amenable to the same potential equation solver as developed for the helicopter. This is quite advantageous since much effort has been expended, both in making the potential solver efficient and in verifying its operation.

While the helical flow direction is an ideal choice for the primary flow direction, other considerations must be taken into account in order to provide a satisfactory coordinate system. These considerations hinge on the desire to include cascade effects and the employment of small disturbance boundary conditions near the blade surfaces. Proper specification of the helical coordinates permits the straightforward treatment of annular cascade flows while maintaining orthogonal properties near the blade locations. The helical coordinates given in this thesis allow both of these requirements to be met.

These helical coordinates are analytically defined in terms of basic propeller parameters through simple transformations to Cartesian coordinates. Thus, they automatically adapt to the cascade configuration for any number of blades and blade twist, which itself is a function of the propeller advance ratio. The helical coordinates enter the problem in terms of the components of the metric tensor for the transformation. These components are readily evaluated in a

separate subroutine. The Jacobian of the transformation is particularly simple and provides a means of verifying whether a given transformation is valid.

Obtaining accurate solutions for steady, not to mention unsteady, three-dimensional transonic flows, presents a difficult challenge even for the most advanced computational methods. The present work assumes a steady-state flow exists as observed in a reference frame attached to the propeller system, rotating with a constant angular velocity. This is considered a necessary step which must be completed before undertaking the unsteady problem. In addition, the fluid will be regarded as being inviscid in an irrotational flow field and thus is expressible in terms of a potential formulation. The solution is sought in terms of a disturbance potential. This disturbance potential is the potential associated with the reduced velocity obtained by subtracting both the free-stream velocity and the rotational velocity, resulting from the transformation to a noninertial reference frame, from the total velocity. This solution should be valid for lightly loaded blades.

Presentation of this thesis will begin with an introduction of some basic propeller concepts. In turn this will be followed by a historical review of some notable analytical and numerical endeavors related to propeller theory. This review is intended to provide the background and motivation for this work as well as form a basis for justification of the approach taken. In the subsequent chapter, the governing equation for the three-dimensional small perturbation potential is derived in detail from the general potential equation in a rotating reference frame. Here, the full potential equation is given in general tensor form applicable to any suitable coordinate system which need not be

orthogonal. Following this, the small disturbance form of the equation is derived in terms of coordinates which are scaled by the relevant transonic scaling parameters. A separate chapter is next provided for the boundary condition equations. A chapter dealing with the coordinate system construction and its arrangement to suit a cascade of propellers is then presented. This is related to two appendixes on analytical helical coordinate transformations. Next, a chapter on the numerical procedure and solution technique is given. A generalized form of the Douglas-Gunn algorithm is introduced which allows for additional cross-derivative terms to be included in the potential solver. However, for the flow cases presented here, these terms had little effect on the solution, and, hence, for the results of this effort they were omitted from the governing equation. The next chapter presents and discusses details of the results obtained. Solutions are presented for an annular cascade consisting of eight bicircular arc blades with a maximum thickness of five percent. These blades are run for two geometric operating conditions: a high advance ratio case where the advancing speed is large compared to the rotational speed of the propeller tip, and a low advance ratio case where these two speeds are equal. For the high advance ratio case, the helical free-stream Mach number relative to the blade tip is $M_R = 0.8$. For the low advance ratio case, results for two values of the free-stream Mach number are presented--a subsonic free-stream case of $M_R = 0.8$, and a transonic case of $M_R = 1.1$ which is representative of a turboprop. In general, the results are for zero angle of attack; however, a lifting case is presented for the low advance ratio and high free-stream condition. The nonlifting cases are compared with results from an Euler code (Ref. 6). A final chapter

delineates conclusions reached and recommends future efforts. Three appendixes are included. The first two concern helical coordinate systems; the first of these presents the metric tensor for periodical coordinates used in the present work and the second presents nonperiodical coordinates used for flow about isolated blades. The remaining appendix contains a listing of the formulas for the derivative expressions relating stretched coordinates and uniformly spaced computational coordinates.

II. PROPELLER CHARACTERISTICS AND NOMENCLATURE

Some basic concepts will now be introduced related to common propeller characteristics and nomenclature. In many ways it is useful to think of the propeller as a highly twisted wing acted on by both lifting forces and drag forces. Lift is produced normal to the relative velocity at the surface. For small angles of incidence α_i, the lift is proportional to this angle. The angle of incidence equals the angle of attack α, minus the angle of zero lift α_o, as shown in Fig. 2.1. In a real fluid, drag is produced in a direction parallel to the relative velocity between the fluid and the body. The main distinction between a wing and propeller is that a propeller rotates and produces thrust while working its way through the fluid whereas a wing just advances while producing lift. The combined rotational and forward motion of the propeller results in highly twisted blades which are formed of radially varying profiles with the thickest sections nearest the hub. This increase in complexity admits additional parameters beyond those encountered in wing theory.

The most important propeller parameter is the advance ratio which relates the forward velocity V to the rotational speed. The forward velocity is assumed to lie in the direction of the axis of rotation and will often be referred to as the axial velocity. The advance ratio J is commonly defined as equaling the propeller's forward velocity divided by the product of its rate of revolution n times its diameter D:

$$J = \frac{V}{nD} \quad . \tag{2.1}$$

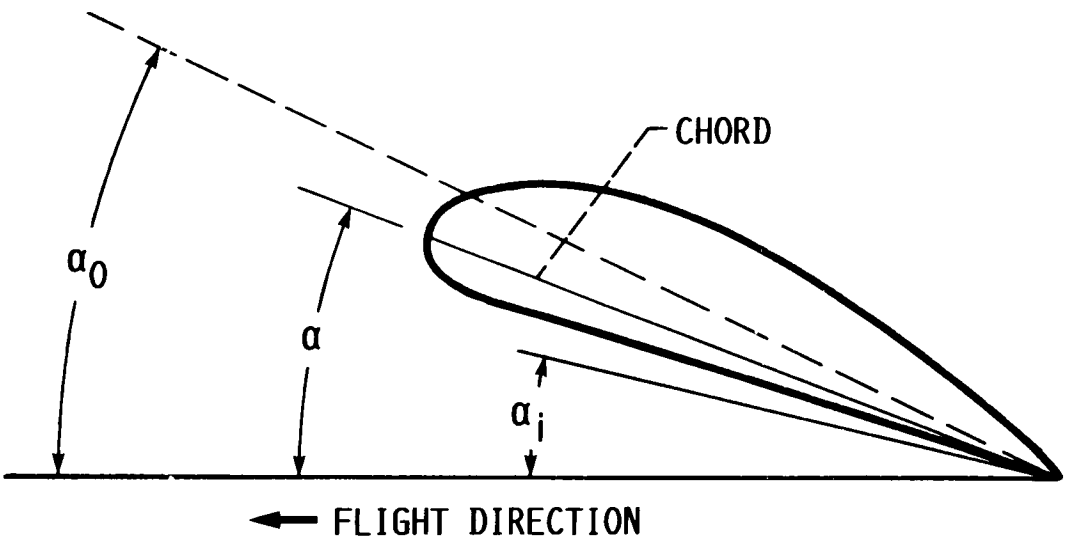

FIGURE 2.1. - AIRFOIL SECTION SHOWING ANGLE OF ATTACK α, ANGLE OF INCIDENCE α_i, AND ANGLE OF ZERO LIFT α_0.

Another definition of the advance ratio is frequently used. It is designated by λ and equals the ratio formed by dividing V by the angular velocity of the propeller's tip

$$\lambda = \frac{V}{\Omega R} \tag{2.2}$$

where Ω is the angular frequency of shaft rotation and R is the tip radius of the propeller. Convenience or mode of practice determines which definition is used since the two are related by

$$J = \pi\lambda. \tag{2.3}$$

In the present work, λ will be used throughout.

The relationship between the forward and rotational velocities for any propeller section is expressed in terms of the advance angle β diagrammed and related to a helical curve in Fig. 2.2. The following relation connects the advance angle with the radius:

$$\tan \beta = \frac{V}{\Omega r} . \tag{2.4}$$

The slope of any helix is thus proportional to $1/r$. The distance advanced during one revolution is termed the pitch, obviously the same for all radial elements of a rigid body. The surface swept out by the leading edge of a rotating and advancing propeller is a helical surface or helicoid and is called the advance helicoid. The angle of attack of any blade element is generally referenced to the advance angle β; i.e., the angle of attack is measured from the advance helicoid. This is because a very thin blade constructed to lie in the advance helicoid produces no lift, and thus it gives a definition consistent with that of the planar wing. Blades are constructed such that the angle of attack varies radially. This variation in α can be interpreted as a radial variation in blade pitch since each radial element of the blade has a

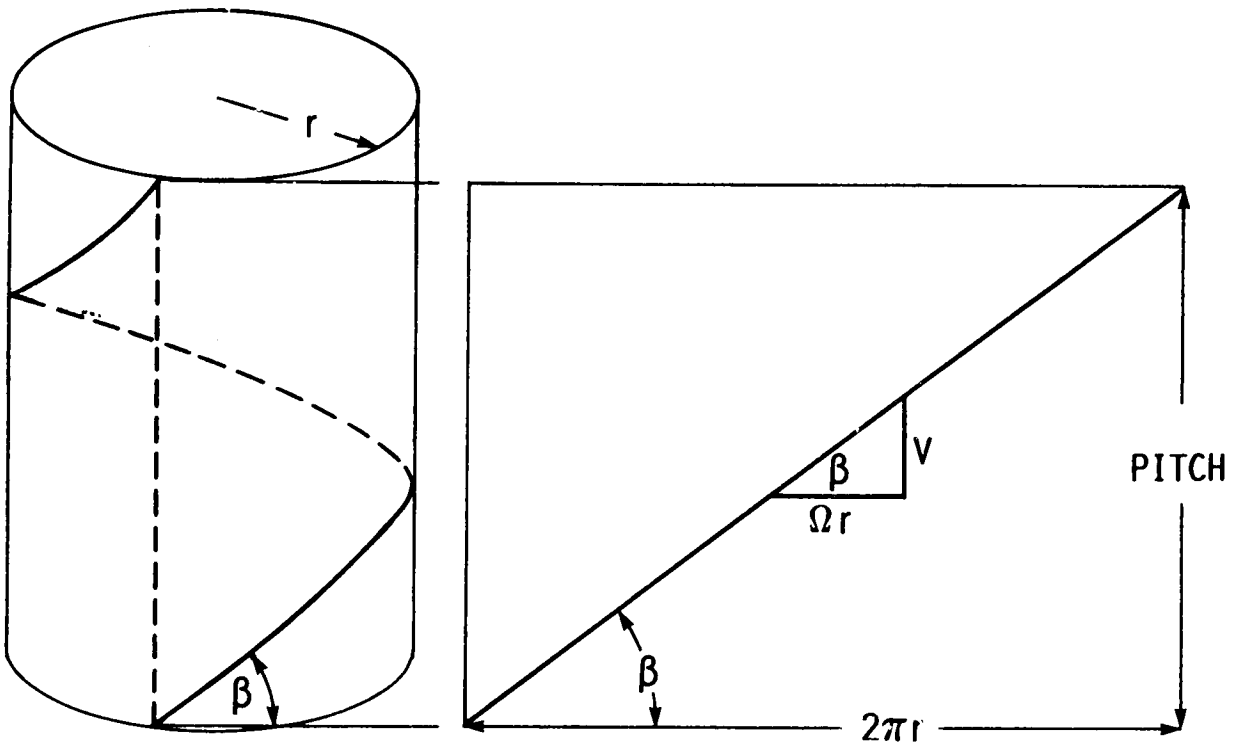

FIGURE 2.2. - HELICAL CURVE WITH ADVANCE ANGLE β.

geometrical pitch which, in general, differs from the pitch of the advance helicoid; the mean surface of a lifting, symmetric blade does not lie in a helical surface. This spanwise variation of blade pitch introduces lift and allows the blade to be optimized in regard to its ratio of lift to drag. In elementary design the pitch of each section is chosen to give the optimum angle of attack for that section's profile. Figure 2.3 illustrates a typical span station showing the chord ℓ, angle of attack α, and the maximum thickness t_{max} along the chord.

The performance of a propeller is measured in terms of its efficiency. The efficiency η is defined by

$$\eta = \frac{\text{THRUST x FREESTREAM VELOCITY}}{\text{SHAFT POWER}} \tag{2.5}$$

It is convenient to introduce dimensionless coefficients for thrust and power that have the form

$$C_T = \frac{T}{\rho n^2 D^4} \quad \text{and} \quad C_P = \frac{P}{\rho n^3 D^5} , \tag{2.6}$$

respectively, where T is the thrust, P is the shaft power, and ρ is fluid density. Then the efficiency can be simply expressed in terms of these coefficients and the advance ratio J in the following form:

$$\eta = \frac{C_T J}{C_P} \tag{2.7}$$

When stating the efficiency for a complete propeller system, it is necessary to denote the thrust, thrust coefficient and the corresponding efficiency in a manner indicating that the effects of components such as the spinner and nacelle are included. This is customarily done by using the subscript "net," such as in the following:

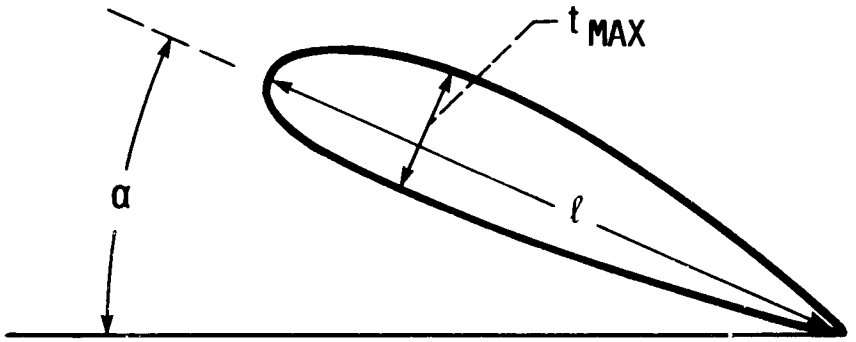

FIGURE 2.3. - AIRFOIL SECTION SHOWING CHORD ℓ, ANGLE OF ATTACK α, AND MAXIMUM BLADE THICKNESS t_{MAX}.

$$\eta_{net} = \frac{C_{T,net}J}{C_{P,net}} \quad . \tag{2.8}$$

III. HISTORICAL REVIEW

3.1 Analytical Methods

Investigations of flow about propellers have their roots in the early work of Rankine and Froude which was based on simple momentum theory for an incompressible flow. Simple application of momentum theory considers the momentum and energy of the fluid and treats the propeller as an actuator disk that imparts momentum to the fluid which passes through. This causes the formation of a slipstream of increased axial velocity. In performing this analysis (Refs. 7 to 8), it is useful to assume that the propeller system is composed of a large number of equally spaced blades producing a circumferentially uniform flow in which the velocity is constant across the disk but greater than that of the surrounding free-stream. A pressure change occurs across the disk which accounts for the momentum gain. By assuming irrotational flow and by applying Bernoulli's equation to streamlines on each side of the disk, this change in pressure can be related to the velocity rise in the final slipstream. The values of the pressure and velocity at pertinent locations are shown in Fig. 3.1 which illustrates this simple model. The value of the velocity increase, v, at the disk is found to be exactly half the increase, v_1, existing in the final slipstream.

Further results concerning propeller efficiency may be presented after considering the increase in axial momentum and rate of energy input. The use of momentum theory leads to limits on the maximum efficiency. Explicit relations are obtained between efficiency and both

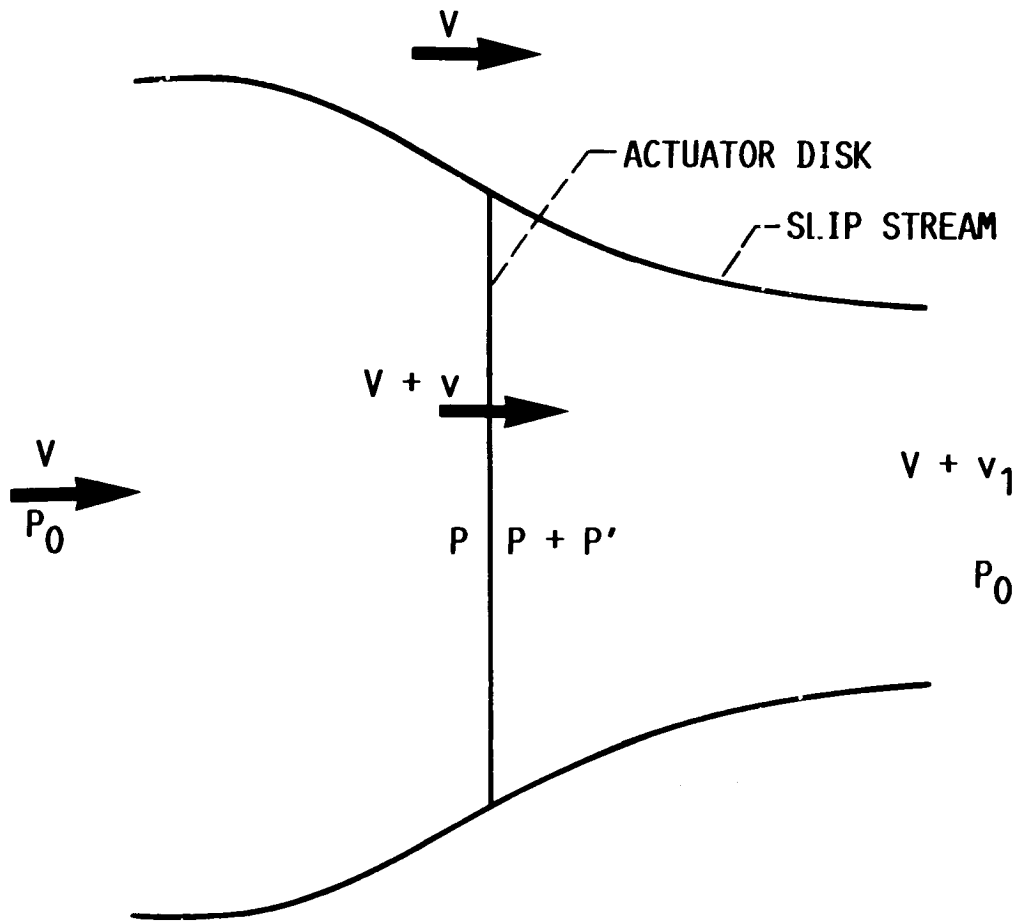

FIGURE 3.1. - ACTUATOR DISK WITH UNIFORM CIRCUMFERENTIAL FLOW.

power and thrust, which are customarily represented in terms of their coefficients, as a function of the most important propeller parameter, the advance ratio J. A more exact account of momentum theory, including the effect of slipstream rotation is given by Betz (Ref. 9). However, it should be mentioned that momentum theory fails to yield the detailed forces (loading) acting on each blade element.

The attempt to determine the forces acting on the blades leads to the creation of the blade element theory. This theory approximates the aerodynamic forces acting on a blade by treating each radial element between r and r + dr as a two-dimensional wing section. The use of wing section theory provides the elemental lift and drag forces, which can be resolved in component form in the directions of thrust and torque, at each radial section. The values of the total thrust and torque can be determined by integrating the contributions of the radial elements. Corrections to account for the influence of neighboring elements can be added in an empirical manner.

The application of blade element theory has been used in conjunction with momentum theory to provide improved results over solitary use of either method. This combined technique provides perhaps the best method for evaluating propellers with a large number of blades without actually calculating the entire three-dimensional velocity and pressure fields comprising the flow. However, for the normal situation involving propellers with few blades, the assumption of axial symmetric flow arising from the momentum viewpoint is weak since most of the flow does not pass near a blade.

The evolution of propeller theory advanced significantly from the work of Goldstein (Ref. 10) which also stemmed from the successful

development of the theory of the airfoil. This theory acknowledged the role of circulation in the generation of lift, a concept set forth by Kutta and Joukowski, and it also contained the formulation of Prandtl's model of flow past a finite wing of large aspect ratio. Prandtl's model introduced the concept of a continuously trailing vortex sheet which replaced the simpler model of two trailing tip vortex lines offered by Lanchester. Furthermore, this model allowed the actual airfoil to be replaced at its mean location by a bound vortex sheet across which a pressure difference can exist. For wings of large enough aspect ratio, the vortex sheet representing the wing can be approximated by a single bound vortex line lying in the plane of the wing normal to the approaching flow and with spanwise varying strength. Together the streamwise aligned vortices of the trailing vortex sheet and the lifting line vortex, representing the wing, induce velocities which superpose with the undisturbed stream velocity. The application of these propositions to the case of the propeller, including the modifications needed for three dimensional flows containing discontinuities, results in a complicated set of integral equations.

Using the groundwork provided by early airfoil theory, Goldstein constructed a model which assumed that the trailing vortices emanating from the rear edge of the propeller forms a rigid vortex sheet of constant velocity, which closely approximates the structure of a helical sheet. The rigid vortex sheet was assumed to be embedded in an inviscid fluid with zero circulation. The flow far downstream of the propeller was taken as satisfying Laplace's equation: $\nabla^2\Phi = 0$, where Φ represents the velocity potential whose gradient is the fluid velocity. By aptly defining a helical coordinate along the screw surface in terms

of cylindrical polar coordinates, Goldstein was able to simplify the treatment of the boundary conditions. Satisfying single-valuedness and meeting continuity requirements, etc., led to a solution for the velocity potential far downstream of the propeller in terms of Bessel functions. Formulas were then derived from which the optimum load distribution along the blades could be calculated for any number of blades.

Proceeding along the lines set by Goldstein, Reissner (Ref. 11 to 12) derived and presented in more detail (Ref. 13) integral relations connecting circulation, thrust and torque along the span with the geometric and flow parameters such as blade angle distribution, number of blades and inflow angle. It is interesting to note that while the complete set of equations presented was derived on the foundations developed from wing theory for incompressible flow, nevertheless, ideas introduced by H. Lamb (Ref. 14), for treating the magnetic field arising from a helical electric streamline, were drawn upon. Lamb presented the three-dimensional Biot-Savart integral in a manner which took advantage of helical symmetry and managed to reach solutions for the electric potential problem which were comprised of Bessel functions of the first kind for the inner radial field and of the second kind for the outer field. Reissner set out from this point, aided by the work of Kawada (Ref. 15), which was concerned with the induced velocities resulting from a circulation of constant strength along a blade and which also made use of helical symmetry. Reissner based his mathematical development on the Poisson differential equation, $\nabla^2\Phi = q$, for a velocity potential produced by an arbitrary source distribution. He proceeded toward a more general integral equation, which differed from

the Biot-Savart integral and the series solution obtained by Goldstein, by replacing the blades with lifting lines with infinitely thin trailing vortex sheets. The vortex sheets were represented by the proper distribution of sources and sinks entering on the right-hand side of Poisson's equation. Helical symmetry was invoked to reduce the number of independent coordinates to two, with the new independent coordinates being a radial coordinate and a helical coordinate defined in the manner of Goldstein and Kawada from cylindrical coordinates. The ability to arrive at this two-dimensional equation for the velocity potential relied on the vortex sheets being arranged so as to lie on multiple sheets of helical symmetry with infinite extent downstream. Further refinements, which removed this symmetry condition but improved the theory, were pointed out by Reissner. These included taking into account the radial contraction of the flow on passing through the propeller system (slip-stream contraction) and the displacement of the helical vortex sheets due to their mutual interaction. These improvements were considered, however, to be of a secondary nature.

Shortly before the end of World War II, Theodorsen published a series of technical papers (Refs. 16 to 19) dealing with both single and dual rotation (counter-rotating) propellers. These reports formed the basis of his subsequent book Theory of Propellers (Ref. 20), which presented experimental measurements as well as the theoretical treatment.

Theodorsen extended the lightly-loaded theory presented by Goldstein in his 1929 paper to that of heavy loading by redefining certain key propeller parameters. Goldstein had acknowledged that a better approximation would be gained, valid for moderate loads, by doing

such. This modification took into account the increase in advance ratio and slipstream contraction that can occur to a wake surface as it travels downstream; see Fig. 3.2. Expressions were derived for the thrust, torque, and efficiency in terms of these parameters. Included with these parameters were the circulation coefficient connecting the circulation at each blade element to the advance ratio and the mass coefficient parameter which represented an average of the circulation coefficient over the cross-section normal to the flow. It is important to note that these parameters referred to the ultimate wake and not to the region immediately behind the blades. Theodorsen reasoned that the distribution of circulation existing on the propeller blades is, to the first order, the same as the resulting distribution of potential difference existing in the wake if the radius of the wake is stretched at each axial location to equal the radius of the propeller blades. The optimum circulation distribution for heavy loading is thus identical to that of light loading provided the helix angles in the ultimate wake are the same. Thus, the key relations for propeller theory, as developed along the lines of Goldstein, were extended to heavy loading and expressed compactly in terms of the important mass coefficient parameter.

In addition to the theoretical development, Theodorsen carried out extensive detailed measurements. Here he relied on the analogy between electrical theory and fluid mechanics for potential flow to conduct electrolytic-tank measurements in place of conventional wind-tunnel tests. By placing a helical insulating surface into an electrolytic tank with a uniformly imposed electric field along it axis, an electric field entirely descriptive of the discontinuous flow behind a propeller

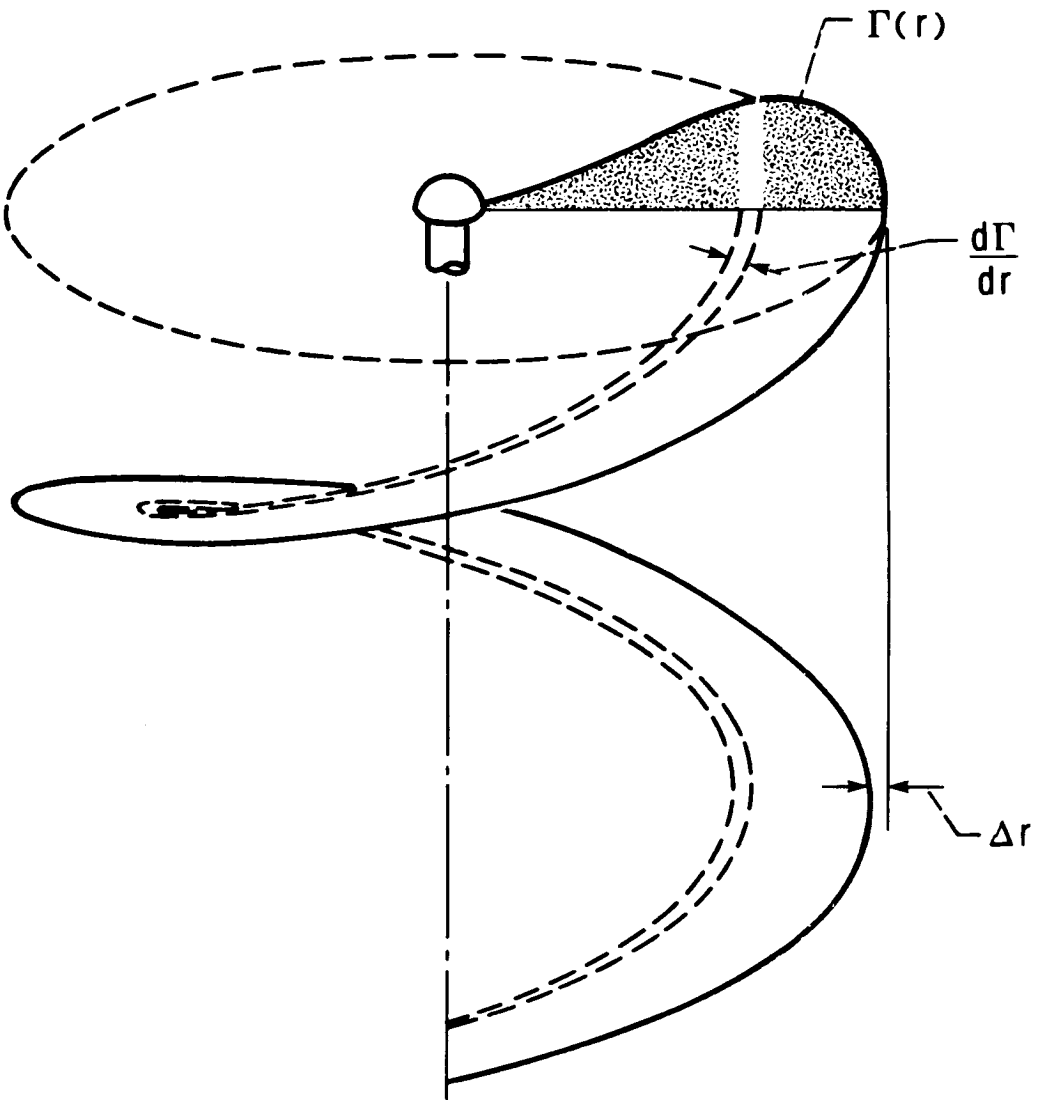

FIGURE 3.2. - WAKE PROPAGATING DOWNSTREAM CONTRACTS CORRESPONDING TO AN INCREASE IN PITCH.

was produced. The effect of advance ratio and number of blades on the mass coefficient was readily determined by varying the helix shape and geometry of the tank. This provided the experimental results needed for comparison with theoretical results and extended the results beyond the known range to include higher advance ratios. The general procedure is covered in some detail for applying the theory to the general design problem. The interested reader is referred to Theodorsen's book.

Still within the structure of linearized theory, Busemann (Ref. 21), and Davidson (Ref. 22) attempted to include compressibility effects by generalizing the incompressible propeller theory to supersonic tip speeds. These two investigations progressed from origins similar to those of Goldstein and Reissner. Busemann advanced physical arguments to explain or predict changes in the flow for higher Mach numbers; Davidson provided detailed calculations as well. The most notable characteristic of flows at Mach numbers approaching unity is the mixed nature of the flow fields. For mixed flows the elliptic character of the solutions for subsonic regions, which are essentially incompressible, are joined by the hyperbolic character representative of the supersonic regions where compressibility effects cannot be ignored. The existence of supersonic as well as subsonic regions of the flow was recognized and tied to the solutions which again took the form of Fourier-Bessel functions. In these cases the solutions obtained satisfied the steady linearized small disturbance equations. Busemann's equations were restricted to two dimensions involving polar coordinates. Davidson developed a more general disturbance equation which was expressed in both cylindrical and helical coordinates. Although the equations contained no nonlinear terms, they exhibited the mixed nature

of the flow field which progressed with increasing radius from an entirely subsonic (subcritical) flow to a flow embedded with pockets of supersonic (supercritical) flow to, finally, totally supersonic regions at the tip. In contrast, the fixed wing problem results in essentially only one of the above cases depending on the approaching Mach number. It is largely a result of the radial variation of the helical velocity that makes the propeller problem more complex than that of the wing. This is evidenced by the presence of the spanwise-type mixed flow feature even with linear theory.

Even within the limitations of linearization, the effects of numerous geometric parameters must be taken into account for a more rigorous treatment of propeller flow. The effects of thickness, camber, angle of attack, sweep, offset, blade interference, and tip relief must be dealt with to a sufficient degree. A number of more recent investigations has addressed different aspects of these problems. In particular, an analytical effort by Hanson (Ref. 23) to include these items resulted in a fairly general description of the flow field. He constructed an analysis for prop-fans based on the acoustic methods of Goldstein (Ref. 24) which relate the density disturbance at any point in a medium enclosed by impermeable walls to the arbitrary motion of unsteady sources. This is accomplished via an integral formulation employing Green's functions and provides an integral equation for the near and far field density disturbance and one for the unsteady velocity potential. The result for the disturbance pressure, or acceleration potential as it is often called, is valid for any Mach number and planform but presumes that the surface pressures are known. The formulation for the derivation of the velocity potential contains only

linear source terms and is valid for any steady or unsteady helically convected source. The velocity potential itself must be obtained by inversion methods used for wing analysis. Two key elements were needed to achieve these results. First, the exact boundary conditions at the blade surfaces were actually applied at mean reference surfaces approximating the blade positions, thus greatly simplifying the mathematics. Secondly, it was recognized that a helicoidal surface theory could be used as a natural extension of wing theory with the observation that each blade element rotating in forward flight sweeps out a helix. Thus, a coordinate system was established that was formed by a dimensional coordinate at constant radius in the advance helicoid, a radial coordinate, and another coordinate at constant radius lying in the helicoid normal to the advance helicoid. Blade coordinates are then transferred to the advancing helicoid at locations neighboring the upper and lower blade surfaces as in thin airfoil theory. In this manner the ideas of wing theory were adapted to propeller analysis. This analysis then gives aerodynamic and acoustic information pertaining to steady performance, unstalled flutter, and noise radiation.

This discussion concludes the section on analysis methods; it is necessarily incomplete, but presents a review introducing many of the important concepts developed earlier in propeller theory. It should be stressed that the above methods neglected many physical phenomena in order to simplify the mathematical models and provide solutions. Indeed, their success hinged mainly on construction of simplified models. These models retain most of the significant physics, and which could be solved and lead to improved designs. It is testimony to the insight and resourcefulness of these early researchers that such large strides could be made.

3.2 Nonlinear Flows with Shocks

This section discusses the development of CFD methods applied to high-speed flows where compressibility effects are important and in which shocks may be present. Generally the effects of viscosity and heat conduction will be considered negligible, though some comments will be made concerning the former. The development of successful CFD methods has relied on an understanding of the physical characteristics and the mathematical properties of the partial differential equations associated with these flows. The physical significance and the mathematical behavior of the governing equations for inviscid flows of this type will be reviewed in order to establish the consequences of transitioning from partial differential equations to finite difference equations.

Difference equations can be thought of as approximating the partial differential equations (PDE) on a general lattice of mesh points. In this manner, the continuous functions present in the PDE will be replaced with finite difference functions that are discrete and defined only on the lattice and only at discrete intervals of time. The finite difference equations will be considered consistent with the corresponding PDE if it can be demonstrated that any difference between the PDE and the finite difference representation vanishes as the general lattice of mesh points is refined. This can be accomplished if a substitution of an assumed solution to the PDE in the form of a Taylor series expansion into the finite difference equation produces agreement to within a set of higher order terms which tend to zero as the mesh spacing and time interval simultaneously are allowed to approach zero. The higher order terms are called the truncation error terms and represent one measure of solution accuracy. The accuracy cannot be

predicted beforehand since in each truncation error term, a derivative factor of differential order corresponding to the order of the term is also present, but unknown. For cases where large gradients in the solution exist, these derivatives can be large enough to offset the smallness of the mesh. Estimates of accuracy can be made once a solution is achieved by examining the truncation terms or by repeating the calculation for several levels of mesh density. The consistency condition is an important requirement for a difference scheme. If a difference scheme converges, then it will converge to the solution of the corresponding differential problem provided that they are consistent with each other.

In addition to consistency, one would prefer that the solutions for a set of finite difference equations possess certain properties desired similarly, though not necessarily guaranteed, for the PDE. One hopes that a solution exists that is unique and stable. In this regard a problem can be considered to be stated properly if it has exactly one stable solution satisfying both the governing equations and the auxiliary conditions. The auxiliary conditions are usually boundary or initial conditions but may include both or other types of constraints. The existence and uniqueness requirements are dependent on the stated conditions being consistent and sufficient to determine a unique solution. The stability property manifests itself in different contexts. A stable solution of a mathematical physics problem implies that, for small changes in a given condition, there will be correspondingly small changes in the solution. The question of stability is very important since inevitably the process of carrying out a solution introduces some error through truncation or the inexact

specification of some condition. It is essential that the effect of these errors remain small, causing only small inaccuracies in the solution.

The solution of a problem using a finite difference grid carries with it inherent inaccuracies. Since information is utilized only at discrete points, small wavelength components are not resolved sufficiently, and those shorter than the length of a grid interval not at all. The question of stability in regard to finite difference equations can be addressed in terms of the growth in amplitude of frequency harmonics of the solution, and it is subsequently related to the ratio of the coarseness of the physical grid and the time step increment, in say an initial value problem. The iterative updating of the solution from a given time level to a new level Δt later is called the elemental marching step. Depending on whether the numerical scheme is of the implicit or explicit type or a mixture of these two types, certain frequency harmonics can experience unlimited growth in amplitude as the elemental marching steps are performed. The numerical scheme is said to be unstable if any frequency dominates the solution in such a physically unwarranted fashion. Restricting the time step to conform to the Courant-Friedrichs-Lewy (CFL) (Ref. 25) condition generally assures that such components will not grow exponentially, as long as additional destabilizing influences do not exist beyond those associated with the elemental marching step. Certain methods of enforcing the boundary conditions may lead to instability regardless of satisfaction of the CFL condition. Exact conditions for stability are not attainable for most time dependent and nonlinear problems. Recourse is often made to linear stability criteria obtained by neglecting nonlinear effects. This is

helpful in determining guidelines on stability bounds in many instances. The existence of stability and satisfaction of the consistency condition are sufficient to insure that the finite difference solution converges to the solution of a linear differential equation as the difference intervals tend to zero (Lax's Equivalence Theorem). Unfortunately, a similar statement cannot be made for nonlinear problems. The properties of existence, uniqueness, and stability are very important, but the problem of determining whether a problem is stated correctly is also very difficult. Some of these questions will be addressed further.

The nonlinearity of the inviscid transonic flow equations is the main hindrance in the development of analytical methods capable of solving these partial differential equations. Few instances arise where this difficulty can be avoided. Use of the hodograph plane transforms the basic equations into a linear form by transposing the roles of the independent variables. However, the hodograph transformation is restricted to two-dimensional flows, and even then, a trade-off exists in that the boundary conditions are generally more complicated though the equations are linearized. Thus, in most cases, the transonic flow equations will be encountered in a nonlinear form. In addition, shock-free inviscid flow solutions are rare, and if they exist are likely to appear as isolated solutions which are close to solutions containing shocks. This section will discuss some of these aspects and how they enter into consideration when devising finite difference methods applicable to transonic flows. With respect to numerical efforts, only a few cases will be considered which have a bearing on the present work.

Much of the progress achieved in the development of numerical methods for steady flows has been found to extend directly to unsteady applications. In this regard, steady flows are often solved as converged solutions of unsteady problems, asymptotically reaching steady state through real or pseudo time. Mention will be made of both unsteady as well as steady inviscid flows. Since this work solves a hyperbolic type equation due to the introduction of time as another independent variable, the unsteady perspective will be stressed. The efficient and accurate solution of a given flow, whether steady or unsteady, requires proper numerical simulation of the dominant physical phenomena. Hence, with the understanding that the proper numerical approach is more fully appreciated if the physical aspects of the problem are first understood, additional features pertaining to transonic flows should be stated beyond merely recognizing their nonlinearity. Transonic flows are characterized by the following traits: sensitivity to small perturbations; weak decay of these fluctuations as they propagate laterally; slow global adjustment to local disturbances; mixed nature with supersonic regions embedded within subsonic regions; and likely presence of surfaces of discontinuity such as shocks. Simple and accurate treatment of shocks is of primary importance in providing efficient numerical schemes for transonic flow. Therefore, a brief description of their nature will be given along with a quick review of how they are incorporated into the numerical modeling.

A simplified picture of shock waves can be provided if viscous and heat conduction effects are neglected while considering the response of a flow to a disturbance. The placement of a thin body in a uniform stream which approaches it at high subsonic or supersonic speeds

produces a discontinuity in the pressure field. This discontinuity results because high pressure pulses propagate more rapidly than low pressure ones and shock waves invariably form by coalescing pressure waves originating from any finite disturbance. The pressure waves must be compression waves in order for a shock to form, never expansion waves. In actuality these discontinuities are smeared out by physical dissipative effects which are absent when viscous and heat conduction effects are discounted; only in the limit of zero viscosity do shocks appear as discontinuities. However, the mathematical description of a shock is considerably simplified by neglecting these dissipative mechanisms and the approximation to reality is quite good in most cases.

It can be shown for unsteady plane flow that any disturbance that compresses the medium will eventually lead to a breakdown in the gas, i.e., a discontinuity will develop when a simple plane wave produced by a compression force propagates into a gas at rest. An example consisting of a limiting form of Burger's equation will illustrate the formation of a discontinuity from an initially smooth wave. It will also serve the purpose of introducing some concepts related to nonlinear partial differential equations that are basic to their understanding. In fact, many of the fundamental investigations concerning numerical computations deal with this particular equation, and thus it serves as a natural springboard to pass to more complicated equations by providing valuable core material underlying this area.

Burger's equation is a widely studied nonlinear equation modeling both convective and diffusive processes and is of the form

$$\frac{\partial u}{\partial t} + u \frac{\partial u}{\partial x} = \upsilon \frac{\partial^2 u}{\partial x^2} \tag{3.1}$$

where u, x, t, and υ can be taken as the nondimensional velocity, distance, time, and diffusion coefficient, respectively. Actually Eq. (3.1) is more accurately classified as a quasi-linear equation since it is linear with respect to the highest order derivative terms. We wish to examine the special case of $\upsilon = 0$; no diffusion occurs and Eq. (3.1) reduces to the homogeneous form

$$\frac{\partial u}{\partial t} + u \frac{\partial u}{\partial x} = 0. \tag{3.2}$$

Specifying an initial condition

$$u(x,t)\Big|_{t=0} = u(x,0) = \sin(x) \tag{3.3}$$

defines an initial value problem with a smooth initial curve. The solution to this problem is given in implicit form by

$$u - \sin(x - ut) = 0 \tag{3.4}$$

which is readily verified by its substitution into Eqs. (3.2) and (3.3). This solution is unique but exists only within a limited range of the initial curve. The solution is sketched in Fig. 3.3 for several time intervals. The waveform of the solution can be seen to progressively distort from the smooth shape at time $t = 0$ to a discontinuous shape at time $t = 2$ in the manner described above. This demonstrates an important property of the solution to nonlinear equations: they can develop discontinuities even with smooth initial data; this is in contrast to the linear case where discontinuities can arise only if the initial data are discontinuous. This indicates the necessity for admitting possible discontinuous solutions when solving nonlinear problems. More will be said later concerning discontinuous solutions to the equations of gas dynamics.

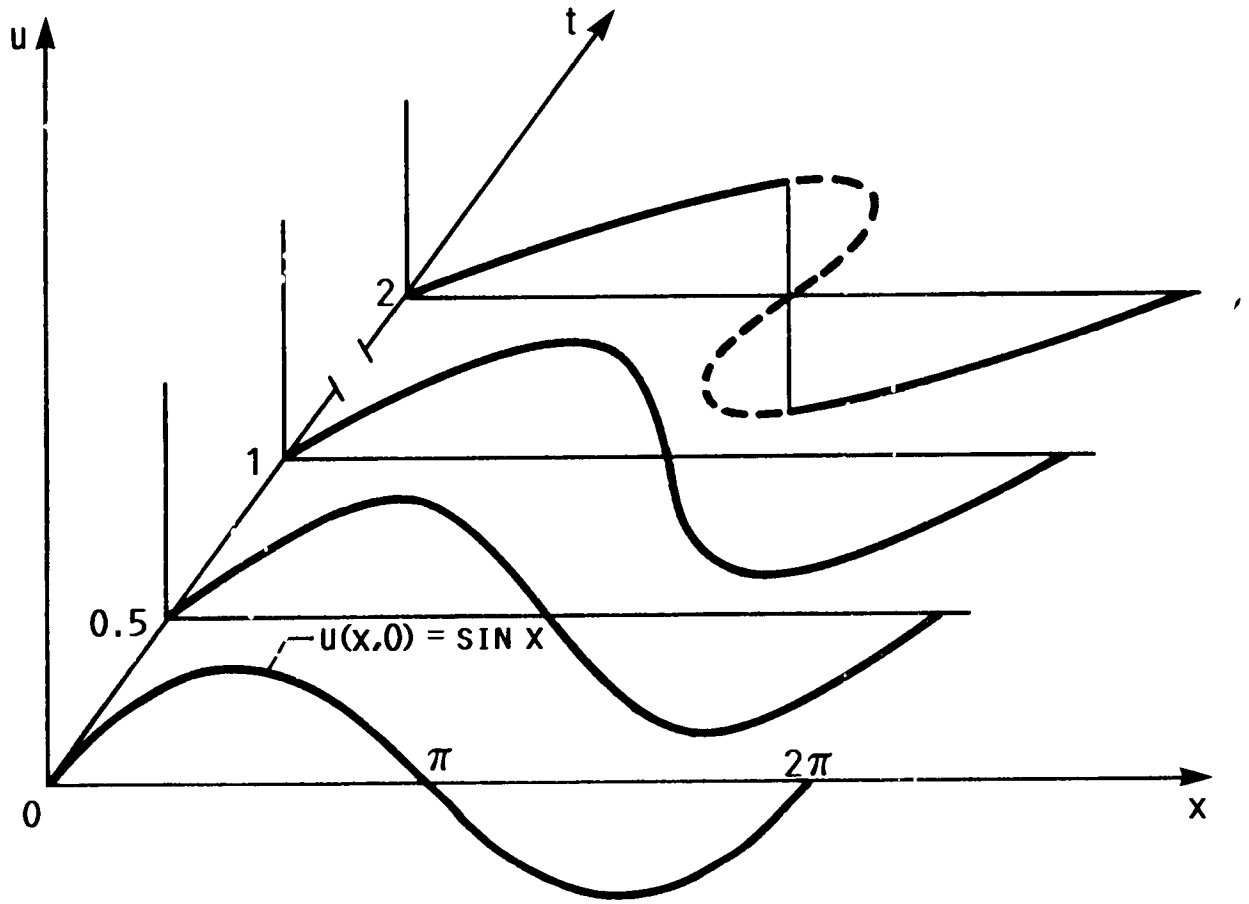

FIGURE 3.3. - DEVELOPMENT OF A DISCONTINUITY FROM AN INITIALLY SMOOTH WAVE.

We return to the examination of Burger's equation by connecting it to the theory of partial differential equations. This will provide access to some valuable geometric and analytic insight. To carry this out, observe that equation (3.2) is a quasi-linear differential equation in two independent variables, x and y, of a general form

$$P \frac{\partial u}{\partial x} + Q \frac{\partial u}{\partial y} = R \tag{3.5}$$

where P, Q, and R may be functions of x, y, and u only; furthermore, all variables and their first derivatives are continuous and $P^2 + Q^2 \neq 0$. In the special case presented above, $P = u$, $Q = 1$, and $R = 0$, and where in Eq. (3.2), t has taken on the role of the variable y that appears in the more general Eq. (3.5).

A general theory exists for equations of this type which can be drawn on in order to provide analytical results (Refs. 26 to 27). The solution to Eq. (3.5) can be interpreted in terms of an integral surface defined through the function

$$F(x,y,u) = C \tag{3.6}$$

where C is a constant and u satisfies Eq. (3.5); such a surface can be visualized geometrically in an x,y,u-space. The most general solution to Eq. (3.5) is a function $G(u_1,u_2)$ where u_1 and u_2 each satisfy the equation and correspond to separate values of the constant C, say C_1 and C_2, appearing in Eq. (3.6). Thus u_1 and u_2 are two distinct integral surfaces. The function F can be introduced into Eq. (3.5) resulting in an equation in which u can be considered independent along with x and y. The partial derivatives of F with respect to both x and y separately are each equal to zero as can be seen immediately from Eq. (3.6). These can each be used to give

expressions for one of the partial derivatives appearing in Eq. (3.5) which then assumes the following symmetrical form

$$P \frac{\partial F}{\partial x} + Q \frac{\partial F}{\partial y} + R \frac{\partial F}{\partial u} = 0 \tag{3.7}$$

provided that

$$\frac{\partial F}{\partial u} \neq 0.$$

This can be thought of as an expansion of the scalar product formed from vectors having components P, Q, R and $\partial F/\partial x$, $\partial F/\partial y$, $\partial F/\partial u$ in some appropriate orthogonal Cartesian system. Geometrically this has significance in that it shows that the vector with components P, Q, R is perpendicular to the normal to the integral surface at any point. Thus, the vector lies in the plane tangent to the surface at any point and its direction specifies a fundamentally important direction on the surface called the characteristic direction. This direction is unique at any point but, in general, differs with location. Starting at any point in the surface and following the characteristic direction along the surface results in a curve being traced out called the characteristic curve; hence, a characteristic curve is everywhere tangent to the characteristic direction. The projection of the characteristic curves onto the x,y-plane defines the physical characteristics.

An equivalent way of expressing Eq. (3.5) can be given that promotes its visualization geometrically by introducing certain parameters. This will aid in the construction of solutions which pass through a given curve. Extension of these concepts to higher dimensions provides an approach to constructing solutions for higher order problems by the method of iteration. From the theory of quasi-linear

differential equations, the characteristic curves are defined in terms of the following set of first order ordinary differential equations

$$\frac{dx}{ds} = P(x,y,u)$$

$$\frac{dy}{ds} = Q(x,y,u) \tag{3.8}$$

$$\frac{du}{ds} = R(x,y,u)$$

where s is a continuous parameter varying monotonically along these curves. A two-parameter family of integral curves satisfies Eq. (3.8) since there are two independent differential equations in this set, i.e., the set of equations depends on s and two additional constants. It is convenient to introduce new variables such that one is s which varies along each characteristic and the second variable τ is introduced as a parameter which is constant along any characteristic curve but varies from curve to curve. Together, the curves form a one-parameter family of solutions sweeping out the solution surface defined in Eq. (3.6) for a given value of C. Since the solution of the ordinary differential system admits a two-parameter family of solutions, an arbitrary function must be introduced to define a particular one-parameter family subset which satisfies Eq. (3.5). This arbitrary function relates the two arbitrary constants that arise from the solution of Eq. (3.8).

Specification of this function gives rise to an initial value problem for which the requirement that the solution surface pass through a particular curve establishes an initial value problem and fixes one parameter. The original independent variables can be defined in terms of the new variables as

$$x = x(s,\tau)$$
$$y = y(s,\tau) \tag{3.9}$$
$$u = u(s,\tau)$$

such that x, y, and u satisfy the initial condition that

$$x_o = x(0,\tau)$$
$$y_o = y(0,\tau) \tag{3.10}$$
$$u_o = u(0,\tau).$$

Here the value of s along the initial curve $\mathscr{C}$ is arbitrarily chosen as zero. It should be mentioned that the data curve x_o, y_o, u_o needs only to be continuously differentiable.

Solutions to the above system exist in some neighborhood of the given initial curve if the above transformation has the property that the Jacobian

$$J = x_s y_\tau - y_s x_\tau \tag{3.11}$$

does not equal zero. This guarantees that the transformation is invertible such that s and τ can be expressed in terms of x and y. In this case the solution $u(s,\tau)$ of Eq. (3.9) can be expressed as $u(x,y)$ and is generated by the characteristic curves which must lie entirely in the surface. Should the Jacobian vanish along $\mathscr{C}$, then either $\mathscr{C}$ is a characteristic curve and an infinite set of solutions exist or it is a noncharacteristic curve and no continuously differential solution exists. This statement applies to any other curve displaced from the initial curve. In general, should any two solutions u_1 and u_2 pass through the same curve, then it must be a characteristic curve. The significance of these remarks will become clear when requirements are discussed concerning the proper treatment of shocks as discontinuities.

By returning to the example of Burger's equation, the parametric approach can be applied directly giving information on the solution domain. Assume that a solution surface exists satisfying the homogeneous Burger's Eq. (3.2) which is generated by a one-parameter family of curves passing through the initial curve defined by Eq. (3.3). The first two expressions in Eq. (3.8) define the family of characteristics and the last one defines the solution surface in terms of the parameter which is constant along each curve. This can be can seen by carrying out the integration of Eq. (3.8) by recalling that $P = u$, $Q = 1$, $y = t$ and, since it is homogeneous, $R = 0$. The solution which satisfies the equation and the condition that it initially be a sine curve is given parametrically as

$$\begin{aligned} x &= s \sin \tau + \tau \\ t &= s \\ u &= \sin \tau \end{aligned} \tag{3.12}$$

(Ref. 28). The Jacobian of the transformation is

$$x_s y_\tau - y_s x_\tau = -(1 + s \cos \tau). \tag{3.13}$$

It can be seen that for certain values of s and τ the Jacobian will be zero. The locations where it vanishes are of interest, and the projection of these locations on the physical plane is termed the envelope. Such an envelope denotes positions where projections of the characteristics cross which, in turn, implies that the solution is no longer single-valued. The location of the envelope for this example can be determined by introducing the variables x and t into Eq. (3.13) and then setting this equation for the Jacobian equal to zero. The resulting curve for the envelope is then given by the relationship:

$$x = \cos^{-1} \frac{-1}{t} \pm (t^2 - 1)^{1/2}. \tag{3.14}$$

The solution for the envelope is sketched in Fig. 3.4. Since the value of R is zero for this problem, the third expression in Eq. (3.8) shows that the solution is constant along a characteristic curve which is verified by the last relation in Eq. (3.12). In the region to the right of the curves AB and AC in Fig. 3.4, characteristic curves cross and Eq. (3.14) is multi-valued; this corresponds to the dotted portion of the curve at $t = 2$ shown in Fig. 3.3. The discontinuity arising in the solution is a result of the crossing of characteristic curves, each associated with a constant value of u. Since the value of u is different for characteristics intersecting at the discontinuity, there is a resulting jump in the value of u associated with these conflicting characteristics. This exhibits a general feature of nonlinear equations. A discontinuity, which may be present in a nonlinear flow, does not lie along a characteristic curve. This is in contrast to a linear problem where discontinuities are present only if the initial data are discontinuous, in which case they are propagated along the characteristics. More specifically, it can be stated that shocks do not lie on characteristic curves but rather separate the flow into distinct regions differing by jumps in certain physical quantities. The jump in the physical quantities must satisfy certain physical criteria. It is exactly these jump criteria which serve to sift out the physically correct solution from the other mathematical solutions.

Because of the presence of these discontinuities, it is necessary to relax the stipulation that a solution be continuously differentiable. This fact stems from consideration of integral conservation laws which equate the rate of change in a quantity in a region to its flux at the boundary of the region. We can expand the definition of u to that of

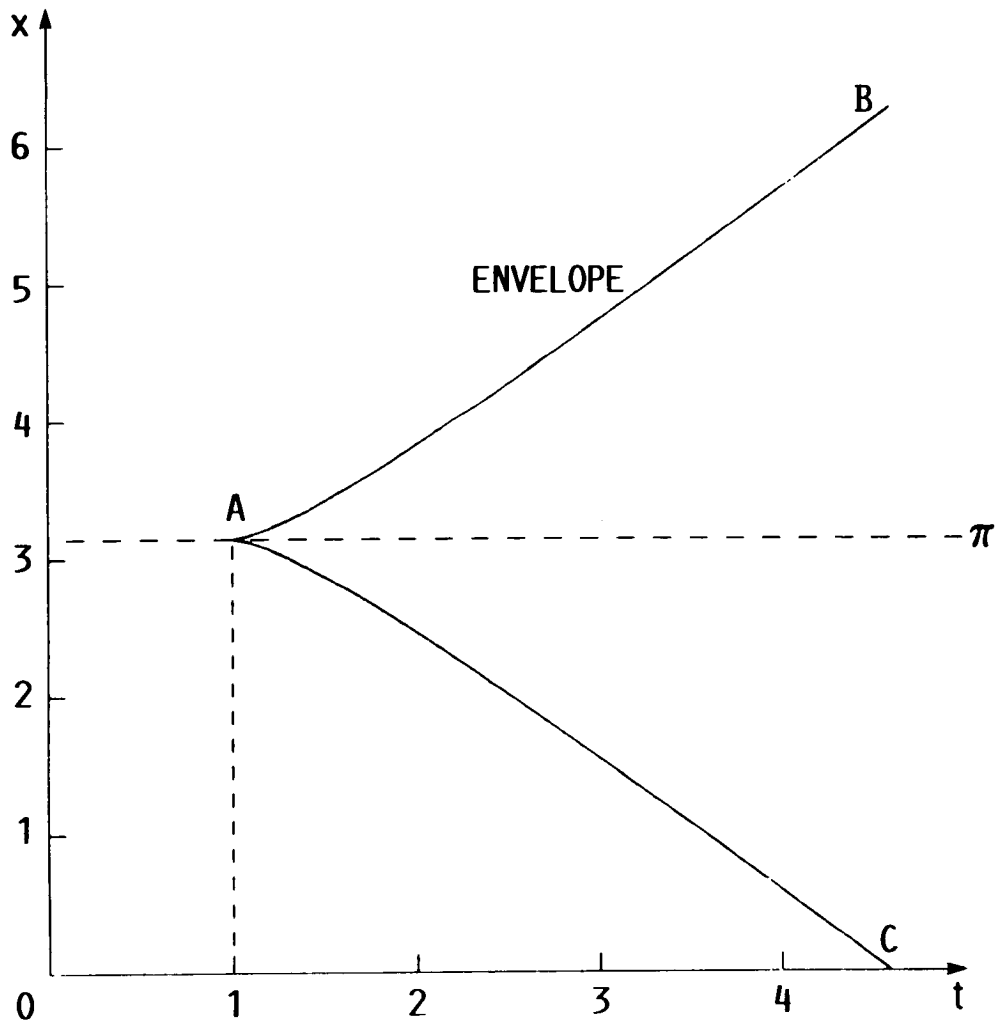

FIGURE 3.4. - ENVELOPE INDICATING WHERE VALUE OF JACOBIAN GIVEN IN EQUATION (3.13) IS ZERO.

a generalized density of a quantity and denote its flux as $\bar{f}$. The integral form of the conservation law for the quantity is

$$\frac{d}{dt} \int_{\mathcal{D}} u \, dx = - \int_S \bar{f} \cdot \hat{n} dS \tag{3.15}$$

for a general domain $\mathcal{D}$ of arbitrary dimension with bounding surface S possessing an outward normal $\hat{n}$ and where dx signifies the differential "volume" element. Here, we follow the presentation of Lax (Ref. 29) who omits the vector symbols in the scalar product. The conservation equation states that the rate of increase of the quantity in the region equals the negative of its outflow through the bounding surface. This holds for quantities like mass, momentum, and energy but not, in the general case, for entropy or internal energy for example.

Equation (3.15) is a general relationship to which the divergence theorem can be applied to the right-hand side, for sufficiently well behaved functions, which transforms it to

$$\int_{\mathcal{D}} (u_t + \text{div } \bar{f}) \, dx = 0 \tag{3.16}$$

with the time derivative moved inside the integral and denoted as a subscript. For u and f which possess continuous partial derivatives, the derivative form of the conservation law follows

$$u_t + \text{div } \bar{f} = 0. \tag{3.17}$$

This is the so-called divergence form of the differential conservation laws. The requirement that the derivatives be continuously differentiable implies that discontinuities such as shocks must be treated as internal boundaries separating the total domain into regions which by themselves possess smooth solutions; Eq. (3.17) then can be satisfied by these piecewise continuous solutions. Lax calls the

solution for the total region, including the discontinuity which satisfies the integral law, a generalized solution so as to distinguish it from a regular solution which must be differentiable.

Recall the example of the sine wave given above. The solution near the initial curve begins as a generalized solution, which is regular, but evolves into a generalized solution that is no longer continuous. The concept of a discontinuous solution is fully justified provided that it is physically meaningful. However, discontinuous solutions which satisfy the differential conservation laws may not be unique. The criterion that is used to distinguish the physically relevant solution is that the jump conditions existing across the discontinuity must satisfy the physics of the problem.

When shocks are treated as discontinuities, the differential equations must be replaced with equivalent upstream and downstream boundary (or "jump") conditions. These are known as the Rankine-Hugoniot relations. They can be obtained from the conservation laws, the Euler equations, by applying these laws separately to a control volume which contains the shock and which moves at the shock velocity. These relations specify the changes in the thermodynamic properties such as temperature, pressure, and density occurring across a shock without considering the detailed physics within the shock. In this way physically meaningful solutions are obtained. The Rankine-Hugoniot relations, which conserve mass, momentum, and total energy, were actually preceded by a set of analogous equations in which entropy was conserved rather than energy. Since entropy is not conserved across a shock, these analogous relations are normally discarded in favor of the Rankine-Hugoniot relations. Since shocks are the only means of entropy

production in inviscid flows, either set of conservation equations would be valid in a flow without shocks.

Some comments should be made concerning the potential equation derived from Euler equations by requiring the flow to be irrotational. By Crocco's theorem for steady flows, an irrotational flow is isentropic if the flow has constant total enthalpy; however, the flow may be rotational and still be isentropic. In this sense, isentropic flow is consistent with irrotational flow in that it imposes no additional restrictions on steady flows with uniform stagnation enthalpy. Thus potential calculations generally assume an isentropic jump, and consequently either conservation of mass, momentum, or energy must be sacrificed to prevent an overly determined system. The choice of conserving mass and energy is usually made, based mainly on the fact that they are both scalar quantities and that, for steady flows, integration of the energy equation implies constant enthalpy along streamlines. Klopher and Nixon (Ref. 30) review the three possible pairings for the conservation quantities and discuss the likelihood of conserving mass, momentum, and energy by allowing entropy changes to occur across the shock.

Conservation laws can also be expressed for a system of equations and take the differential form

$$\frac{\partial u^j}{\partial t} + \text{div } f_i^j = 0 \qquad j = 1,2,3,\ldots,n \tag{3.18}$$

for n unknown quantities and their respective fluxes f^j, where each flux is, in general, a nonlinear function of all the u^j. This can be written in an equivalent form where the divergence operator is replaced by differential operators appearing as an implied double summation over both repeated dummy indices i and k as such:

$$\frac{\partial u^j}{\partial t} + \frac{\partial f_i^j}{\partial u^k}\frac{\partial u^k}{\partial x^i} = 0. \qquad j = 1,\ldots,n \tag{3.19}$$

The index i ranges up to the number of independent variables not including time; the index k ranges over the number of n unknowns. This notation is closely connected to matrix notation. This can be seen by identifying u as well as the partial derivative factors in the terms with matrices. Let W be a column vector of the unknowns. Then the following matrices

$$W_t = \begin{bmatrix} \frac{\partial u^1}{\partial t} \\ \frac{\partial u^2}{\partial t} \\ \vdots \\ \frac{\partial u^n}{\partial t} \end{bmatrix} \qquad A_i = \frac{\partial f_i^j}{\partial u^k} = \begin{bmatrix} \frac{\partial f_i^1}{\partial u^1} & \frac{\partial f_i^2}{\partial u^1} & \cdots & \frac{\partial f_i^n}{\partial u^1} \\ \frac{\partial f_i^1}{\partial u^2} & \frac{\partial f_i^2}{\partial u^2} & \cdots & \frac{\partial f_i^n}{\partial u^2} \\ \vdots & \vdots & & \vdots \\ \frac{\partial f_i^1}{\partial u^n} & \frac{\partial f_i^2}{\partial u^n} & \cdots & \frac{\partial f_i^n}{\partial u^n} \end{bmatrix} \qquad W_x i = \begin{bmatrix} \frac{\partial u^1}{\partial x^i} \\ \frac{\partial u^2}{\partial x^i} \\ \vdots \\ \frac{\partial u^n}{\partial x^i} \end{bmatrix} \tag{3.20}$$

lead to the compact matrix representation

$$W_t + A_i W_x i = 0 \tag{3.21}$$

for a system of n equations with the implied sum over each of the i independent variables other than time; the matrix A_i is an n by n matrix. This notation is quite prevalent in the literature. The reason for introducing the system of quasi-linear equations is that the Euler equations are such a set of equations and the equation that will be solved herein is a limiting case of them.

The Euler equations can easily be written in vector form for two-dimensional unsteady flow with velocity components u and v in the respective directions of x and y as

$$W_t + F_x + G_y = 0 \tag{3.22}$$

where

$$W = \begin{bmatrix} \rho \\ \rho u \\ \rho v \\ \rho\left(\frac{1}{2}q^2 + e\right) \end{bmatrix}, \quad F = \begin{bmatrix} \rho u \\ \rho u^2 + p \\ \rho uv \\ \rho u\left(\frac{1}{2}q^2 + h\right) \end{bmatrix}, \quad G = \begin{bmatrix} \rho v \\ \rho uv \\ \rho v^2 + p \\ \rho v\left(\frac{1}{2}q^2 + h\right) \end{bmatrix}$$

and ρ is the density. Here, e is the specific internal energy and h is the specific enthalpy for an ideal gas and $q^2 = u^2 + v^2$. The pressure is given by the equation of state $p = \rho RT$ for a perfect gas at temperature T, where R is the universal gas constant. Obviously F and G take on the role of f^i_j for $i = 1$ and $i = 2$, corresponding to the flux in the x and y directions, respectively. The attached subscripts denote partial differentiation with respect to the indicated variable. For isentropic flows, the pressure is related solely to the density through the relationship $p\rho^{-k} = \text{constant}$ where k is the ratio of specific heats. The Euler equations then simplify such that W, F, and G reduce to only their first three elements.

The jump conditions relating the upstream and downstream states adjacent to a shock are given by Lax (Ref. 29) as

$$v_s\left[u^j\right] = \left[\bar{f}^j\right] \cdot \hat{n} \tag{3.23}$$

for a smooth shock surface moving with speed v_s. The notation is the same as that used for Eq. (3.15); however, the brackets indicate the jump values of the enclosed quantities occurring across the shock. The value of the shock speed v_s is limited above by the speed of sound preceding the shock, and bounded below by the speed of sound on the high

pressure side. This guarantees that the shock will experience an entropy increase rather than a decrease, a feature that the Rankine-Hugoniot relations fail to discriminate. Since the initial conditions are not sufficient in themselves to determine a unique solution, these are the supplemental conditions needed to correctly specify a shock. Failure to use either the correct conservation equations or the conservation form leads either to incorrect shock speeds or strengths.

The process of calculating the position of a shock and the subsequent application of the Rankine-Hugoniot relations is known as shock fitting. The use of shock fitting provides an accurate method of handling shocks and it also provides sharp resolution since they are treated as discontinuities. Shock fitting procedures were used as early as the year 1948 by Emmons (Ref. 31) who used a somewhat different approach in establishing shock jump conditions for flow over airfoils. The direct application of these fitting techniques is handicapped since the positions describing a shock surface must be calculated, often resulting in lengthy trial and error procedures. This is particularly troublesome since, in general, a shock moves through the medium along an undetermined path. Numerical schemes which fit shocks frequently exploit the theory of characteristics since certain quantities are constant, or nearly so, along the characteristic directions.

The notion of characteristics which was mentioned above in regard to first order equations plays an important role in the development and understanding of numerical methods for systems of hyperbolic equations. To see how the theory of characteristics enters, it will be simply stated that the matrix for the system of equations in Eq. (3.21) can be transformed by multiplying it by a linear matrix which results in an

equivalent set of equations which have an interesting property. This property is that each of the resulting equations contain differentiation in a single direction. This is called the normal form for a system of hyperbolic equations. The directions of differentiation are the familiar characteristic directions which were presented above in the more easily understood form of first order equations with two independent variables. Nevertheless, the characteristics generalize in the case of higher order equations or systems of equations with more than two independent variables; the main difference is the obvious increase in diversity and complexity exhibited when more variables are involved. Higher order equations are often treated as systems of first order equations by introducing extra dependent variables.

For the unsteady one-dimensional Euler equations, three characteristic directions emanate from each point in the fluid. Along these characteristic curves information propagates, either in the form of waves or fluid motion. Sound waves flow along forward and rearward characteristics while particle paths follow a characteristic upon which the entropy is constant and which lies between the other two. For isentropic flow, certain quantities known as Riemann invariants can be constructed from the fluid variables such that one is constant for the forward characteristic and another for the rearward direction. These directions are sketched in Fig. 3.5. Signals reaching a point N, which just happens to coincide with a lattice point in the flow, have paths labeled λ^+ and λ^- representing the forward and rearward characteristics, respectively. In general, the characteristics do not follow paths connecting grid points. For nonisentropic flow, quantities

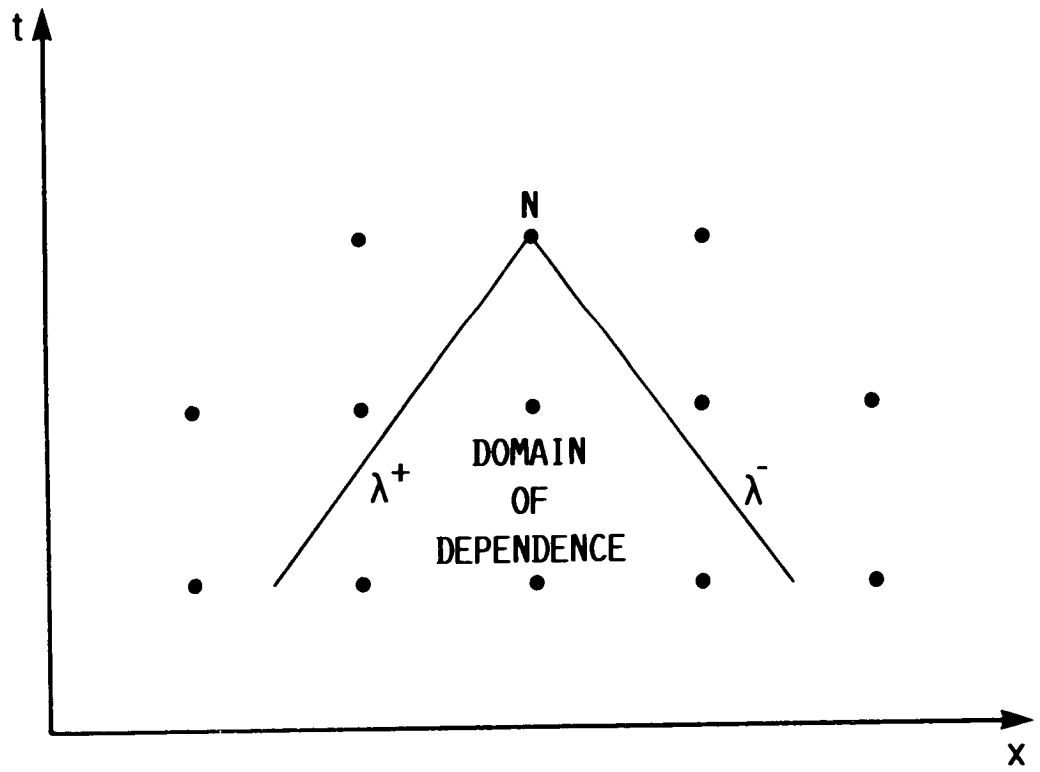

FIGURE 3.5. - DOMAIN OF DEPENDENCE FOR POINT N LIES BETWEEN CHARACTERISTICS.

analogous to the Riemann invariants can be defined which are approximately constant, at least for small time periods.

The fact that initial data propagated along characteristic directions determine the nearby solution to such hyperbolic problems leads to the important concept of domain of dependence. Data outside the characteristic rays shown in Fig. 3.5 cannot influence the solution at point N. Only data within the region influences the solution. This region is called the domain of dependence. Similarly, the characteristics leaving a point at time t will define a domain influenced by that point later on. It is important for stability reasons that these domains be respected while carrying out the finite difference calculations. The time-step must be adjusted to the spatial grid interval so that the analytical domain of dependence is contained within the computational domain of dependence. This restricts the maximum time-step on the basis of qualitative physical arguments. For example, inspection of Fig. 3.6 reveals that information from the three circled grid points at time level t would suffice to provide all necessary data for point N at time $t + \Delta t$. The computational domain, which is represented as straight dashed lines, contains the physical domain of dependence framed by the solid lines. For double the time-step, say in the absence of information at time t, then five grid points of data at time $t - \Delta t$ would contain all the information influencing point N. The region between the solid and dashed lines on each side of the domain of dependence represents information which is not needed at point N but which it sees nevertheless. This transfer of spurious data will occur as long as the characteristics do not connect the grid points; in general they do not and, consequently, loss of

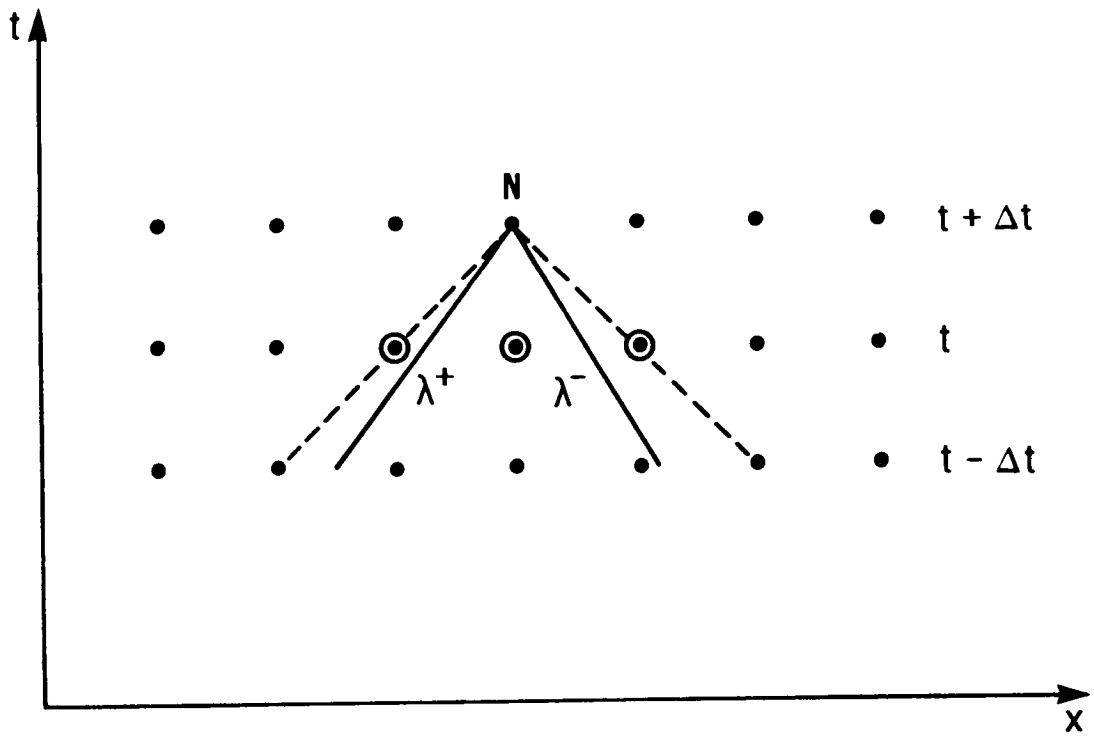

FIGURE 3.6. - NUMERICAL DOMAIN MUST CONTAIN THE PHYSICAL DOMAIN OF DEPENDENCE FOR STABILITY.

accuracy results. The domain of dependence principle places a qualitative restriction on the time-step. This is of special importance to explicit numerical schemes. Implicit schemes have the advantage that time-step limitations imposed for stability may be relieved or removed altogether. In any case, stability requirements are usually not available for a nonlinear problem but hopefully estimates can be acquired from a linear counterpart or numerical experiment.

Further inspection of the domain of dependence is required in the instance of embedded shocks. To illustrate this case, Fig. 3.7 presents a sketch similar to those just reviewed but which now includes a shock path in the computational plane. Assuming the flow to be supersonic on the left (the upstream side) of the shock and subsonic on the right, two sets of characteristics can be identified with points N and N+1 residing in the supersonic and subsonic zones, respectively. In the supersonic zone, it is clear that all soundwaves travel downstream, and hence, both λ-characteristics have positive slopes; i.e., they both propagate downstream. For the subsonic zone, one characteristic points upstream and one downstream. Information affecting a supersonic point must come from the upstream direction, commonly referred to as the upwind direction. Subsonic points are influenced by signals from each direction. Finite difference schemes take this into account by upwind differencing at supersonic points and central differencing at subsonic points. Details differ for various schemes on the means of switching from one type of differencing to the other when the flow changes from supersonic to subsonic.

A novel scheme was recently introduced by Moretti (Ref. 32) who was inspired by the physical implications of the method of characteristics.

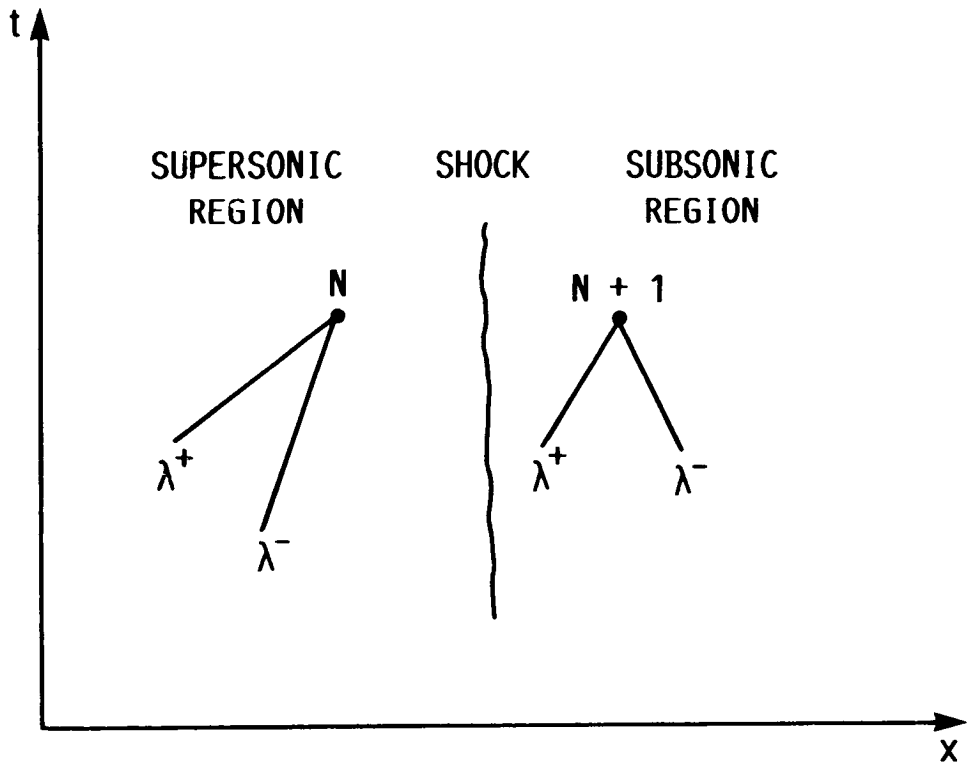

FIGURE 3.7. - CHARACTERISTIC DIRECTIONS FOR FLOW WITH EMBEDDED SHOCK.

The scheme is a second order accurate method capable of tracking weak shocks and is currently being improved, with initial testing being conducted mainly on unsteady problems in two space dimensions. It is appropriately called the λ-scheme and employs shock fitting to specify the entropy jump and to correct the shock speed for shocks that are initially predicted as being isentropic. Other investigators have made contributions to this technique, in particular Zannetti (Ref. 33) who introduced the use of generalized Riemann invariants. Still, while the method offers hope of accurately tracking and computing shocks, its forthwith use for three-dimensional flows has yet to be demonstrated. The difficulties in using shock fitting procedures for complicated flows encouraged efforts for alternative methods.

An alternative method which models the dissipative nature of shocks was introduced by von Neumann and Richtmyer (Ref. 34). Their approach was to add terms, mocking the physical effects of viscosity, to the one-dimensional unsteady inviscid flow equations. This was done in a discriminatory fashion by prescribing the additional terms as nonlinear functions of the dependent variables which have the following three features: to act in a strong manner at a shock location; to have a weak effect away from the shock; and to remain compatible with the Rankine-Hugoniot relations for shocks sufficiently thin when compared to the characteristic flow dimensions. The overall effect of this approach was to smear any shock smoothly over an interval of distance rather than produce a sharp discontinuity. The thickness of a typical smeared shock is on the order of the grid size interval which theoretically can be as fine as desired, though practical considerations limit the spacing refinement. The thermodynamic variables therefore acquire a continuous

but rapid variation in place of a sharp jump across a shock. Since these terms are arrived at based only on considerations of physical reasonableness rather than exact laws, a certain amount of arbitrariness is introduced; this would likely be compounded in generalization to higher dimensions. It should also be emphasized that the modifications introduced by including these dissipative terms is purely a mathematical artifice and the success of the technique relies on properly specifying the amount and distribution of artificial viscosity. The inclusion of physically reasonable, yet artificial, terms to provide treatment of a shock discontinuity illustrates a prevalent circumstance appearing variously in computational applications; namely, the acceptance of some loss in one property for a gain in another. Here this occurs with a highly simplified treatment of shocks being obtained at the expense of introducing some numerical error into the solution by using somewhat arbitrarily defined dissipative terms.

The introduction of artificial viscosity preceded the advent of the high speed computer but was recognized, along with other developments in numerical methods, as being most useful with automatic computing capability. The rapid growth in computer capabilities signaled a trend toward application of highly simplified procedures suitable for repetitive machine calculation. The stage was set for numerical calculation of nonlinear flows with shocks. The amount of numerical work dealing with transonic flows is overwhelming and precludes any complete review here. A number of excellent surveys of developments in transonic flows have been made (Refs. 35 to 39. Therefore, only a brief review will be given to highlight certain key aspects. As in the case of analytical treatment of propeller theory, it is useful and convenient

to sketch the numerical approach by focusing on the numerical developments associated with wing applications. Most of the fundamental advances in the numerical treatment of external transonic flows have come about largely due to procedures devised to predict steady and unsteady flows over airfoils. These flows possess the characteristics listed above and yet offer examples simple enough to be treated directly with various techniques. This quality affords the opportunity to compare the numerical results and lend credibility to them; also, experimental data or exact analytical solutions for restricted cases can often be obtained to qualify or corroborate the numerical results.

An appropriate beginning for the discussion of transonic flows over airfoils is the work of Magnus and Yoshihara (Ref. 40). This work represents the first direct finite-difference procedure for transonic flow with embedded shock waves. The unsteady Euler equations, expressed in conservation form, were used to solve two-dimensional, steady, supercritical flows about lifting airfoils. These unsteady equations were numerically approximated using a modified Lax-Wendroff finite-difference technique. Steady solutions were obtained by allowing the unsteady solutions to converge to a time-dependent state. The advantage in treating a steady flow as a limit of an unsteady one is that the steady equations are a mixed elliptic-hyperbolic system whereas the unsteady equations are hyperbolic. The gain realized from this uniformity of equation type more than offsets the increase in complexity caused by adding time as another independent variable. This approach especially simplified the problem since the locations where the steady flow equations switch type are unknown and must be found as part of the solution process. Use of the unsteady formulation eliminates the need

to devise distinct numerical schemes particular to the subsonic and supersonic regions. Of considerable importance was their method of introducing numerical viscosity. They introduced artificial viscosity in two separate ways. One of the ways diffusion was introduced arises from the formulation of the second order differencing scheme. Lower order terms in the truncation error are retained which behave similarly to real viscosity by reducing all gradients in the solution. The higher gradient locations naturally were affected more than the lower ones. This serves the same purpose as the artificial viscosity introduced by von Neumann and Richtmyer in that it automatically captures a shock as a high gradient region joining regions of strongly dissimilar flows. A second way of introducing damping terms was brought about by using spatially weighted averages of the dependent variables in the leading terms of the Taylor series expansions expressing the updating of these variables. The numerical viscosity can be reduced in each case by refining the grid since the the damping terms are in fact truncation error terms. A trade-off is reached between stability and accuracy. The solutions obtained were quite time consuming, in good part due to the absence of a suitable grid, but served as benchmarks for more approximate calculations to follow.

Murman and Cole approached the transonic flow problem along the lines of small perturbation analysis. They first solved a simplified form of the two-dimensional steady transonic equation

$$\frac{1}{2}\left(\varphi_x^2\right)_x - \varphi_{yy} = 0 \tag{3.24}$$

for the perturbation potential φ with what was later realized as not being a fully conservative scheme (Ref. 41), and subsequently with a nearly fully conservative scheme (Ref. 42) in which the correct shock

jump condition was obeyed, at least in practice as evidenced by the results. The perturbation potential is the velocity potential minus the free stream potential. Here, and in what follows, the x coordinate is in the free-stream direction; the y direction is normal to the free-stream flow. The use of a perturbation technique limits these efforts to thin airfoils but greatly simplifies the boundary condition treatment at the airfoil surface. They used an iterative line relaxation procedure to sweep downstream along successive grid lines aligned transverse to the flow. Over-relaxation was used in the subsonic regions of the flow. The use of the successive line over-relaxation (SLOR) procedure improved the computational efficiency by about an order of magnitude over that of Magnus and Yoshihara.

The use of such a straightforward procedure for the calculation of mixed flow was possible due to their type-dependent differencing scheme. This was their main contribution and is carried out as follows. During the course of the calculation, the velocity at each grid point along the relaxation line under consideration is compared with the speed of sound. If the velocity is supersonic, that point is implicitly backward (upwind) differenced in the streamwise direction. If the velocity is subsonic, central differencing is used. This type-dependent differencing respects the domain of dependence and furthermore, proved simple to implement. An important development was included in the fully conservative scheme which significantly improved the shock calculations. A special difference operator was introduced which was used at grid points where the flow decelerates through the speed of sound (ruling out any supersonic-to-supersonic shocks). The difference operator thus operates at shock points and is called a shock-point operator. It

should also be mentioned that a switching operator (Ref. 43) is used at sonic points, where the flow accelerates through the speed of sound. The sonic operator poses no special problem since the flow is continuous at sonic points. However, it should be emphasized that four operators exist as follows: a central operator at subsonic points; an upwind operator at supersonic points; a sonic operator; and a shock-point operator. The shock-point operator effectively switches the difference scheme from the implicit backward hyperbolic operator upstream of the shock to the centrally differenced elliptic operator past the shock in such a manner that the combination of all three operators is fully conservative.

This switching procedure can be looked at from a flux viewpoint by imagining the grid points to be enclosed by corresponding cells packed tightly. Use of the switching operator balances the flux internally so that for any contiguous group of grid cells, the net flux of a quantity at their external border is zero. Since the initial type-dependent scheme lacked the shock-point operator, flux was not necessarily conserved at the internal shock boundaries and consequently the scheme was not fully conservative even when the derivatives were otherwise placed in conservation form.

Several codes have originated based on the Murman and Cole method. The first one developed was by Krupp and Murman (Ref. 44) which used the nonconservative form of the difference equations. Murman, Bailey, and Johnson (Ref. 45) later developed a code (TSFOIL) using the fully conservative form of the difference equation given by

$$\left[\left(1 - M_\infty^2\right)\varphi_x - \frac{k+1}{2} M_\infty^d \varphi_x^2\right]_x + \varphi_{yy} = 0 \qquad (3.25)$$

or, in a general form, with the physical variables scaled, written as

$$\left(K\tilde{\varphi}_{\tilde{x}} - \frac{k+1}{2}\tilde{\varphi}_{\tilde{x}}^2\right)_{\tilde{x}} + \tilde{\varphi}_{\tilde{y}\tilde{y}} = 0. \tag{3.26}$$

The relations between the physical and scaled variables are given as follows:

$$\begin{aligned} \tilde{\varphi} &= \delta^{-2/3} M_\infty^n \varphi \\ \tilde{y} &= \delta^{1/3} M_\infty^m y \end{aligned} \tag{3.27}$$

where

$$K = \frac{1 - M_\infty^2}{M_\infty^{2m}\delta^{2/3}} .$$

The variable δ is the airfoil thickness ratio, M_∞ is the free-stream Mach number, and k is the ratio of specific heats. The constants d, m, and n are the similarity parameters chosen to give the desired form of the small disturbance equation. When d = m = n = 0, the Cole form (Ref. 46) is obtained. The Sprieter form (Ref. 47) is given by defining d = 2 and m = n = 2/3. Finally, the Krupp form (Ref. 48) is obtained by selecting d = 7/4, m = 1/2, and n = 3/4. The Cole choices for the transonic similarity parameters are based on mathematical simplicity. The Spreiter and Krupp choices are made to give accurate approximations over a wide range of free-stream velocity and thickness ratio. The conservative form of the equations produce shocks with nearly the correct strength and speed. Nonconservative formulations exhibit the fortuitous feature of having the shock position displaced upstream accompanied by a smaller pressure drop across the shock, more in agreement with experimental viscous measurements. Such features make the nonconservative results more appealing to some airfoil designers.

A few loopholes present in the Murman-Cole shock operator were closed with the simple modifications made by Engquist and Osher (Ref. 49). They not only analyzed the two-dimensional small disturbance equation, Eq. (3.26), but solved the time-dependent form:

$$\left(K\tilde{\varphi} - \frac{k+1}{2}\tilde{\varphi}_x^2\right)_x + \tilde{\varphi}_{yy} - 2\tilde{\varphi}_{xt} = 0. \tag{3.28}$$

Convergence to the steady state was reached after a sufficient number of iterations.

Artificial viscosity was not added by design in the numerical formulations of the type dependent schemes mentioned above. However, enough is generated due to the upwinding operators that shocks are captured over 3 or 4 mesh widths using the Murman-Cole scheme and over 1 or 2 mesh widths using the Engquist-Osher scheme. The use of type dependent differencing destroys the symmetry that would otherwise occur in the equations and which would admit expansion shocks as well as compression shocks.

The SLOR procedure used by Murman and Cole was replaced by approximate factorization (AF) procedures by Ballhaus and Steger (Ref. 50) in their investigation of the low frequency form for the transonic small disturbance equation which is given in the form

$$2\frac{\omega\ell}{U_\infty}M_\infty^2\tilde{\varphi}_{xt} = V_c\tilde{\varphi}_{xx} + \tilde{\varphi}_{yy} \tag{3.29}$$

for an airfoil of chord ℓ undergoing periodic motion of frequency ω. The free-stream velocity is U_∞ and $V_c = 1 - M_\infty^2 - (k+1)M_\infty^m\varphi_x$. The flow is locally subsonic or supersonic when V_c is positive or negative, respectively. The ratio $\omega\ell/U_\ell$ determines the time scale and is called the reduced frequency. It relates the time a mean fluid particle takes

to traverse the length of a chord to the time required for one blade oscillation. The appearance of the reduced frequency is attributed to the fact that in Eq. (3.29) the variables $\tilde{\varphi}$, x, $\tilde{y}$, and t are additionally scaled by ℓU_∞, ℓ, ℓ, and $1/\omega$, respectively. This low frequency form of the equation is valid for reduced frequencies much less than one. For most transonic flows the low frequency equation is adequate since the low frequencies associated with the slowly moving upstream waves dominate the solution near the airfoil. The higher frequency waves travel quickly downstream and do not have a chance to build into strong waves. Fortunately, the low frequency oscillations are adequately analyzed with coarser time steps than those for high frequencies. For this reason Ballhaus and Steger examined implicit and semi-implicit numerical schemes that would allow them to remove the time-step limitations of explicit schemes so that larger time steps could then be taken which were limited only by accuracy considerations. The AF procedures were introduced to reduce the computational work required by SLOR techniques. The AF procedures split the difference equations into simple factors which are easily invertible. The factors are usually solvable by tridiagonal or quadridiagonal algorithms such as the Thomas algorithm. Among the schemes studied was the ADI method developed by Peaceman and Rachford for the two-dimensional Laplace equation and extended to multi-dimensions by Douglas and Gunn (Refs. 51 to 52). The ADI scheme was shown to be an AF type scheme. The stability of the schemes was compared and their shock capturing features were examined.

The ADI technique developed by Douglas and Gunn was used in the numerical solution of the unsteady, three-dimensional flow about

helicopter rotors (Refs. 1 to 5) using the small disturbance approach. A numerical code was written and used to analyze the flow in the transonic tip region of the rotor blades. The strong similarity in the form of the helicopter equation to that of the propeller problem led to the adoption of the code, with some modifications, for the present effort.

IV. GOVERNING EQUATION

This chapter presents the potential equation and the development of an approximation to it which is valid for small disturbance flow about thin, lightly loaded propeller blades. First, the general potential equation in an inertial coordinate system will be developed for isentropic flow of a perfect gas with no other approximations made. Then this equation will be transformed to streamwise coordinates. The potential equation in rotating coordinates will then be given as developed in (Ref. 5) for a coordinate system attached to a helicopter blade. Following this, the equivalent tensor equation valid for any coordinate system will be presented for an accelerated system. Finally, the small perturbation equation for generalized helical coordinates will be derived.

4.1 Potential Equation in an Inertial Coordinate System

Consider a flow with uniform upstream velocity U_∞ directed along the X-axis where X, Y, and Z are Cartesian coordinates with corresponding velocity components u, v, and w. The continuity equation can be written in the expanded form as

$$\rho_t + u\rho_X + v\rho_Y + w\rho_Z + \rho(u_X + v_Y + w_Z) = 0. \tag{4.1}$$

Bernoulli's equation for unsteady flow can be expressed in a form giving the speed of sound c as a variation from its upstream speed c_∞ as

$$c^2 = c_\infty^2 - \frac{k+1}{2}(2\Phi_t + \Phi_X + \Phi_Y + \Phi_Z) \tag{4.2}$$

where the scalar Φ is the velocity potential defined through the following components:

$$u = \frac{\partial \Phi}{\partial X} ; \qquad v = \frac{\partial \Phi}{\partial Y} ; \qquad w = \frac{\partial \Phi}{\partial Z} . \tag{4.3}$$

Thus, the fluid velocity is given by

$$\bar{q} = \nabla \Phi. \tag{4.4}$$

For isentropic flow, the density and speed of sound are connected by the relation

$$\frac{\rho}{\rho_\infty} = \left(\frac{c}{c_\infty}\right)^{2/(k-1)} . \tag{4.5}$$

This relation can be used to eliminate the density in Eq. (4.1). Using Eq. (4.5), performing the differentiation in the first four terms in Eq. (4.1), and multiplying the result by c^2/ρ yields

$$\frac{1}{k+1}\left[(c^2)_t + u(c^2)_X + v(c^2)_Y + w(c^2)_Z\right] + c^2(u_X + v_Y + w_Z) = 0. \tag{4.6}$$

Bernoulli's equation, written for an unsteady flow in Eq. (4.2), can be used to introduce the velocity potential into Eq. (4.6); replace c^2 in the equation using Eq. (4.2), and carrying out the indicated differentiation yields

$$\begin{aligned} &\Phi_{tt} + u\Phi_{Xt} + v\Phi_{Yt} + w\Phi_{Zt} + u(\Phi_{Xt} + u\Phi_{XX} + v\Phi_{XY} + w\Phi_{XZ}) \\ &\quad + v(\Phi_{Yt} + u\Phi_{XY} + v\Phi_{YY} + w\Phi_{YZ}) + w(\Phi_{Zt} + u\Phi_{XZ} + v\Phi_{YZ} + w\Phi_{ZZ}) \\ &\quad - c^2(\Phi_{XX} + \Phi_{YY} + \Phi_{ZZ}) = 0. \end{aligned} \tag{4.7}$$

Rearranging terms yields a more symmetrical equation, viz.,

$$\begin{aligned} &\Phi_{tt} + 2u\Phi_{Xt} + 2v\Phi_{Yt} + 2w\Phi_{Zt} + (u^2 - c^2)\Phi_{XX} + (v^2 - c^2)\Phi_{YY} \\ &\quad + (w^2 - c^2)\Phi_{ZZ} + 2uv\Phi_{XY} + 2uw\Phi_{XZ} + 2vw\Phi_{YZ} = 0. \end{aligned} \tag{4.8}$$

Various approximations can be made to Eq. (4.8) which itself is an exact equation. For example, dividing it by c^2 and allowing c to approach infinity reduces the equation to $\nabla^2\Phi = 0$ for an incompressible flow. Similarly, other approximations can be made by removing cubic and even quadratic terms. As another example, in the case of acoustic theory, a linear equation results for the subsonic and supersonic regimes by neglecting certain terms and letting the quantities c and u assume their free-stream values c_∞ and U_∞; whereas a separate equation is obtained for the transonic regime since local effects are more dominant, requiring retention of the local values of c and u. Most approximate equations derived from Eq. (4.8) are produced for the purposes of linearization. However, the goal here is to arrive at an approximation that is consistent with this equation in the limit of small disturbances, yet valid for nonlinear transonic flows.

4.2 Potential Equation in Streamwise Coordinates

Before beginning our discussion of the disturbance potential for the propeller problem, it is worthwhile to present Eq. (4.8) using streamwise coordinates. First, the magnitude of the total velocity vector q is given as

$$\bar{q} = \left(u^2 + v^2 + w^2\right)^{1/2}. \tag{4.9}$$

For any directional coordinate s, the directional derivative along s is simply

$$\frac{\partial}{\partial s} = \frac{\partial}{\partial X}\frac{dX}{ds} + \frac{\partial}{\partial Y}\frac{dY}{ds} + \frac{\partial}{\partial Z}\frac{dZ}{ds}. \tag{4.10}$$

By referring to Fig. 4.1, it can be seen that dX/ds, dY/ds, and dZ/ds are the direction cosines which equal u/q, v/q, and w/q, respectively, if s is a streamline. The second directional derivative is defined as

$$\frac{\partial^2\Phi}{\partial s^2} = \Phi_{ss} = \frac{1}{q^2}\left(u^2\frac{\partial^2\Phi}{\partial X^2} + v^2\frac{\partial^2\Phi}{\partial Y^2} + w^2\frac{\partial^2\Phi}{\partial Z^2} + 2uv\frac{\partial^2\Phi}{\partial X\partial Y} + 2uw\frac{\partial^2\Phi}{\partial X\partial Z} + 2vw\frac{\partial^2\Phi}{\partial Y\partial Z}\right). \quad (4.11)$$

Furthermore,

$$\frac{\partial^2\Phi}{\partial s\partial t} = \frac{1}{q}\left(u\frac{\partial^2\Phi}{\partial X\partial t} + v\frac{\partial^2\Phi}{\partial Y\partial t} + w\frac{\partial^2\Phi}{\partial Z\partial t}\right) \quad (4.12)$$

follows directly from Eq. (4.3) when the velocity ratios are inserted as the direction cosines. Substitution of the streamwise derivatives given by Eqs. (4.11) and (4.12) into the potential Eq. (4.8) is easily accomplished by grouping the appropriate terms in the latter. This leads to a streamwise formulation of the potential equation given by

$$\Phi_{tt} + 2q\Phi_{st} = (c^2 - q^2)\Phi_{ss} + c^2(\nabla^2\Phi - \Phi_{ss}) \quad (4.13)$$

where $\nabla^2 = \partial^2/\partial X^2 + \partial^2/\partial Y^2 + \partial^2/\partial Z^2$ is the Cartesian Laplacian operator. This takes on a particularly simple form for two-dimensional steady flow, i.e.,

$$(c^2 - q^2)\Phi_{ss} + c^2\Phi_{nn} = 0. \quad (4.14)$$

where Φ_{ss} reduces to

$$\Phi_{ss} = \frac{1}{q^2}\left(u^2\frac{\partial^2\Phi}{\partial X^2} + 2uv\frac{\partial^2\Phi}{\partial X\partial Y} + v^2\frac{\partial^2\Phi}{\partial Y^2}\right) \quad (4.15)$$

and Φ_{nn} represents the second directional derivative normal to the streamwise direction such that the positive direction of n is consistent with Fig. 4.1:

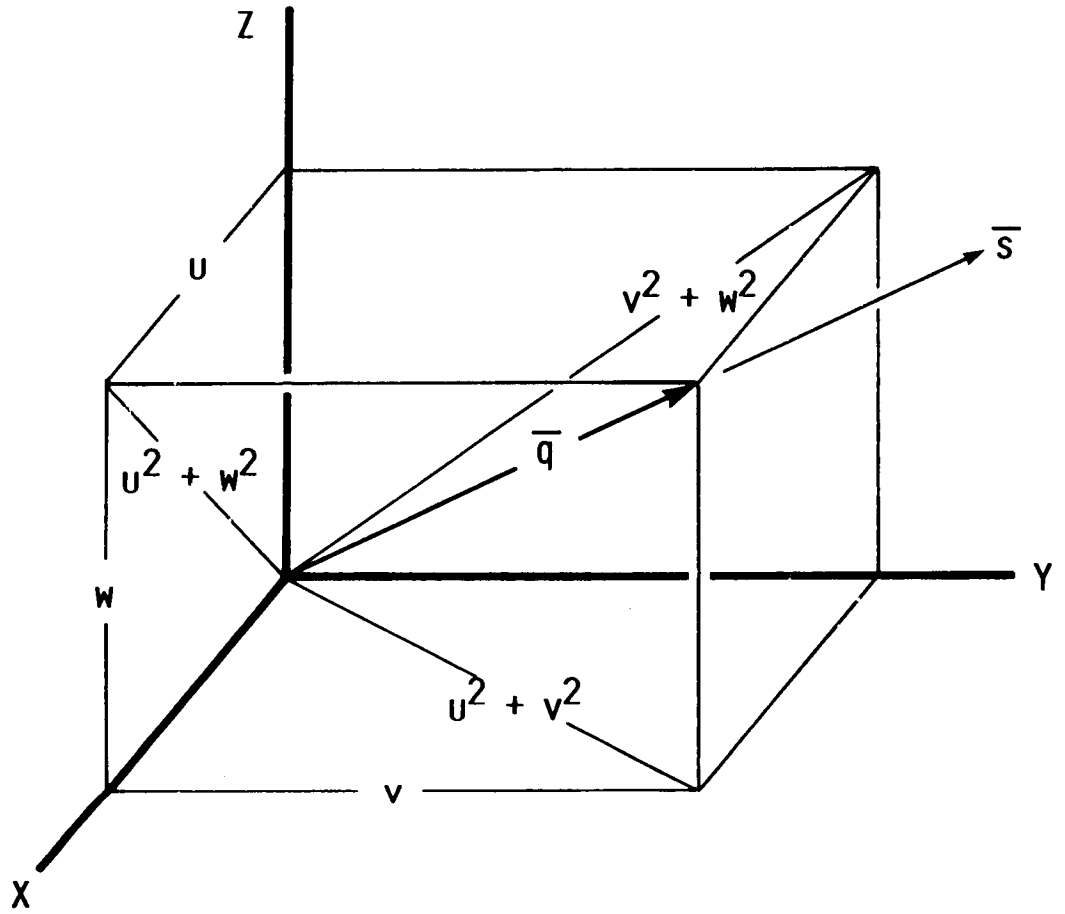

FIGURE 4.1. - DIRECTION COSINES EQUAL u/q, v/q, AND w/q WHEN $\overline{s}$ IS DIRECTED ALONG $\overline{q}$.

$$\Phi_{nn} = \frac{1}{q^2}\left(v^2 \frac{\partial^2\Phi}{\partial X^2} - 2uv \frac{\partial^2\Phi}{\partial X \partial Y} + u^2 \frac{\partial^2\Phi}{\partial Y^2}\right). \qquad (4.16)$$

The use of a coordinate system aligned with the streamwise and normal directions has obvious advantages. The potential equation is considerably simplified when expressed in these coordinates. The troublesome cross-derivative terms which generally complicate the numerical solution and usually adversely effect the convergence rate are removed. Even when streamwise and normal coordinates cannot be used explicitly, they can be expressed locally in terms of the actual coordinates as in Eqs. (4.15) and (4.16) for two-dimensional flow. One marked advantage of doing this is that derivatives can be treated differently in the streamwise and normal directions. In fact, it was for this very reason that Jameson (Ref. 53) introduced his rotated-differences procedure. The use of a streamwise coordinate system allows type dependent differencing schemes, as discussed in the last chapter, to be employed in a straightforward manner. The streamwise direction can be type-dependent differenced and the normal direction can be centrally differenced. The use of rotated differencing allows derivatives to be constructed in the streamwise and normal directions from the Cartesian coordinates. Failure to use a rotated differencing scheme without one coordinate being nearly aligned with the flow direction can lead to instability when supersonic regions are present. The likelihood of instability results from either central differences having a component in the streamwise direction or from upwind differences which may not contain the correct domain of dependence, leading to negative artificial viscosities. This points out a major advantage in using helical coordinates for propeller flow. The

undisturbed flow direction can be aligned with a helical coordinate. This helical direction will be the streamwise direction for which type-dependent differencing can be used.

4.3 Potential Equation in Noninertial System

The potential equation, Eq. (4.8) can be expressed in vector form (Ref. 54) as

$$\Phi_{tt} + \frac{\partial}{\partial t}(\nabla\Phi)^2 + \frac{1}{2}\nabla\Phi \cdot \nabla(\nabla\Phi)^2 = c_\infty^2 - (k-1)\left[\Phi_t + \frac{1}{2}(\nabla\Phi)^2\right]. \qquad (4.17)$$

The potential equation can also be expressed in an xyz coordinate system which is both translating with an arbitrary constant velocity $\bar{V}$ away from the inertial frame, and rotating with an arbitrary constant rotational velocity $\bar{\Omega} \times \bar{r}$. The angular velocity vector $\bar{\Omega}$ (with magnitude Ω) has the direction of the axis through the origin about which xyz are rotating, and $\bar{r}$ is the position vector in this system. The relationship between the two coordinate systems is shown in Fig. 4.2. Although both $\bar{V}$ and $\bar{\Omega}$ are general vectors, they will soon be restricted to a common axial direction in the following development. The rotating system is, of course, not an inertial system. Although such a system introduces extra terms, it offers advantages over fixed coordinates. In particular, for a propeller rotating about an axis aligned with its flight direction, the flow appears steady (ignoring unsteady effects such as flutter) to an observer in a coordinate system rotating with the propeller.

A potential equation can also be established in the noninertial frame for a flow which is irrotational in the inertial frame. This is initiated by defining a perturbation potential φ which separates the contribution of the free-stream from the total potential. The

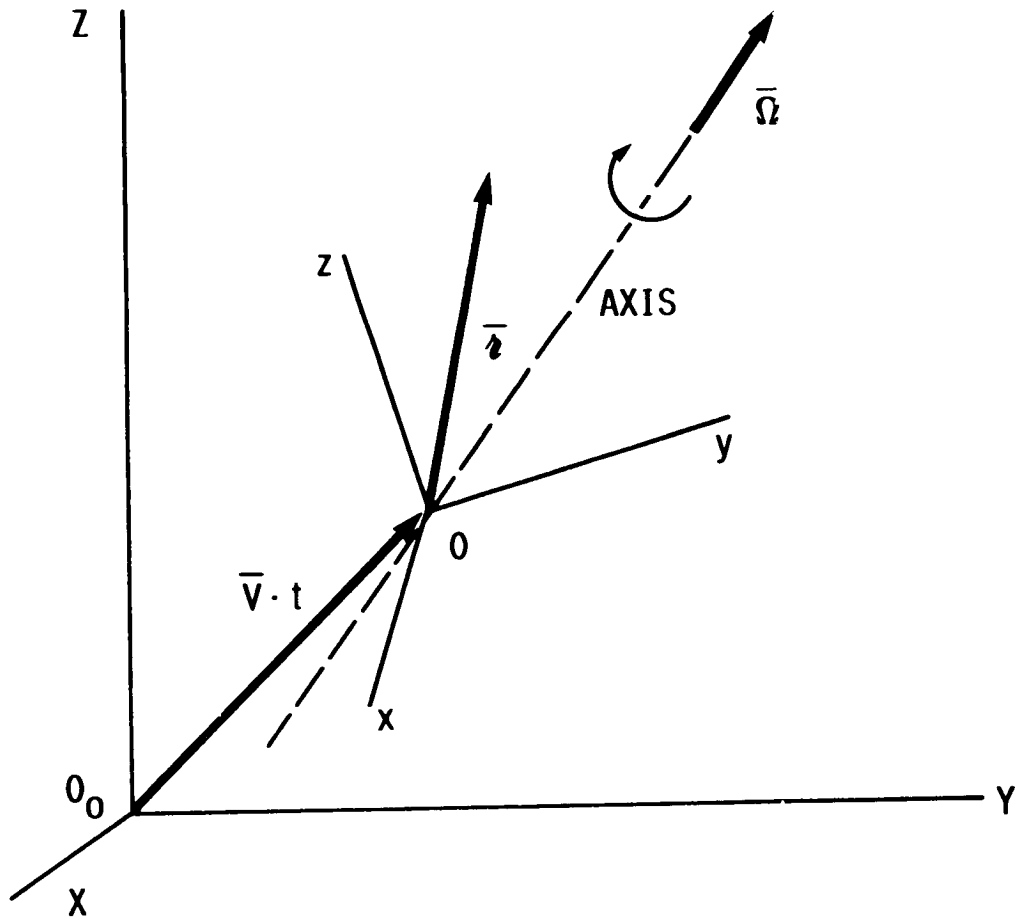

FIGURE 4.2. - RELATIONSHIP BETWEEN INERTIAL COORDINATE SYSTEM XYZ AND NONINERTIAL COORDINATE SYSTEM xyz WHICH IS ROTATING ABOUT AXIS PASSING THROUGH ITS ORIGIN.

freestream contains both uniform flow and bulk rotational flow contributions, consequently

$$\bar{q}' \equiv \nabla\varphi = \bar{q} - (\bar{V} + \bar{\Omega} \times \bar{r}) \tag{4.18}$$

represents the irrotational perturbation velocity. The gradient operator is invariant with respect to choice of Cartesian coordinate systems. The components of the perturbation velocity $\bar{q}'$ are defined as

$$u' = \frac{\partial\varphi}{\partial x} \quad , \quad v' = \frac{\partial\varphi}{\partial y} \quad , \quad w' = \frac{\partial\varphi}{\partial z} \; . \tag{4.19}$$

The transformation of the potential equation has been carried out by Isom (Ref. 5) for a coordinate system translating and rotating with constant, but otherwise arbitrary, $\bar{V}$ and $\bar{\Omega}$. The potential equation in the noninertial system is given as

$$\varphi_{tt} + \bar{a} \cdot \nabla(\nabla\varphi \cdot \bar{a}) + 2\bar{a} \cdot \nabla\varphi_t - \bar{\Omega}x\bar{a} \cdot \nabla\varphi - \frac{\partial\bar{V}}{\partial t} \cdot \nabla\varphi + 2\nabla\varphi \cdot \nabla\varphi_t$$

$$+ \bar{a} \cdot \nabla(\nabla\varphi)^2 = \left\{c_\infty^2 - (k - 1)\left[\varphi_t + \bar{a} \cdot \nabla\varphi + \frac{1}{2}(\nabla\varphi)^2\right]\right\}\nabla^2\varphi \tag{4.20}$$

where $\bar{a}$ is the negative of the vector sum of the translational velocity and the rotational velocity as seen by an observer in the rotating frame. Thus, for such an observer, $\bar{a}$ can be simply written as

$$\bar{a} = -(\bar{V} + \bar{\Omega} \times \bar{r}). \tag{4.21}$$

It should be pointed out that in the transformation from the potential equation for an inertial reference frame, Eq. (4.17), to the potential equation for a noninertial frame, Eq. (4.20), the cubic term, on the left-hand side of Eq. (4.17), was dropped. Otherwise, Eq. (4.20) is an exact equation. Introduction of the perturbation potential does not, in itself, imply any approximations.

4.4 Potential Equation in Noninertial Curvilinear Coordinate System

Application of Eq. (4.20) to the propeller problem can be carried out by further simplification in much the same manner as was done in deriving the small disturbance equations for the helicopter problem. However, since the helical coordinate systems which will be used for the propeller problem are nonorthogonal, the potential equation, Eq. (4.20) is more tractable if expressed in invariant tensor form. For a translational velocity $\overline{V}$ which is independent of time, it has the form

$$\frac{\partial^2\varphi}{\partial t^2} + a^i \frac{\partial}{\partial y^i}\left(a^j \frac{\partial\varphi}{\partial y^j}\right) + 2a^i \frac{\partial^2\varphi}{\partial y^i \partial t} - \frac{1}{2}\varepsilon^{ijk}(\Omega_j a_k - \Omega_k a_j)\frac{\partial\varphi}{\partial y^i}$$

$$+ \frac{\partial}{\partial t}\left(g^{ij}\frac{\partial\varphi}{\partial y^i}\frac{\partial\varphi}{\partial y^j}\right) + a^i \frac{\partial}{\partial y^i}\left(g^{jk}\frac{\partial\varphi}{\partial y^j}\frac{\partial\varphi}{\partial y^k}\right) = \left\{c_\infty^2 - (k-1)\left[\frac{\partial\varphi}{\partial t} + a^i\frac{\partial\varphi}{\partial y^i}\right.\right.$$

$$\left.\left. + \frac{1}{2}g^{ij}\frac{\partial\varphi}{\partial y^i}\frac{\partial\varphi}{\partial y^j}\right]\right\}\left[g^{ij}\frac{\partial^2\varphi}{\partial y^i \partial y^j} + \frac{1}{\sqrt{g}}\frac{\partial}{\partial y^i}(\sqrt{g}\, g^{ij})\frac{\partial\varphi}{\partial y^i}\right]. \qquad (4.22)$$

In this equation a^i and a_i represent the contravariant and covariant components, respectively, of the general velocity vector $\overline{a}$ defined by Eq. (4.21). The quantities g^{ij} are the contravariant components of the metric tensor for the transformation between the curvilinear coordinates y^i and our orthogonal Cartesian coordinates. The quantity g is the determinant of the corresponding covariant components g_{ij} which do not appear explicitly in the equation. The symbol ε^{ijk} is the permutation symbol which equals zero for repeating values of i,j,k, unity for cyclic (even) permutations of $1,2,3$, and negative unity otherwise.

4.5 Potential Equation in Helical Coordinates

Equation (4.22), expressed in terms of a rotating coordinate system, can be simplified considerably by choosing one of the

curvilinear coordinates to be in the direction of the vector $\bar{a}$. From Eq. (4.21), this is seen to be the direction opposite the vector sum of the translational velocity and rotational velocity which we now take to be orthogonal such that $\bar{V}$ is aligned with the axis of rotation as shown in Fig. 4.3. With this arrangement the vector $\bar{a}$ is in the direction of the free-stream velocity vector as it appears to an observer whose frame of reference rotates with the blade. In this instance the magnitude of $\bar{a}$ will be designated by U such that it may be written in matrix form as

$$\bar{a} = \begin{bmatrix} U \\ 0 \\ 0 \end{bmatrix} . \tag{4.23}$$

Also,

$$U^2 = (\Omega r)^2 + V^2, \tag{4.24}$$

where r is the radial distance as measured from the axis of rotation. Equation (4.22) then simplifies to

$$\frac{\partial^2\varphi}{\partial t^2} + U^2 \frac{\partial^2\varphi}{(\partial y^1)^2} + 2U \frac{\partial^2\varphi}{\partial y^1 \partial t} - \frac{1}{2}\Omega^2 y^2 \frac{\partial\varphi}{\partial y^2} + \frac{\partial}{\partial t}\left(g^{ij} \frac{\partial\varphi}{\partial y^i} \frac{\partial\varphi}{\partial y^j}\right)$$

$$+ U \frac{\partial}{\partial y^1}\left(g^{jk} \frac{\partial\varphi}{\partial y^j} \frac{\partial\varphi}{\partial y^k}\right) = \left\{c_\infty^2 - (k-1)\left[\frac{\partial\varphi}{\partial t} + U \frac{\partial\varphi}{\partial y^1} + \frac{1}{2} g^{ij} \frac{\partial\varphi}{\partial y^i} \frac{\partial\varphi}{\partial y^j}\right]\right\}$$

$$\times \left[g^{ij} \frac{\partial^2\varphi}{\partial y^i \partial y^j} + \frac{1}{\sqrt{g}} \frac{\partial}{\partial y^i}\left(\sqrt{g}\, g^{ij}\right) \frac{\partial\varphi}{\partial y^j}\right]. \tag{4.25}$$

4.6 Approximate Potential Equation in Scaled Helical Coordinates

Equation (4.25) is exact in that it is equivalent to Eq. (4.20), but expressed in a blade-fixed reference system. However, this equation is much too complicated to be solved efficiently. Therefore, a systematic simplification is necessary to arrive at an approximation

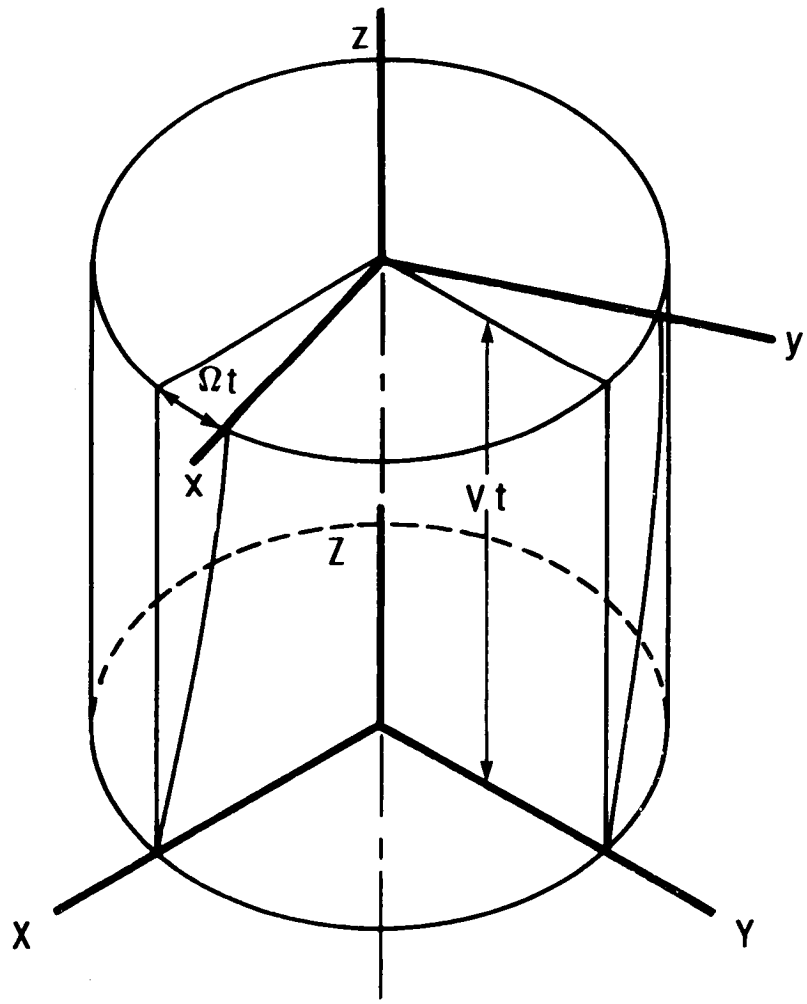

FIGURE 4.3. - NONINERTIAL COORDINATE SYSTEM WITH AXIS ALIGNED WITH INERTIAL SYSTEM.

which retains the nonlinear features of the problem and which is valid for small disturbances about the mean flow. Starting from Eq. (4.20), such a procedure was carried out by Isom (Ref. 5) using Cartesian coordinates for flow about the tip region of a helicopter blade. Following the development of the approximate equation for the helicopter problem, a similar process is applied to Eq. (4.22) for the case of a propeller blade using helical coordinates. The use of helical coordinates introduces the metric tensor into the approximate equation and allows representation of flow curvature.

Derivation of the approximate equations for flow about a propeller is based on consideration of the following parameters: the axial free-stream Mach number M_∞; the thickness ratio δ; the ratio of the chord ℓ to the blade-tip radius R, which is the inverse of the aspect ratio, ε; and the advance ratio λ. For true unsteady problems the reduced frequency would also enter. However, since we are examining only steady solutions, the reduced frequency need not be given further consideration. Also, for cascade solutions, a parameter representing the blockage of the flow, say solidity, would normally enter the problem; here the blades will be considered far enough apart so that variations in solidity will not be important. For an advanced turboprop, typical values of the relevant parameters are $M_\infty = 0.8$, $\delta = .02$, $\varepsilon = 0.3$, and $\lambda = 1$.

Following Cole's choices of the similarity parameters, the lateral direction y^3, which lies essentially normal to the blade, is scaled by dividing it by the value $\delta^{1/3}$. This could be done also for the radial-like or spanwise direction y^2, since the physical justification for scaling is to transform the lateral dimensions to account for the

weak diminution of disturbances in these directions in comparison to the streamwise direction. However, Isom chose to scale the spanwise direction differently by introducing ε as defined previously. This is accomplished by normalizing the streamwise direction y^1 along with the already scaled y^3 direction by ℓ, while normalizing y^2 by R. Since by these two methods of scaling, the y^i result in the same final approximation, either can be used. The latter choice is made here and the directions are scaled such that the original coordinates transform to the dimensionless ones, as given by

$$y^1 = \ell\tilde{y}^1, \qquad y^2 = R\tilde{y}^2, \qquad y^3 = \frac{\ell}{\delta^{1/3}}\,\tilde{y}^3 \tag{4.26}$$

where the tilde denotes the dimensionless coordinates. In addition, time and the disturbance potential are nondimensionalized as follows:

$$t = \frac{\tilde{t}}{\Omega}, \qquad \varphi = \delta^{2/3}\Omega R\ell\tilde{\varphi}. \tag{4.27}$$

The use of the tilde is for clarification only. When the switch to the scaled, nondimensional variables is actually performed, the tilde will be removed.

It is now assumed that in terms of the scaled variables, the following are two reasonable approximations: (1) all second derivatives of the potential are of first order in magnitude; and (2) all first derivatives are second order in magnitude. The first assumption is based on accumulated experience and the second is based on the fundamental limitation that the deviation in velocity from the free-stream velocity be small. For the limiting case of incompressible flow, the maximum variation from free-stream conditions occurs at the boundary of the solid surfaces; this can be expected to extend reasonably well to compressible flow. The perturbation velocities along a blade surface

can be considered small for sufficiently thin blades with small slopes and thus all perturbation velocities can be considered small. Then, in terms of the original unscaled variables, using Eq. (4.26) and the assumption of equal magnitude of scaled second derivatives, the following ratios among the second derivatives,

$$\frac{\partial^2\varphi}{(\partial y^1)^2} : \frac{\partial^2\varphi}{(\partial y^2)^2} : \frac{\partial^2\varphi}{(\partial y^3)^2} : \frac{\partial^2\varphi}{\partial y^1 \partial y^2} : \frac{\partial^2\varphi}{\partial y^1 \partial y^3} : \frac{\partial^2\varphi}{\partial y^2 \partial y^3}$$

and, similarly, the following ratios among the products of the first derivatives

$$\left(\frac{\partial\varphi}{\partial y^1}\right)^2 : \left(\frac{\partial\varphi}{\partial y^2}\right)^2 : \left(\frac{\partial\varphi}{\partial y^3}\right)^2 : \frac{\partial\varphi}{\partial y^1}\frac{\partial\varphi}{\partial y^2} : \frac{\partial\varphi}{\partial y^1}\frac{\partial\varphi}{\partial y^3} : \frac{\partial\varphi}{\partial y^2}\frac{\partial\varphi}{\partial y^3}$$

are each, in the given sequence, estimated to compare as

$$\frac{1}{\ell^2} : \frac{1}{R^2} : \frac{\delta^{2/3}}{\ell^2} : \frac{1}{\ell R} : \frac{\delta^{1/3}}{\ell^2} : \frac{\delta^{1/3}}{\ell R} .$$

The ratio relations above can be multiplied by ℓ^2 and written

$$1 : \varepsilon^2 : \delta^{2/3} : \varepsilon : \delta^{1/3} : \varepsilon\delta^{1/3}.$$

From the values given earlier for a typical advanced turboprop blade, ε^2, $\delta^{2/3}$, and $\varepsilon\delta^{1/3}$ are each small compared to unity. Furthermore, the values of the off-diagonal elements of the contravariant metric tensor components g^{ij} are small compared to the diagonal elements $g^{(ii)}$ for most locations, especially near the blade surfaces where gradients in the solution are largest. These are the main criteria used to reduce Eq. (4.25) to a more amenable form.

The expression $g^{ij}\,\partial\varphi/\partial x^i\,\partial\varphi/\partial x^j$, representing $(\nabla\varphi)^2$, occurs in three terms of Eq. (4.25) and is approximated as

$$g^{ij}\frac{\partial\varphi}{\partial x^i}\frac{\partial\varphi}{\partial x^j} \approx g^{11}\left(\frac{\partial\varphi}{\partial x^1}\right)^2. \qquad (4.28)$$

This is justified since each of the discarded terms is judged to be small by virtue of the corresponding ratio relations and by the fact that the off-diagonal g^{ij} are small. Of these three occurrences, only its occurrence in the last term on the left-hand side of Eq. (4.25) will be retained. This term may be written as

$$U \frac{\partial}{\partial y^1}\left[g^{11}\left(\frac{\partial \varphi}{\partial y^1}\right)^2\right] = U \frac{\partial \varphi}{\partial y^1}\left(2g^{11} \frac{\partial^2 \varphi}{(\partial y^1)^2} + \frac{\partial g^{11}}{\partial y^1}\right). \tag{4.29}$$

The variation of g^{11} with respect to y^1 is small enough that the second term on the right-hand side of Eq. (4.29) can be neglected. This results in the following approximation

$$U \frac{\partial}{\partial y^1}\left[g^{11}\left(\frac{\partial \varphi}{\partial y^1}\right)^2\right] \approx U g^{11} \frac{\partial}{\partial y^1}\left(\frac{\partial \varphi}{\partial y^1}\right)^2 . \tag{4.30}$$

The Laplacian operator occurring in the final brackets on the right-hand side of Eq. (4.25) remains to be simplified. This is done by neglecting the last set of terms which contain the first derivatives of the potential. The Laplacian factor is thus given the approximate form

$$g^{ij} \frac{\partial^2 \varphi}{\partial y^i \partial y^j} + \frac{1}{\sqrt{g}} \frac{\partial}{\partial y^i}\left(\sqrt{g}\, g^{ij}\right) \frac{\partial \varphi}{\partial y^j} \approx g^{ij} \frac{\partial^2 \varphi}{\partial y^i \partial y^j} . \tag{4.31}$$

Equations (4.30) and (4.31) are inserted into Eq. (4.25) and the fourth term containing a first derivative of the potential on the left-hand side of the equation is omitted. This reduces Eq. (4.25) to

$$\begin{aligned} &\frac{\partial^2 \varphi}{\partial t^2} + U^2 \frac{\partial^2 \varphi}{(\partial y^1)^2} + 2U \frac{\partial^2 \varphi}{\partial y^1 \partial t} + U g^{11} \frac{\partial}{\partial y^1}\left(\frac{\partial \varphi}{\partial y^1}\right)^2 \\ &= \left[c_\infty^2 - (k-1)\left(\frac{\partial \varphi}{\partial t} + U \frac{\partial \varphi}{\partial y^1}\right)\right]\left[g^{11} \frac{\partial^2 \varphi}{(\partial y^1)^2} + g^{22} \frac{\partial^2 \varphi}{(\partial y^2)^2} + g^{33} \frac{\partial^2 \varphi}{(\partial y^3)^2}\right. \\ &\left. + 2\left(g^{12} \frac{\partial^2 \varphi}{\partial y^1 \partial y^2} + g^{13} \frac{\partial^2 \varphi}{\partial y^1 \partial y^3} + g^{23} \frac{\partial^2 \varphi}{\partial y^2 \partial y^3}\right)\right]. \end{aligned} \tag{4.32}$$

C 2

Finally, on the right-hand side, the unsteady term is dropped and only the largest of the nonlinear terms is retained which contains the factor $g^{ij}\,\partial^2\varphi/\partial y^i \partial y^j$ from the Laplacian. All other nonlinear terms are small based on the equivalence of the ratio relations. The equation for the perturbation potential is then

$$\frac{\partial^2\varphi}{\partial t^2} + U^2\,\frac{\partial^2\varphi}{(\partial y^1)^2} + 2U\,\frac{\partial^2\varphi}{\partial y^1 \partial t} + 2Ug^{11}\,\frac{\partial\varphi}{\partial y^1}\,\frac{\partial^2\varphi}{(\partial y^1)^2}$$

$$= -(k-1)Ug^{11}\,\frac{\partial\varphi}{\partial y^1}\,\frac{\partial^2\varphi}{(\partial y^1)^2} + c_\infty^2\left[g^{11}\,\frac{\partial^2\varphi}{(\partial y^1)^2} + g^{22}\,\frac{\partial^2\varphi}{(\partial y^2)^2} + g^{33}\,\frac{\partial^2\varphi}{(\partial y^3)^2}\right.$$

$$\left. + 2\left(g^{12}\,\frac{\partial^2\varphi}{\partial y^1 \partial y^2} + g^{13}\,\frac{\partial^2\varphi}{\partial y^1 \partial y^3} + g^{23}\,\frac{\partial^2\varphi}{\partial y^2 \partial y^3}\right)\right]. \qquad (4.33)$$

By defining

$$M = \frac{U}{c_\infty} \qquad (4.34)$$

and combining similar terms yields, after dividing by c_∞^2,

$$\frac{1}{c_\infty^2}\,\frac{\partial^2\varphi}{\partial t^2} + (M^2 - g^{11})\,\frac{\partial^2\varphi}{(\partial y^1)^2} + 2\,\frac{M}{c_\infty}\,\frac{\partial^2\varphi}{\partial y^1 \partial t} + (k+1)\,\frac{M}{c_\infty}\,g^{11}\,\frac{\partial\varphi}{\partial y^1}\,\frac{\partial^2\varphi}{(\partial y^1)^2}$$

$$= g^{22}\,\frac{\partial^2\varphi}{(\partial y^2)^2} + g^{33}\,\frac{\partial^2\varphi}{(\partial y^3)^2} + 2\left(g^{12}\,\frac{\partial^2\varphi}{\partial y^1 \partial y^2}\right.$$

$$\left. + g^{13}\,\frac{\partial^2\varphi}{\partial y^1 \partial y^3} + g^{23}\,\frac{\partial^2\varphi}{\partial y^2 \partial y^3}\right). \qquad (4.35)$$

This is the final form of the perturbation potential equation in unscaled variables. This equation will now be transformed by the scaling relations given in Eqs. (4.26) and (4.27). Substitution of these scaling relations into Eq. (4.35) gives

$$\frac{\Omega^2}{c_\infty^2}\frac{\partial^2\varphi}{\partial t^2} + 2M\frac{\Omega}{\ell c_\infty}\frac{\partial^2\varphi}{\partial y^1 \partial t} + (M^2 - g^{11})\frac{1}{\ell^2}\frac{\partial^2\varphi}{(\partial y^1)^2}$$

$$+ (k+1)Mg^{11}\frac{\delta^{2/3}\Omega R}{\ell^2 c_\infty}\frac{\partial\varphi}{\partial y^1}\frac{\partial^2\varphi}{(\partial y^1)^2} = g^{22}\frac{1}{R^2}\frac{\partial^2\varphi}{(\partial y^2)^2} + g^{33}\frac{\delta^{2/3}}{\ell^2}\frac{\partial^2\varphi}{(\partial y^3)^2}$$

$$+ 2\left(\frac{g^{12}}{\ell R}\frac{\partial^2\varphi}{\partial y^1 \partial y^2} + \frac{\delta^{1/3}g^{13}}{\ell^2}\frac{\partial^2\varphi}{\partial y^1 \partial y^3} + \frac{\delta^{1/3}g^{23}}{\ell R}\frac{\partial^2\varphi}{\partial y^2 \partial y^3}\right) \qquad (4.36)$$

where the tilde is not shown. Multiplying this equation by $\ell^2/\delta^{2/3}$ and introducing a constant Mach number, characteristic of the rotational speed of the propeller tip as defined by

$$M_T = \frac{\Omega R}{c_\infty}\,, \qquad (4.37)$$

results in

$$\left(\frac{M_T\varepsilon}{\delta^{1/3}}\right)^2\frac{\partial^2\varphi}{\partial t^2} + \frac{2MM_T\varepsilon}{\delta^{2/3}}\frac{\partial^2\varphi}{\partial y^1 \partial t} + \frac{M^2 - g^{11}}{\delta^{2/3}}\frac{\partial^2\varphi}{(\partial y^1)^2} + (k+1)MM_T g^{11}\frac{\partial\varphi}{\partial y^1}\frac{\partial^2\varphi}{(\partial y^1)^2}$$

$$= g^{22}\frac{\varepsilon^2}{\delta^{2/3}}\frac{\partial^2\varphi}{(\partial y^2)^2} + g^{33}\frac{\partial^2\varphi}{(\partial y^3)^2} + 2\left(g^{12}\frac{\varepsilon}{\delta^{2/3}}\frac{\partial^2\varphi}{\partial y^1 \partial y^2}\right.$$

$$\left. + g^{13}\frac{1}{\delta^{1/3}}\frac{\partial^2\varphi}{\partial y^1 \partial y^3} + g^{23}\frac{\varepsilon}{\delta^{1/3}}\frac{\partial^2\varphi}{\partial y^2 \partial y^3}\right). \qquad (4.38)$$

For low frequency or steady problems, it is admissible to delete the second derivative with respect to time. This leaves the final form of the governing equation in terms of the scaled variables as

$$\frac{2MM_T\varepsilon}{\delta^{2/3}}\frac{\partial^2\varphi}{\partial y^1\partial t}+\frac{M^2-g^{11}}{\delta^{2/3}}\frac{\partial^2\varphi}{\left(\partial y^1\right)^2}+(k+1)MM_Tg^{11}\frac{\partial\varphi}{\partial y^1}\frac{\partial^2\varphi}{\left(\partial y^1\right)^2}=$$

$$g^{22}\frac{\varepsilon^2}{\delta^{2/3}}\frac{\partial^2\varphi}{\left(\partial y^2\right)^2}+g^{33}\frac{\partial^2\varphi}{\left(\partial y^3\right)^2}+2\left(g^{12}\frac{\varepsilon}{\delta^{2/3}}\frac{\partial^2\varphi}{\partial y^1\partial y^2}+g^{13}\frac{1}{\delta^{1/3}}\frac{\partial^2\varphi}{\partial y^1\partial y^3}\right.$$

$$\left.+g^{23}\frac{\varepsilon}{\delta^{1/3}}\frac{\partial^2\varphi}{\partial y^2\partial y^3}\right). \qquad (4.39)$$

Equation (4.39) is the small disturbance equation which is solved numerically by the ADI Douglas-Gunn algorithm presented in Chapter VII.

V. BOUNDARY CONDITIONS

5.1 Wall Tangency Condition for Blade Surfaces

The small disturbance boundary condition to be applied at the blade surfaces will now be established. This necessitates returning briefly to the unscaled variables.

In a blade-fixed coordinate system, if the equation for the surface of a blade moving in a time dependent manner is given by

$$F(y^1, y^2, y^3, t) = 0, \tag{5.1}$$

then the vanishing of the fluid velocity component normal to the surface brings

$$\frac{D}{Dt} F(y^1, y^2, y^3, t) = \frac{\partial F}{\partial t} + (\bar{a} + \nabla\varphi) \cdot \nabla F = 0 \tag{5.2}$$

where

$$F = F_u(y^1, y^2, y^3, t) = y^3 - h_u(y^1, y^2, t) = 0 \tag{5.3a}$$

on the upper (suction) blade surface from the leading edge (L.E.) to the trailing edge (T.E.), and

$$F = F_o(y^1, y^2, y^3, t) = y^3 - h_o(y^1, y^2, t) = 0 \tag{5.3b}$$

on the lower (pressure) blade surface. Here, h is the profile parameter. This follows the convention used for wing surfaces. The coordinates are aligned as shown in Fig. 5.1, where y^1 is nearly along the mean chord, y^3 is nearly normal to the chord, and y^2 lies in the spanwise direction.

The general time-dependent boundary condition which allows the profile parameter to include pitching, bending, and twisting is

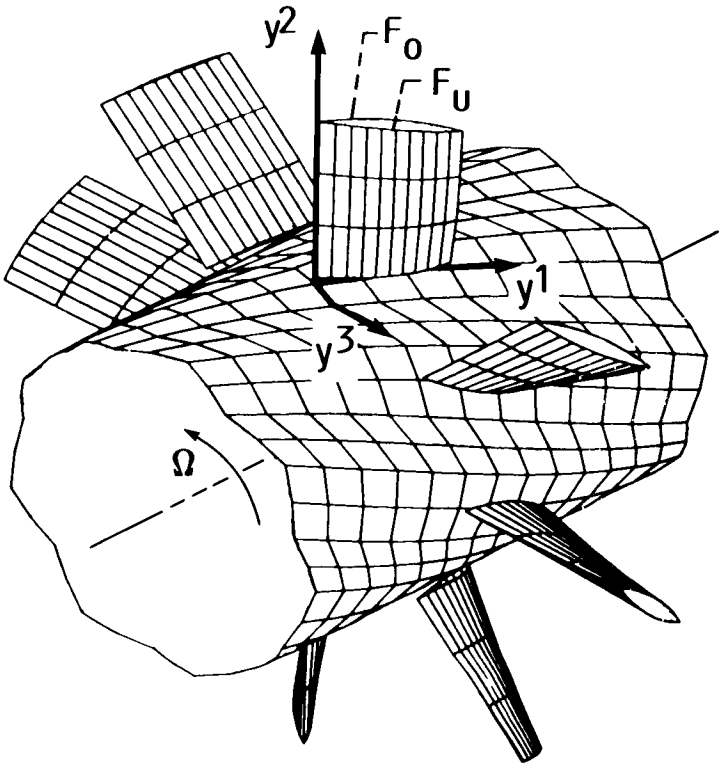

FIGURE 5.1. - ARRANGEMENT OF HELICAL COORDINATES WITH RESPECT TO PROPELLER CASCADE.

developed next. This time-dependence is included mainly for any future efforts which consider flutter. Proceeding with this general development, the two spatial terms in Eq. (5.2) are

$$\bar{a} \cdot \nabla F = U \frac{\partial F}{\partial y^1} \tag{5.4}$$

and

$$\nabla\varphi \cdot \nabla F = g^{ij} \frac{\partial \varphi}{\partial y^i} \frac{\partial F}{\partial y^j} \quad . \tag{5.5}$$

The latter expression can be written out using Eq. (5.3) as

$$\begin{aligned} \nabla\varphi \cdot \nabla F = -g^{11} \frac{\partial \varphi}{\partial y^1} \frac{\partial h}{\partial y^1} - g^{22} \frac{\partial \varphi}{\partial y^2} \frac{\partial h}{\partial y^2} + g^{33} \frac{\partial \varphi}{\partial y^3} \\ - g^{12} \left(\frac{\partial \varphi}{\partial y^1} \frac{\partial h}{\partial y^2} + \frac{\partial \varphi}{\partial y^2} \frac{\partial h}{\partial y^1} \right) + g^{13} \left(\frac{\partial \varphi}{\partial y^1} - \frac{\partial \varphi}{\partial y^3} \frac{\partial h}{\partial y^1} \right) \\ + g^{23} \left(\frac{\partial \varphi}{\partial y^2} - \frac{\partial \varphi}{\partial y^3} \frac{\partial h}{\partial y^2} \right) . \end{aligned} \tag{5.6}$$

The usual application of small disturbance boundary conditions requires that an approximation be made to the derivative of the potential in the direction normal to the mean chord. The use of Eq. (5.6) along with Eq. (5.4), when substituted into Eq. (5.2), with rearrangement to separate $\partial\varphi/\partial y^3$, gives

$$\begin{aligned} \frac{\partial \varphi}{\partial y^3} \left(g^{33} - g^{13} \frac{\partial h}{\partial y^1} - g^{23} \frac{\partial h}{\partial y^2} \right) = \frac{\partial h}{\partial t} + U \frac{\partial h}{\partial y^1} + g^{11} \frac{\partial \varphi}{\partial y^1} \frac{\partial h}{\partial y^1} + g^{22} \frac{\partial \varphi}{\partial y^2} \frac{\partial h}{\partial y^2} \\ + g^{12} \left(\frac{\partial \varphi}{\partial y^1} \frac{\partial h}{\partial y^2} + \frac{\partial \varphi}{\partial y^2} \frac{\partial h}{\partial y^1} \right) - g^{13} \frac{\partial \varphi}{\partial y^1} - g^{23} \frac{\partial \varphi}{\partial y^2} . \end{aligned} \tag{5.7}$$

Introduction of the scaling laws into the above equation provides a basis for simplification. The scaling of h that is consistent with the scaling relations introduced previously is

$$h = \ell\delta\tilde{h}(\tilde{y}^1, \tilde{y}^2, \tilde{t}). \tag{5.8}$$

Substituting Eq. (5.8) along with the previous scaling relations into Eq. (5.7) and again discarding the tilde, yields

$$\left(g^{33} - g^{13}\,\delta\,\frac{\partial h}{\partial y^1} - g^{23}\varepsilon\delta\,\frac{\partial h}{\partial y^2}\right)\frac{\partial \varphi}{\partial y^3} = \varepsilon\,\frac{\partial h}{\partial t} + \frac{U}{\Omega R}\,\frac{\partial h}{\partial y^1} + g^{11}\delta^{2/3}\,\frac{\partial \varphi}{\partial y^1}\,\frac{\partial h}{\partial y^1}$$

$$+ g^{22}\delta^{2/3}\varepsilon^2\,\frac{\partial \varphi}{\partial y^2}\,\frac{\partial h}{\partial y^2} + g^{12}\delta^{2/3}\,\varepsilon\left(\frac{\partial \varphi}{\partial y^1}\,\frac{\partial h}{\partial y^2} - \frac{\partial \varphi}{\partial y^2}\,\frac{\partial h}{\partial y^1}\right)$$

$$- g^{13}\,\frac{1}{\delta^{1/3}}\,\frac{\partial \varphi}{\partial y^1} - g^{23}\,\frac{\varepsilon}{\delta^{1/3}}\,\frac{\partial \varphi}{\partial y^2}\,. \tag{5.9}$$

Based on the typical values of ε and δ, this is closely approximated by

$$\frac{\partial \varphi}{\partial y^3} = \frac{1}{g^{33}}\left(\varepsilon\,\frac{\partial h}{\partial t} + \frac{M}{M_T}\,\frac{\partial h}{\partial y^1} - g^{13}\,\frac{1}{\delta^{1/3}}\,\frac{\partial \varphi}{\partial y^1} - g^{23}\,\frac{\varepsilon}{\delta^{1/3}}\,\frac{\partial \varphi}{\partial y^2}\right). \tag{5.10}$$

For blades which taper gradually toward the tip, the last term in Eq. (5.10) can be neglected with the result

$$\frac{\partial \varphi}{\partial y^3} = \frac{1}{g^{33}}\left(\varepsilon\,\frac{\partial h}{\partial t} + \frac{M}{M_T}\,\frac{\partial h}{\partial y^1} - g^{13}\,\frac{1}{\delta^{1/3}}\,\frac{\partial \varphi}{\partial y^1}\right). \tag{5.11}$$

One of the key developments of this work is the generation of coordinate systems possessing the characteristic that $g^{13} \approx 0$ at the blade surfaces. For these coordinate systems, the unsteady boundary condition at the blade surface, in scaled variables, is

$$\frac{\partial \varphi}{\partial y^3} \approx \frac{1}{g^{33}}\left(\varepsilon\,\frac{\partial h}{\partial t} + \frac{M}{M_T}\,\frac{\partial h}{\partial y^1}\right). \tag{5.12}$$

It is interesting to note that in dimensional Cartestian coordinates ($y^1 = x$, $y^2 = y$, $y^3 = z$), this expression is the familiar

$$\frac{\partial \varphi}{\partial z} \approx \frac{\partial h}{\partial t} + U\,\frac{\partial h}{\partial x}\,. \tag{5.13}$$

Finally, the steady scaled boundary condition is simply

$$\frac{\partial \varphi}{\partial y^3} \approx \frac{1}{g^{33}}\,\frac{M}{M_T}\,\frac{\partial h}{\partial y^1}\,. \tag{5.14}$$

This boundary condition is not actually applied at the airfoil surfaces but rather at two surfaces separated slightly such that they straddle the mean chord surface which itself lies on, or near, the $y^3 = 0$ surface. Thus, at the upper surface

$$\left.\frac{\partial \varphi}{\partial y^3}\right|_{y^3=0+} \approx \frac{1}{g^{33}} \frac{M}{M_T} \frac{\partial h_u}{\partial y^1} . \tag{5.15a}$$

and, at the lower surface

$$\left.\frac{\partial \varphi}{\partial y^3}\right|_{y^3=0-} \approx \frac{1}{g^{33}} \frac{M}{M_T} \frac{\partial h_o}{\partial y^1} . \tag{5.15b}$$

5.2 Flow Field Boundary Conditions

Additional boundary conditions must be specified to fully define the problem. These include the boundary conditions upstream and downstream of the propeller, along with those for the inner and outer radial surfaces, and those far above and below the blade. Additionally, the Kutta condition at the trailing edge of the blade is required along with a treatment for the trailing vortex sheet. The handling of a cascade of blades is identical to that of an isolated blade aside from the specification of the conditions above and below the blade. Even in the case of cascade flow, the flow region about a single blade is sufficient provided the application of periodic conditions reduces the extent of the problem. As mentioned previously, shocks require no special boundary treatment as internal discontinuities because they are captured numerically as part of the solution process.

The upstream boundary condtion on the perturbation potential is

$$\varphi = 0. \tag{5.16}$$

This merely states that the free-stream condition prevails sufficiently far upstream.

In the downstream direction, the value of the perturbation potential is unknown, but at a large enough distance downstream

$$\frac{\partial \varphi}{\partial y^1} = 0 \tag{5.17}$$

is used as the boundary condition.

At the hub, or inner spanwise boundary, the condition

$$\frac{\partial \varphi}{\partial y^2} = 0 \tag{5.18}$$

is used, and the outer spanwise boundary condition is simply

$$\varphi = 0. \tag{5.19}$$

Although y^2 is not strictly a radial direction, it closely approximates it for the coordinate systems employed here.

The far field above and below the blade has two boundary condition options. For an isolated blade, the condition

$$\frac{\partial \varphi}{\partial y^3} = 0 \tag{5.20}$$

is assumed to apply both far above and far below the blade. This requires a coordinate system whereby the y^3 direction is normal to the free-stream direction y^1 at these boundaries. For multiple blades, cascade-type periodic boundary conditions are applied such that

$$\varphi(y^1, y^2, t)\Big|_{y^3 = \substack{\text{upper} \\ \text{surface}}} = \varphi(y^1, y^2, t)\Big|_{y^3 = \substack{\text{lower} \\ \text{surface}}} \tag{5.21}$$

is satisfied over the boundary surfaces which are chosen to lie at the midchannel. This, in return for straightforward application, requires a coordinate system which provides nodal coordinates having azimuthal

periodicity. Such periodic coordinate systems are discussed in a subsequent chapter. Only solutions using the cascade boundary conditions are presented in this work.

It remains to discuss the boundary conditions in the vortex wake. Rollup of a wake is ignored and, the resulting vortex sheet is approximated as lying between the downstream extensions of the helical surfaces upon which the blade boundary conditions are imposed. The strength of the vortex sheet is assumed to be preserved as it convects downstream. In addition, the direction of the vortex vector is assumed to be "parallel" to the free-stream direction. Since the vortex sheet is a free surface, it cannot support a pressure difference. Along with these statements and the fact that the normal velocity across the sheet is zero, it follows that the tangential velocity jump occurring across the sheet is entirely in the spanwise direction. The boundary condition at the trailing edge can be written in terms of the scaled coordinates as

$$[\varphi]_{T.E.} = \Gamma(y^2, t) \tag{5.22}$$

where Γ is the circulation around the propeller blade, and

$$[\varphi] = \left(\varphi\right)_{y^3=0+} - \left(\varphi\right)_{y^3=0-} \tag{5.23}$$

is the jump in the perturbation potential across the wake.

VI. HELICAL COORDINATES

This chapter contains the development of special periodic helical coordinates suitable for propeller problems which include cascade effects. The coordinate transformation between this system and an orthogonal Cartesian system is specified so as to provide simple periodic boundaries, and to also provide orthogonal properties at the blades. However, before describing these new helical coordinates, a brief discussion will be given for a simpler helical coordinate system satisfactory for flow about an isolated blade, but not for cascade flow. This discussion points out similarities and distinctions between the two coordinate systems and will help to illustrate the features of the new coordinates.

6.1 Helical Coordinates for an Isolated Blade

Simple helical coordinates are useful in calculating the flow about isolated propeller blades. The transformation of these coordinates along with a listing of their metric tensors is given in Appendix B. These simple helical coordinates consist of two sets of helices, providing two coordinate directions, y^1 and y^3, with the remaining coordinate direction y^2 being essentially radial. A set of these coordinates is shown in Fig. 6.1. The helical curves are confined to spiral about a common axis on circular cylindrical surfaces; members of each set spiral clockwise about the axis when viewed along the axis in the direction corresponding to an increasing value of y^1. The axial

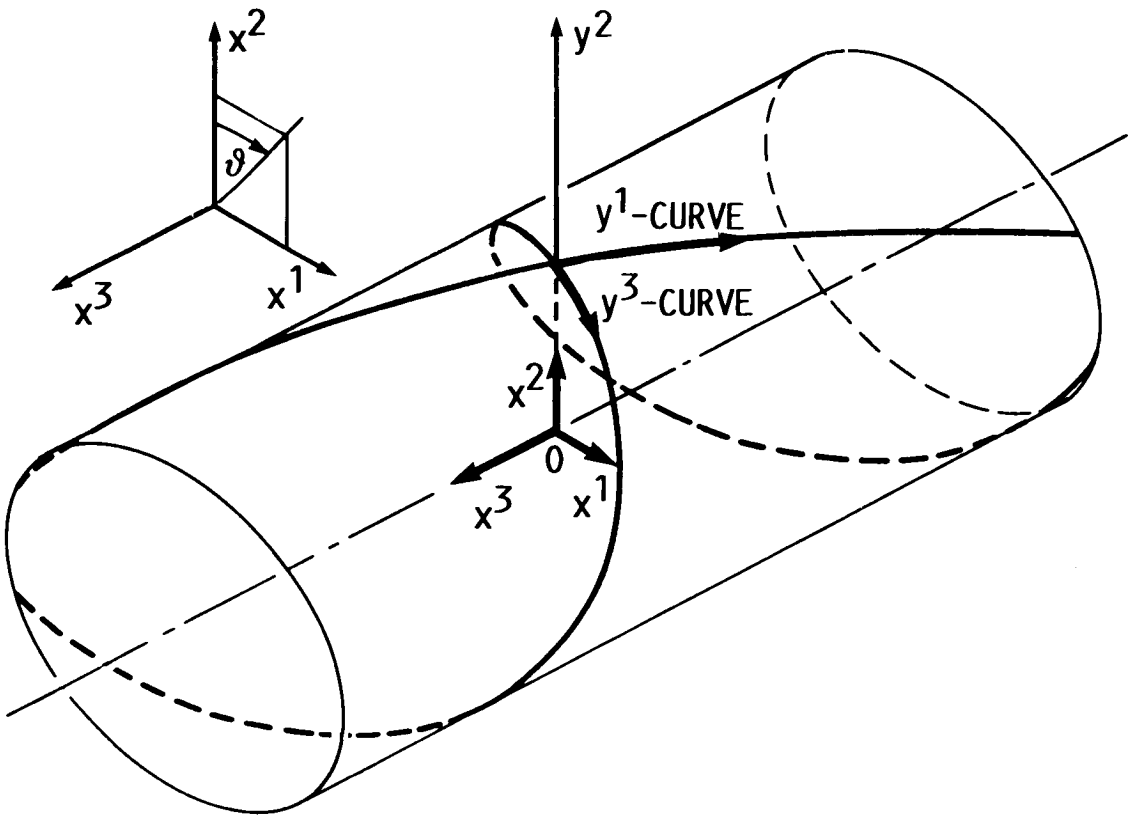

FIGURE 6.1. - HELICAL COORDINATES USED FOR ISOLATED BLADE SHOWN WITH CARTESIAN COORDINATES.

components of y^1 and y^3 are oppositely directed. The two sets of helices are mutually orthogonal.

The main advantage of these coordinates is that the undisturbed flow direction can be aligned with one set of helices. These streamwise helices are constructed such that the helices of greater radii have smaller advance ratios; i.e., the smaller the radius the steeper the spiral, exactly characterizing the mean propeller flow. The set of helices normal to the streamwise helices behaves in the reverse way.

Another distinct advantage is the orthogonality between the two sets of helices. This is an important feature because the small disturbance boundary condition applied at the blade surfaces is greatly simplified. Orthogonality is a desirable property because it generally results in more accurate numerical calculations. Thus, it is advantageous to have these coordinates orthogonal throughout the region of interest.

The coordinate direction y^2, which serves to measure the radial value is, in general, not a straight line. In fact, this coordinate direction has only one straight coordinate line: its coordinate axis, which was chosen to align with the leading edge of the blade. This is called the pitch change axis. With increasing distance from the pitch change axis, this coordinate direction departs to an increasing extent from a purely radial direction. Hence, the orthogonality of the coordinate system is reduced as the distance from the blade's leading edge is increased. Only at the leading edge is the coordinate system truly orthogonal. A notable charcteristic of the coordinate system is that, for high advance ratios, it tends toward an orthogonal Cartesian coordinate system. This can easily be seen by inspecting the metric

tensor for this transformation which is provided in Appendix B. Since for all space $g_{11} = 1$ and $g_{33} = 1$, the values of y^1 and y^3 for any given point correspond to the respective arc lengths along these curves from the origin to that point. This is not the case for the y^2 curves. As mentioned above, the y^2 coordinate is a measure of the radial value from the axis to a given point; the arc length along y^2 exceeds this value. However, as the advance ratio increases, g_{22} also tends to unity.

6.2 Periodic Helical Coordinate System for Cascades

The periodic helical coordinates are closely related to the helical coordinates described above. The streamwise helices y^1 are unaltered so as to retain their alignment with the undisturbed flow. However, to provide periodicity, the geometrical scaling of the y^3 direction is modified so that this coordinate is no longer a direct measure of its arc length. Rather, the y^3 direction is specified to scale similar to the angular coordinate of the familiar circular cylindrical coordinate system; i.e., a change in the value of the y^3 coordinate brings a change in arc length which is proportional to the radius. However, this change in scaling the y^3 coordinate is not sufficient to give circumferential periodicity. The y^3 coordinate curves must be changed so that they are no longer helices.

To provide circumferential periodicty, the y^3 coordinate must be constructed such that, in a periodic fashion, it repeats its axial locations. The simplest choice is to make y^3 the circumferential direction, forcing it to be independent of the axial value. The drawback in doing this is that then it would no longer be normal to the streamwise direction. Orthogonality in these two directions is an

important quality, especially near the surfaces of the blades. To provide orthogonality at the mean blade locations, the y^3 direction must assume the direction of the y^3 coordinate of the helical system used for an isolated blade, at least near the blades. Away from the blades, the y^3 coordinate should reverse its axial direction so as to bend back and regain its original axial station. This must be repeated in a periodic fashion to conform to the locations of the blades. Thus, only coordinate curves in the streamwise direction y^1 are helices for this system. The y^2 direction remains a coordinate which measures the radial value and since it is formed by the intersection of surfaces of constant y^1 and y^3, it will generally not be a straight line.

A set of helical coordinates which has these properties is given by the following transformation to the Cartesian coordinates x^i.

$$x^1 = y^2 \sin \vartheta \tag{6.1}$$

$$x^2 = y^2 \cos \vartheta \tag{6.2}$$

$$x^3 = -\frac{V}{U} y^1 + A(y^2)B(y^3) \tag{6.3}$$

where ϑ is the circumferential angle measured as shown in Fig. 6.2, and which is related to the helical coordinates by

$$\vartheta = \frac{\Omega}{U} y^1 + \frac{y^3}{R} . \tag{6.4}$$

The total helical velocity U is, of course, a function of the radius.

It is convenient to make the following assignments which are consistent with the notation in Appendix A: $x^1 = x$, $x^2 = y$, $x^3 = z$ for the Cartesian coordinates and $y^1 = \gamma$, $y^2 = r$, $y^3 = \xi$ for the helical coordinates. Using these replacements the next section will discuss the proper choices for $A(r)$ and $B(\xi)$.

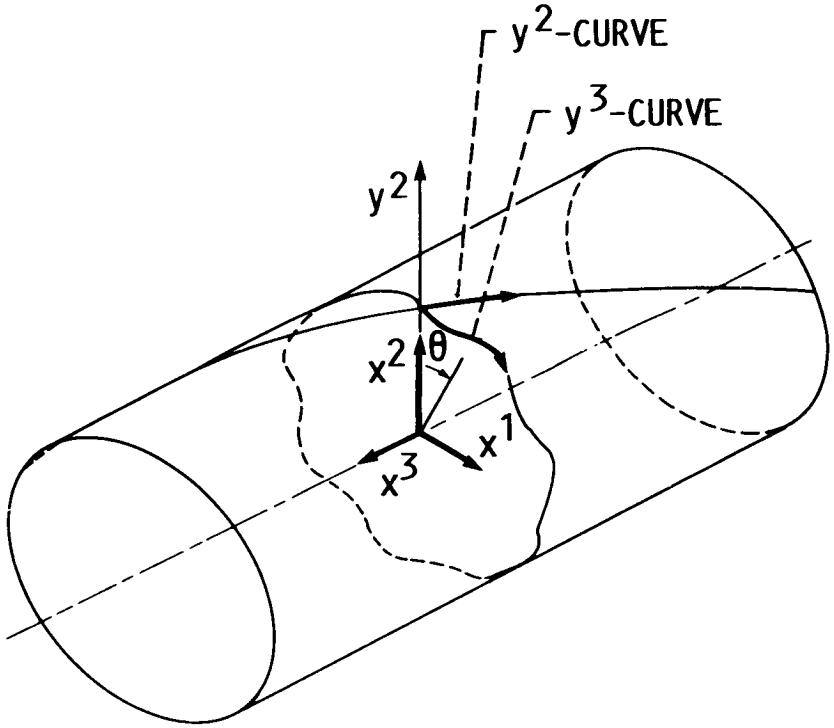

FIGURE 6.2. - PERIODICAL HELICAL COORDINATES FOR A CASCADE SHOWN WITH CARTESIAN COORDINATES.

6.3 Tailoring the Periodic Helical Coordinates

The functions $A(r)$ and $B(\xi)$ are used to tailor the helical coordinate system to two sets of the streamwise helical sheets. The two sets of sheets of constant ξ are illustrated in Fig. 6.3. They are evenly spaced in the circumferential direction. The first set of these sheets will contain the mean position of uncambered, symmetric, twisted blades. These correspond to the advance helicoids described earlier in Chapter II. The second set of helical surfaces is similar and is chosen such that each sheet lies midway between two neighbors of the first set, thus forming an alternating arrangement of periodically spaced helicoidal surfaces. The boundary conditions for the airfoil surfaces are applied very near members of the first set, whereas, the periodic conditions are enforced on the second. It should be mentioned that for asymmetrical blades or blades with camber, the mean blade position will not quite coincide with a helical sheet. The mean blade positions are assumed to lie near the first set of helical sheets so that small disturbance boundary conditions can be accurately applied.

As mentioned, the helical sheets are surfaces of constant ξ. It is desirable for satisfactory application of blade surface boundary conditions that the ξ-coordinate be orthogonal to the mean blade surface. In addition, simple handling of periodicity requires that there be no net change in axial distance when traversing a ξ-coordinate line from one periodic boundary to another. These two objectives can be met by properly choosing the functions $A(r)$ and $B(\xi)$.

Recall that the functions $A(r)$ and $B(\xi)$ enter the transformation through the relationship given in Eq. (6.3), which is now written as

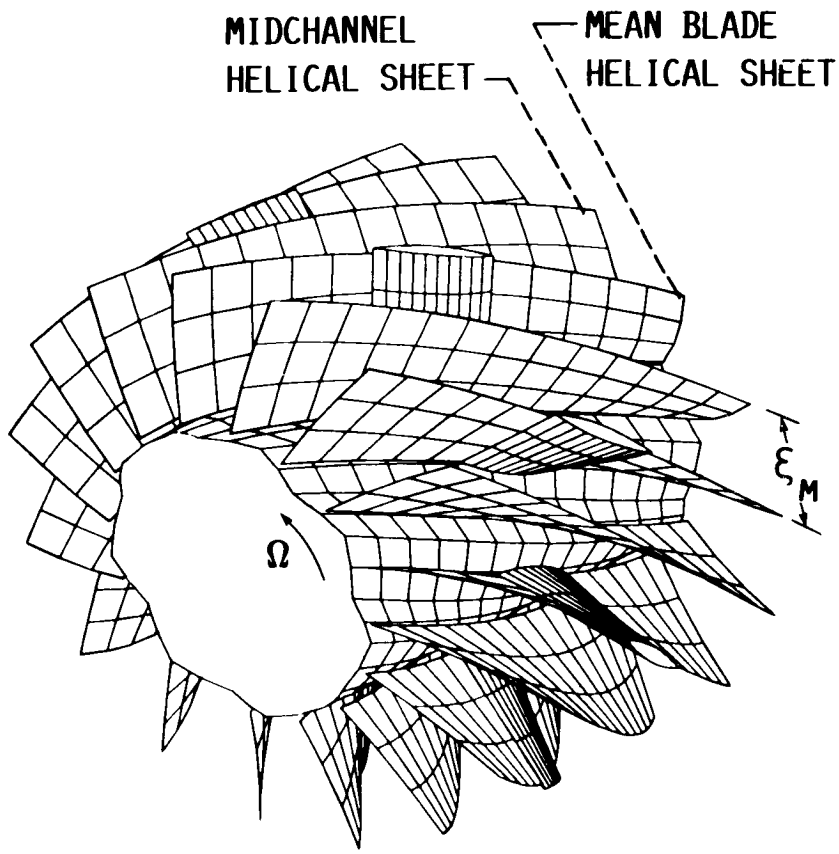

FIGURE 6.3. - ALTERNATING ARRANGEMENT OF HELICOIDAL SHEETS FOR AN EIGHT-BLADED PROPELLER.

$$z = -\gamma \frac{V}{U} + A(r)B(\xi). \tag{6.5}$$

This specifies the axial coordinate in terms of the helical variables. It will be shown that by choosing suitable forms for $A(r)$ and $B(\xi)$, two of the metric tensor components g_{13} and g_{23} vanish concurrently at special values of ξ. The γ and ξ curves will be orthogonal where $g_{13} = 0$ and, likewise, the r and ξ curves will be orthogonal where $g_{23} = 0$. When both are zero, the ξ curves will be normal to the surfaces of constant ξ. The first objective is to arrange this to occur for those helical sheets containing the mean positions of the propeller blades. To assure that these surfaces are periodically spaced in the circumferential direction, $B(\xi)$ is expressed as the product of two functions of ξ in the form

$$B(\xi) = E(\xi) \frac{\xi_m}{\pi} \sin\left(\frac{\xi}{\xi_m} \pi\right) \tag{6.6}$$

where E is a damping function and ξ_m is a positive constant establishing the period and is exactly half the distance between the blades.

Meeting the conditions of orthogonality requires the inspection of the functional dependence of g_{13} and g_{23}. This will reveal what the final forms of $A(r)$ and $B(\xi)$ must be. First, the metric tensor component g_{13} will be discussed, and then g_{23} where additional constraints will be imposed on the axial velocity $V(r)$.

From Appendix A Eq. (A28), we have

$$g_{13} = \frac{\Omega r}{U} \frac{r}{R} - \frac{V}{U} A(r)B'(\xi) \tag{6.7}$$

where the prime indicates differentiation with respect to the indicated argument. By using Eq. (6.6), this becomes

$$g_{13} = \frac{\Omega r}{U}\frac{r}{R} - \frac{V}{U}A(r)\left[E'(\xi)\frac{\xi_m}{\pi}\sin\left(\frac{\xi}{\xi_m}\pi\right) + E(\xi)\cos\left(\frac{\xi}{\xi_m}\pi\right)\right]. \qquad (6.8)$$

As mentioned, $E(\xi)$ is a damping function and is needed to assure a valid coordinate transformation. Useful selections of $E(\xi)$ include $E = \exp\left(-a_o\frac{|\bar{\xi}|}{\xi_m}\right)$, and $E = \exp\left(-a_o\frac{\bar{\xi}^2}{\xi_m^2}\right)$ as well as polynomial forms. The significance of the bar above ξ in the exponential arguments will be discussed later. For simplicity only the first case, namely $E(\xi) = \exp\left(-a_o\frac{|\bar{\xi}|}{\xi_m}\right)$, will be presented since the other cases follow similarly.

The derivative $E'(\xi)$ is

$$E'(\xi) = \pm\frac{a_o}{\xi_m}\exp\left(-a_o\frac{|\bar{\xi}|}{\xi_m}\right) \qquad (6.9)$$

where the minus (plus) sign relates to positive (negative) values of ξ.

By substituting the expressions for $E(\xi)$ and $E'(\xi)$ into Eq. (6.8), we obtain

$$g_{13} = \frac{\Omega r}{U}\frac{r}{R} - \frac{V}{U}A(r)\exp\left(-a_o\frac{|\bar{\xi}|}{\xi_m}\right)\left[\cos\left(\frac{\xi}{\xi_m}\pi\right) \pm \frac{a_o}{\pi}\sin\left(\frac{\xi}{\xi_m}\pi\right)\right] \qquad (6.10)$$

with the same meaning as above attached to the sign notation appearing before the last term.

The periodic significance of ξ_m is now determined by introducing a positive integer N_B and allowing the value of ξ/ξ_m to range from $-1/2N_B$ to $1/2N_B$. Here, N_B signifies the number of blades in the cascade and may be either even or odd. Since the value ξ_m is half the distance between neighboring blades, the blades will be located at intervals of twice ξ_m. The total distance from $-1/2N_B$ to $1/2N_B$ equals one traverse around the cascade. By arbitrarily specifying

one blade to be positioned at $\xi = 0$, the blade locations take on the following values of ξ/ξ_m.

$$\frac{\xi_B}{\xi_m} = \begin{cases} 0, \pm 2, \pm 4, \ldots, \pm(N_B - 1); & \text{for } N_B \text{ odd} \\ 0, \pm 2, \pm 4, \ldots, \pm(N_B - 2), N_B; & \text{for } N_B \text{ even} \end{cases} \tag{6.11}$$

where the subscript B denotes a blade location. Also, at this point, the meaning of the over-bar above ξ is made clear by defining $\bar{\xi}$ to be the value of ξ as measured from the nearest blade. Thus the extremes of $\bar{\xi}$ will be $\pm\xi_m$. With these definitions Eq. (6.10) for the metric tensor component can be written

$$g_{13}\Big|_{\xi=\xi_B} = \frac{\Omega r}{U}\frac{r}{R} - \frac{V}{U} A(r) \exp\left(-a_o \frac{|\bar{\xi}_B|}{\xi_m}\right)\left[\cos\left(\frac{\xi_B}{\xi_m}\pi\right) \pm \frac{a_o}{\pi}\sin\left(\frac{\xi_B}{\xi_m}\pi\right)\right] \tag{6.12}$$

for values at the blade stations. However, since $\bar{\xi}_B = 0$ from the definition of $\bar{\xi}$ and since $\cos\left(\frac{\xi_B}{\xi_m}\pi\right) = 1$ and $\sin\left(\frac{\xi_B}{\xi_m}\pi\right) = 0$, the value of the component g_{13} at the N_B blade stations reduces to

$$g_{13}\Big|_{\xi=\xi_B} = \frac{\Omega r}{U}\frac{r}{R} - \frac{V}{U} A(r). \tag{6.13}$$

Therefore, g_{13} can be forced to equal zero at these periodic positions by simply prescribing that

$$A(r) = \frac{\Omega R}{V}\left(\frac{r}{R}\right)^2. \tag{6.14}$$

The expression for the axial coordinate in Eq. (6.5) can now be explicitly written as

$$z = -\gamma\frac{V}{U} + \frac{\xi_m}{\pi}\frac{\Omega R}{V}\frac{r^2}{R^2}\exp\left(-a_o\frac{|\bar{\xi}|}{\xi_m}\right)\sin\left(\frac{\xi}{\xi_m}\pi\right). \tag{6.15}$$

As mentioned above, the exponential factor serves as a damping function to guarantee that the coordinate transformation is well behaved; i.e.,

the coordinates should not fold nor should the Jacobian of the transformation vanish anywhere within the region of interest. In this regard, the quantity a_o is a nonnegative constant which increases in magnitude as the ratio $V/\Omega R \equiv \lambda$ decreases. For a given λ, the larger the damping the more the ξ-coordinate is forced to assume a purely circumferential direction.

The expression for the metric tensor component g_{23} can be written using Eq. (A30) in Appendix A as

$$g_{23} = -\frac{\Omega r}{U}\frac{r}{R}\frac{U'(r)\gamma}{U} + \left[\left(\frac{V}{U^2}U'(r) - \frac{V'(r)}{U}\right)\gamma + A'(r)B(\xi)\right]A(r)B'(\xi). \tag{6.16}$$

From Eq. (6.6) and the values of ξ_B, the term $A'(r)B(\xi) = 0$ at the N_B blade locations. Furthermore, since g_{13} is zero at these positions, inspection of Eq. (6.7) reveals that $AB' = (\Omega R/V)(r/R)^2$ at the blades also. Then, for this case, the metric tensor component g_{23} reduces to

$$\begin{aligned} g_{23}\Big|_{\xi=\xi_B} &= -\frac{\Omega r}{U}\frac{r}{R}\frac{U'\gamma}{U} + \left(\frac{V}{U^2}U' - \frac{V'}{U}\right)\gamma\frac{\Omega R}{V}\left(\frac{r}{R}\right)^2 \\ &= -\frac{\Omega R}{V}\left(\frac{r}{R}\right)^2\frac{V'\gamma}{U}\,. \end{aligned} \tag{6.17}$$

By inspection, requiring V to be a constant is sufficient to render $g_{23} = 0$. In this way, both g_{23} and g_{13} are made equal to zero at the blade stations defined in Eq. (6.11).

Thus, the ξ-coordinate lines will be orthogonal to the helical sheets containing the mean camber locations of the blades provided that $A(r)$ and $B(\xi)$ are defined as above and that the axial velocity V is a constant. The last constraint is a realistic restriction because a constant value of V is the most reasonable case and the one of most interest.

The second objective is the requirement that the axial distance be the same for corresponding points at each periodic boundary. This is easily verified as being satisfied by inspecting the transformation of z on the helical sheets lying midway between successive blades. From Eq. (6.15), it is seen that

$$z_{PB} = z\Big|_{\xi=\xi_{PB}} = -\gamma \frac{V}{U} \tag{6.18}$$

when $\frac{\xi}{\xi_m} = \frac{\xi_{PB}}{\xi_m} = \begin{cases} \pm 1, \pm 3, \ldots, \pm(N_B - 2), N_B; & \text{for } N_B \text{ odd} \\ \pm 1, \pm 3, \ldots, \pm(N_B - 3), \pm(N_B - 1) & \text{for } N_B \text{ even} \end{cases}$

where the subscript PB denotes "periodic boundary." This relation shows that the net axial distance is not changed upon a complete traverse via a ξ-coordinate line from one periodic sheet to any other. In fact, moving a value of twice ξ_m along any ξ-coordinate restores the original axial location. That this is true can be seen by inspecting Eq. (6.15). The consequence of this is that any set of sheets separated by a value equal to the blade spacing $2\xi_m$ could be used as periodic boundary sheets.

6.4 Final Form of the Periodic Helical Coordinates

For convenience, the transformation of the helical coordinates $\gamma = y^1$, $r = y^2$, $\xi = y^3$ to the Cartesian coordinates $x = x^1$, $y = x^2$, $z = x^3$ is given in terms of the nonsuperscripted variables:

$$x = r \sin\left(\frac{\Omega}{U}\gamma + \frac{\xi}{R}\right) \tag{6.19}$$

$$y = r \cos\left(\frac{\Omega}{U}\gamma + \frac{\xi}{R}\right) \tag{6.20}$$

$$z = -\gamma \frac{V}{U} + \frac{\xi_m}{\pi} \frac{\Omega R}{V} \frac{r^2}{R^2} \exp\left(-a_o \frac{|\bar{\xi}|}{\xi_m}\right) \sin\left(\frac{\xi}{\xi_m}\pi\right). \tag{6.21}$$

This is the set of coordinates which is used in the solution of the small disturbance equation presented in Chapter IV. Various other cases

of these coordinates could have been specified. For example, if either $A(r)$ or $E(\xi)$ of equation (6.3) is chosen equal to zero, then the ξ-curves become circles about the z-axis. As another special case, if $B(\xi) = \xi$ is chosen, then the ξ-curves are helices. On each helix the coordinate value varies as the arc length divided by the value of the radius at which that given helix lies. This distinguishes them from the original helical coordinates given in Appendix B. The metric tensors are given in the latter part of Appendix A for these special cases.

VII. NUMERICAL APPROACH

This chapter presents a general description of the numerical approach used to solve the small disturbance equation derived in Chapter IV. For the sake of convenience, the small disturbance equation will be rewritten letting $y^1 = \gamma$, $y^2 = r$, and $y^3 = \xi$, as discussed in Chapter VI. With this notation Eq. (4.39) can be written

$$A_1 \frac{\partial^2 \varphi}{\partial \gamma \partial t} = \frac{\partial}{\partial \gamma}\left[A_2 \left(\frac{\partial \varphi}{\partial \gamma}\right)^2 + A_3 \frac{\partial \varphi}{\partial \gamma}\right] + A_4 \frac{\partial^2 \varphi}{\partial r^2} + A_5 \frac{\partial^2 \varphi}{\partial \xi^2} + A_6 \frac{\partial^2 \varphi}{\partial \gamma \partial r} + A_7 \frac{\partial^2 \varphi}{\partial \gamma \partial \xi} + A_8 \frac{\partial^2 \varphi}{\partial r \partial \xi} . \tag{7.1}$$

where

$$A_1 = \frac{2MM_T\varepsilon}{\delta^{2/3}} \tag{7.2a}$$

$$A_2 = -\frac{1}{2}(k+1)MM_T g^{11} \tag{7.2b}$$

$$A_3 = \frac{g^{11} - M^2}{\delta^{2/3}} \tag{7.2c}$$

$$A_4 = \frac{\varepsilon^2}{\delta^{2/3}} g^{22} = \frac{\varepsilon^2}{\delta^{2/3}} \tag{7.2d}$$

$$A_5 = g^{33} \tag{7.2e}$$

$$A_6 = \frac{2\varepsilon}{\delta^{2/3}} g^{12} \tag{7.2f}$$

$$A_7 = \frac{2}{\delta^{1/3}} g^{13} \tag{7.2g}$$

$$A_8 = \frac{2\varepsilon}{\delta^{1/3}} g^{23}. \tag{7.2h}$$

In transferring the two terms on the left-hand side of Eq. (4.39) to the right-hand side in Eq. (7.1), they have been lumped together with the understanding that the variation of g^{11} with respect to γ is small. Recall that M is a function of r only and, therefore, the only dependence of A_2 or A_3 on γ is through g^{11}.

It is convenient to define the two bracketed terms in Eq. (7.1) above by F so that:

$$F_\gamma = \frac{\partial}{\partial\gamma}\left[A_2\left(\frac{\partial\varphi}{\partial\gamma}\right)^2 + A_3\,\frac{\partial\varphi}{\partial\gamma}\right]. \tag{7.3}$$

Equation (7.1) is then written as

$$A_1\,\frac{\partial^2\varphi}{\partial\gamma\partial t} = F_\gamma + A_4\,\frac{\partial^2\varphi}{\partial r^2} + A_5\,\frac{\partial^2\varphi}{\partial\xi^2} + A_6\,\frac{\partial^2\varphi}{\partial\gamma\partial r} + A_7\,\frac{\partial^2\varphi}{\partial\gamma\partial\xi} + A_8\,\frac{\partial^2\varphi}{\partial r\partial\xi}\ . \tag{7.4}$$

Except for the presence of the last two terms, this equation has the same form as the equation solved in Isom (Ref. 5) where an ADI method based on the Douglas-Gunn algorithm was used to solve the finite difference form of the equation for flow about helicopter rotors. The additional cross-derivative terms will be handled by generalizing the Douglas-Gunn algorithm. With modest changes this allows the numerical code developed for the helicopter problem to be used for the current work.

It should be pointed out that Eq. (7.4) remains expressed in terms of unstretched physical variables. No mapping of the coordinate system has been carried out so as to produce a nonuniform grid. For simplicity, the numerical algorithm will be presented for the case where there is no coordinate stretching. Following this, the method of introducing coordinate stretching will be explained.

7.1 ADI Douglas-Gunn Algorithm

For three dimensions, the ADI technique involves splitting the given equation into three separate finite difference equations which can be solved successively to complete one time-step increment. A current estimate of φ, say, φ^n is advanced to φ^{n+1} through two intermediate values, which will be denoted by φ^* and φ^{**}, to complete a single stage of iteration.

To begin an iteration at time step n, φ^n is advanced to φ^* by solving the first equation with only the γ-direction being differenced implicitly; this is called the γ-sweep. Next, in the r-sweep, φ^* is advanced to φ^{**} by solving the second equation with only the r-direction being implicit. Finally, in the ξ-sweep, φ^{**} is advanced to φ^{n+1} by solving the third equation with the ξ-direction being the only implicit direction.

The three equations for the respective sweeps are given for a uniform grid as:

γ-sweep:

$$\frac{A_1}{\Delta t}\,\delta_\gamma(\varphi^* - \varphi^n) = D_\gamma F_I + A_4\delta_{rr}\varphi^n + A_5\delta_{\xi\xi}\varphi^n + A_6\delta_{\gamma r}\varphi^n + A_7\delta_{\gamma\xi}\varphi^n + A_8\delta_{r\xi}\varphi^n. \qquad (7.5a)$$

r-sweep:

$$\frac{A_1}{\Delta t}\,\delta_\gamma(\varphi^{**} - \varphi^n) = D_\gamma F_I + \frac{A_4}{2}\,\delta_{rr}(\varphi^{**} + \varphi^n) + A_5\delta_{\xi\xi}\varphi^n + \frac{A_6}{2}\,\delta_{\gamma r}(\varphi^{**} + \varphi^n) + A_7\delta_{\gamma\xi}\varphi^n + A_8\delta_{r\xi}\varphi^n. \qquad (7.5b)$$

ξ-sweep:

$$\frac{A_1}{\Delta t}\delta_\gamma(\varphi^{n+1} - \varphi^n) = D_\gamma F_I + \frac{A_4}{2}\delta_{rr}(\varphi^{**} + \varphi^n) + \frac{A_5}{2}\delta_{\xi\xi}(\varphi^{n+1} + \varphi^n)$$

$$+ \frac{A_6}{2}\delta_{\gamma r}(\varphi^{**} + \varphi^n) + \frac{A_7}{2}\delta_{\gamma\xi}(\varphi^{n+1} + \varphi^n) + \frac{A_8}{2}\delta_{r\xi}(\varphi^{n+1} + \varphi^n). \qquad (7.5c)$$

where D_γ is a special difference operator to be explained below and δ_{rr}, $\delta_{\xi\xi}$, ..., $\delta_{r\xi}$ are standard difference operators in the indicated directions. Here, F represents the bracketed terms of Eq. (7.1) which correspond to the flux in the γ-direction, and $D_\gamma F_I$ gives the finite difference approximation to $\partial F/\partial\gamma$ at the I^{th}-node for each set of values of J and K. The nodal values I, J, and K are associated with the γ, r, and ξ directions, respectively. The three directions have uniform step-sizes $\Delta\gamma$, Δr, and $\Delta\xi$, which may be distinct.

An example of how the difference operators in Eq. (7.5) are defined in terms of difference approximations is given as follows

$$\delta_{rr}\varphi^n = \frac{1}{(\Delta r)^2}\left(\varphi^n_{I,J+1,K} - 2\varphi^n_{I,J,K} + \varphi^n_{I,J-1,K}\right). \qquad (7.6)$$

An analogous expression may be readily written for $\delta_{\xi\xi}$. In the case of the mixed second-order operators, the following is used.

$$\delta_{\gamma r}\varphi^n = \frac{1}{\Delta\gamma\Delta r}\left(\varphi^n_{I,J+1,K} - \varphi^n_{I,J,K} - \varphi^n_{I-1,J+1,K} + \varphi^n_{I-1,J,K}\right). \qquad (7.7)$$

Corresponding expressions hold for $\delta_{\gamma\xi}$ and $\delta_{r\xi}$.

The nonlinear term contained in $D_\gamma F_I$ is linearized by averaging at the n and * time levels by defining

$$F_{I+1/2} = A_2\left(\delta_\gamma\varphi^n_{I,J,K}\right)\left(\delta_\gamma\varphi^*_{I,J,K}\right) + \frac{1}{2}A_3\delta_\gamma\left(\varphi^n_{I,J,K} + \varphi^*_{I,J,K}\right) \qquad (7.8)$$

to be the flux at the midpoint of the I^{th}-cell on any node line given by J and K. The Murman-Cole type-dependent differencing scheme is

introduced to provide stable differencing as explained in Chapter III by defining

$$D_\gamma F_I = \frac{1}{\Delta\gamma}\left[\varepsilon_I(F_{I+1/2} - F_{I-1/2}) + (1 - \varepsilon_{I-1})(F_{I-1/2} - F_{I-3/2})\right]. \tag{7.9}$$

where

$$\varepsilon_I = \begin{cases} 1, & V_c > 0 \\ 0, & V_c < 0 \end{cases} \tag{7.10}$$

and

$$V_c = A_2\varphi_\gamma + A_3. \tag{7.11}$$

This switches the difference equations at each grid point according to whether the flow field at that point is subsonic, sonic, supersonic, or a shock.

A more convenient set of equations for numerical computations is obtained from the set given in Eq. (7.5) by subtracting Eq. (7.5a) from Eq. (7.5b) and Eq. (7.5b) from Eq. (7.5c), producing, with some rearrangement, the following set:

γ-sweep:

$$\frac{A_1}{\Delta t}\delta_\gamma(\varphi^* - \varphi^n) - D_\gamma F_I = A_4\delta_{rr}\varphi^n + A_5\delta_{\xi\xi}\varphi^n + A_6\delta_{\gamma r}\varphi^n + A_7\delta_{\gamma\xi}\varphi^n + A_8\delta_{r\xi}\varphi^n; \tag{7.12a}$$

r-sweep:

$$\left(\frac{A_1}{\Delta t}\delta_\gamma - \frac{A_4}{2}+\delta_{rr} - \frac{A_6}{2}\delta_{\gamma r}\right)(\varphi^{**} - \varphi^*) = \left(\frac{A_4}{2}\delta_{rr} - \frac{A_6}{2}\delta_{\gamma r}\right)(\varphi^* - \varphi^n); \tag{7.12b}$$

ξ-sweep:

$$\left(\frac{A_1}{\Delta t}\delta_\gamma - \frac{A_5}{2}\delta_{\xi\xi} - \frac{A_7}{2}\delta_{\gamma\xi} - \frac{A_8}{2}\delta_{r\xi}\right)(\varphi^{n+1} - \varphi^{**}) = \left(\frac{A_5}{2}\delta_{\xi\xi} + \frac{A_7}{2}\delta_{\gamma\xi} + \frac{A_8}{2}\delta_{r\xi}\right)(\varphi^{**} - \varphi^n). \tag{7.12c}$$

The equations in Eq. (7.12) have been arranged into the so-called delta form where the unknowns on the left-hand sides are expressed as differences in the potential. This form has superior numerical properties compared with those in Eq. (7.5). The solution to the above set of equations involves no more than solving tridiagonal matrices, except in the case of a shock point where a quadridiagonal matrix occurs in the γ-sweep. The potential at time level $n+1$ can be found from the potential at level n by adding the solutions for the delta differences from all sweeps to φ^n as

$$\varphi^{n+1} = \varphi^n + (\varphi^* - \varphi^n) + (\varphi^{**} - \varphi^*) + (\varphi^{n+1} - \varphi^{**}). \qquad (7.13)$$

The sequencing of the solution along lines of grid points for each of the three sweeps is illustrated in Fig. 7.1. The γ-sweep is marched from upstream to downstream along rows of grid points where each row is characterized by constant values of r and ξ. The iteration in this sweep proceeds along rows in a plane of constant ξ by advancing sequentially to the row with the next higher value of r. When all rows of the current ξ-plane are completed, the process is repeated for the plane with the next higher value of ξ. When every plane has been swept through, the solution has advanced to φ^*. Similarly, the iteration proceeds in the r-sweep along rows of constant γ and ξ by sequencing the rows through successive planes of constant ξ. This takes the solution to φ^{**}. Since the value of ξ varies in the ξ-sweep, this last sweep proceeds along planes of constant r. When the last plane has been completed, the solution has advanced to φ^{n+1}. This completes one full iteration.

As is common in ADI methods, the time step is varied from iteration to iteration over the course of the calculation from some maximum value

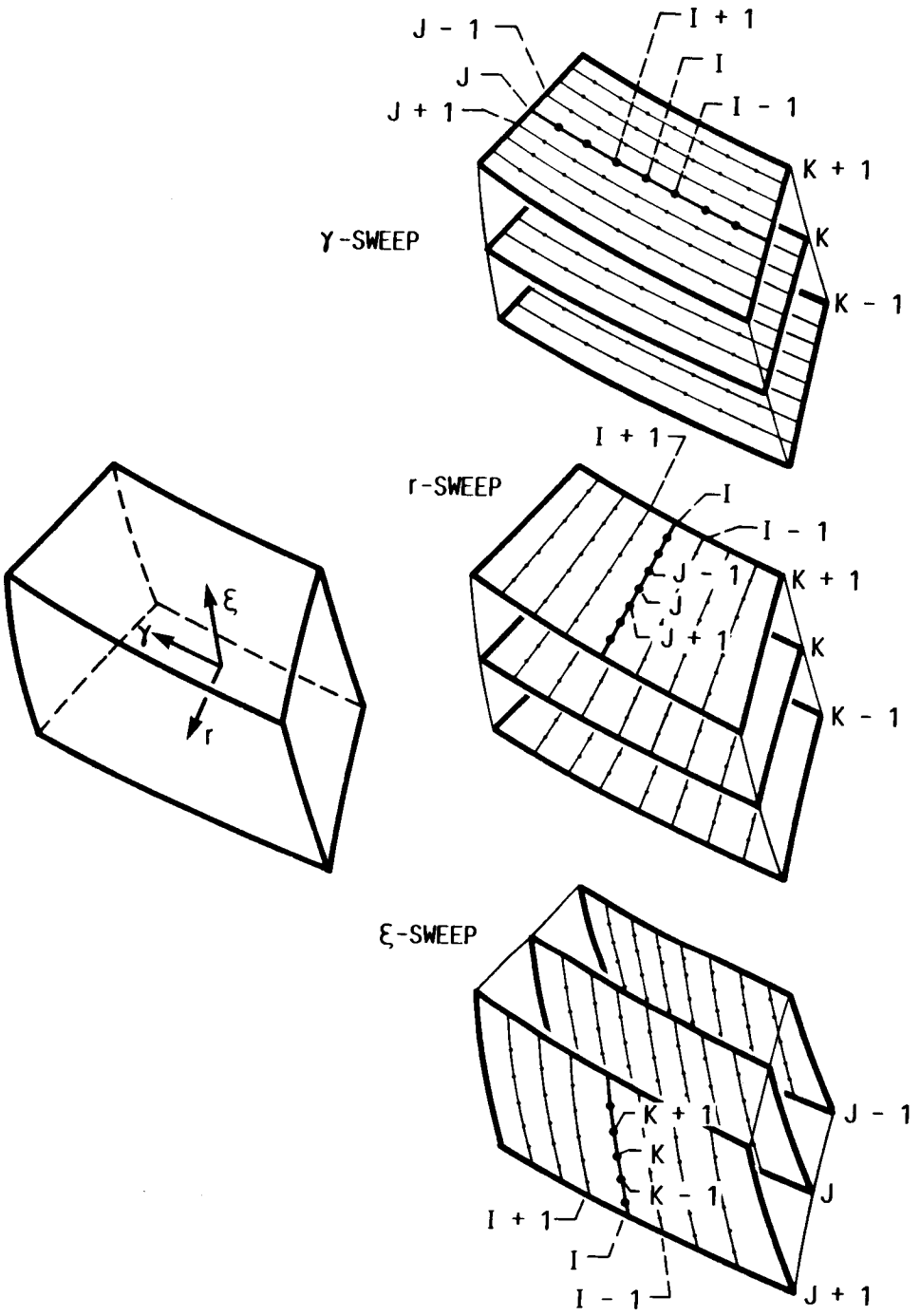

FIGURE 7.1. - THE THREE SWEEPS OF A COMPLETE ADI ITERATION.

Δt_{max} to some minimum value Δt_{min}. This is done to improve the convergent rate of the calculation. The geometric sequence

$$\Delta t_i = \Delta t_{min} \left(\frac{\Delta t_{max}}{\Delta t_{min}} \right)^{(i-1)/(N-1)} \qquad i = 1, 2, 3, \ldots N \qquad (7.14)$$

is used for N iterations (N = 8) and then repeated until the total number of iterations has been reached. The total number of iterations is determined by a preset value for the maximum number of iterations, or by either satisfying a convergence criterion or exceeding an error bound. The range in the time step for the sequence of iterations addresses both high- and low-frequency components of the error. In general, the range of Δt_{min} and Δt_{max} must be determined by trial and error and is strongly influenced by the size of the computational mesh.

7.2 Grid Stretching

Thus far, the physical mesh has been considered to be a uniform grid. However, it is preferable to have the grid points clustered in regions of high gradients and sparsely distributed in regions of low gradients. Grid stretching is a means of accomplishing this. It is used here to distribute the physical mesh points such that they are more heavily clustered near the airfoil than away from it with the greatest concentrations near the leading and trailing edges. The grid is smoothly stretched from the airfoil surfaces to a coarse grid at the outer boundaries of the flow field. The stretching is performed in all three coordinate directions. It is defined in a general sense as a mapping of the physical space $\gamma r \xi$ to a uniform computational space $\bar{\gamma} \bar{r} \bar{\xi}$ by

$$\gamma = \gamma(\bar{\gamma}, \bar{r}), \quad r = r(\bar{r}), \quad \xi = \xi(\bar{\xi}). \qquad (7.15)$$

It should be noted that the physical coordinates r and ξ are stretched by their respective computational coordinates. However, γ is a function of both $\bar{\gamma}$ and $\bar{r}$. The added dependence of γ on $\bar{r}$ is necessary to accommodate swept wings.

The coordinate stretching is introduced through the conventional chain rule formulas which are given in Appendix C. By replacing the various partial derivatives in Eq. (7.1) with those obtained by the chain rule, this equation is generalized to stretched grids. The use of coordinate stretching complicates, but does not change, the basic form of the ADI algorithm.

VIII. DISCUSSION AND RESULTS

This discussion focuses on the results obtained for flow over a single blade of an eight bladed cascade. As explained in the introduction, the blades of this cascade are simple bicircular arc profiles with a maximum blade thickness of 5 percent. Furthermore, the planform of the blades is rectangular with the required spanwise twist made about the leading edge. This produces a blade of constant chord length. The aspect ratio of the blades is defined as the ratio of the blade-tip radius, as measured from the axis, divided by the chord length. All the results here are for blades with an aspect ratio of 4:1. The hub of the propeller system is placed at a radius of 0.375 R, where R is the tip radius; this gives an effective aspect ratio of 2.5 for a blade length measured from the hub, rather than from the axis.

There are a number of reasons for using the blade geometry described above. The main reason is to provide a simple propeller geometry. By using a simple geometry, the flow will be uncomplicated by the effects which would otherwise arise by using a complex blade shape. The propeller geometry is simple for any specified advance ratio. Another reason is that the bicircular arc profile is widely used as a model profile in flow simulation studies. The front-to-back and top-to-bottom symmetry of the blade produces symmetrical flow for the case of a very high advance ratio and a zero angle of attack. For the case of a nonzero angle of attack, lift can be introduced simply by rotating the blade about the pitch change axis. Thus, a host of

propeller geometries can easily be generated by this method of specifying the blade construction. This, in turn, means that many different flow cases can be specified simply by prescribing the advance ratio, the angle of attack, and the Mach number of the approaching flow. Furthermore, any investigator who wishes to repeat the calculations can unambiguously reconstruct the propeller geometry. Because of these features, such a propeller system serves as a good prototype for flow investigation.

Four separate test cases are solved numerically in this investigation. These test cases are indicated in Table 8-1 by their respective values of the advance ratio λ, the helical Mach number of the approaching flow M_R, and the angle of attack α. The first case to be studied is the case of very high advance ratio $\lambda = 100$ with a subsonic free-stream Mach number $M_R = 0.8$ and a zero angle of attack $\alpha = 0.0°$. Because this flow is essentially an axial flow, it represents a limiting case for zero propeller rotation. The second case studied is for an advance ratio $\lambda = 1$, but with the same free-stream Mach number $M_R = 0.8$ and the same angle of attack $\alpha = 0.0°$ as used in the first case. The value $\lambda = 1$ is typical for a propeller. The third case studied is for an advance ratio $\lambda = 1$ and an angle of attack $\alpha = 0.0°$, but for a transonic free-stream Mach number $M_R = 1.1$. The values of λ and M_R for the third case are typical of an advanced turboprop. The fourth case is for an advance ratio $\lambda = 1$ and a free-stream Mach number $M_R = 1.1$, as in the third case, but now a nonzero angle of attack $\alpha = 2.0°$ is specified. Thus, the four cases present two values for each of the three varied parameters. The third case will include a separate study on the effect of grid refinement on the

solution. In addition, for the first three cases, the results obtained from the helical small disturbance (HSD) code are compared with results obtained from an Euler code (Ref. 6) These results are presented in the form of constant Mach number contours on the blade surfaces and selected cross-channel and blade-to-blade surfaces. All solution computations were made using a Cray X-MP/24. The number of numerical iterations used in computing the solutions for all test cases was 5000 for both codes. The computational time used by the HSD solution code was approximately 60 percent of the computation time used by the Euler solution code. The Euler solution code required approximately three times the amount of computer memory of that used by the HSD solution code. Before discussing the results, the grids used in the computations for the HSD solution code and the Euler solution code will be detailed.

Mesh lines for the HSD solution computations are shown (for the case $\lambda = 1$) in Fig. 8.1 where, for clarity, only every third line is included from the leading edge to the trailing edge of the blade. A uniform grid extended over the blade surface and a stretched grid extended over the following regions: from the leading edge to the upstream boundary, from the blade tip to the outer radial boundary, and from the blade surface to the periodic boundary. The number of grid intervals for each computational direction is indicated in Table 8-2. The grid contained 30 intervals along the blade in the streamwise direction and an additional 11 grid intervals both upstream and downstream of the blade, for a total of 52 streamwise intervals. In the radial direction, 20 grid intervals were used, with half of these being on the blade. In the circumferential direction, 20 grid intervals were used from the lower to the upper periodic boundary. The total grid,

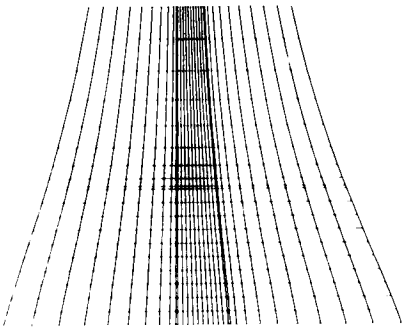

(A) VIEW NORMAL TO AXIS SHOWING PROJECTED VIEW OF HELICAL SHEET CONTAINING BLADE.

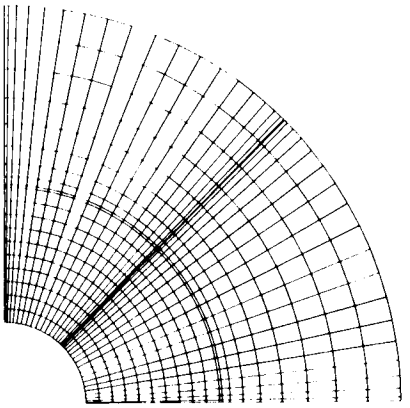

(B) CROSS-CHANNEL VIEW AT LEADING EDGE.

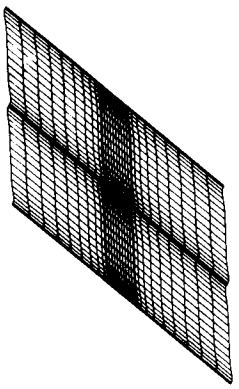

(C) BLADE-TO-BLADE VIEW ACROSS TWO CHANNELS; NOT ALL GRID POINTS ARE SHOWN ALONG BLADE SURFACE.

FIGURE 8.1. - HELICAL COORDINATES USED IN SMALL DISTURBANCE COMPUTATION.

therefore was 52 by 20 by 20 intervals. The upstream and downstream boundaries were located 4 chord lengths from the leading and trailing edges of the blade, respectively. The outer radial boundary was placed one blade diameter from the axis.

This grid was used as the standard grid in computing most HSD solutions for the test cases. As discussed earlier for case 3, a series of grids in addition to this standard grid was used to investigate the effect of grid refinement. This additional series of grids is described and the effect of grid density on the solution is discussed following the discussion of the case 3 results for the standard grid.

For the Euler equation computations, the same unstretched grid extended over the blade surface. Otherwise, the grid was stretched as above, but with a different stretching function and no stretching in the circumferential direction. A representative grid, coarser than what was actually used for the Euler calculations, is shown in Fig. 8.2 for the case of $\lambda = 1$. The number of grid intervals for each direction is given in Table 8-2. The position of the blade is indicated by the narrow opening (visible in Fig. 8.2(b)) of the grid lines near the hub. The grid of Fig. 8.2(c) illustrates how the streamwise grid transitions from an axial direction upstream of the blade to a helical direction near the blade and back to an axial direction downstream. Since the blade-to-blade direction is purely circumferential, this results in a high degree of coordinate shearing at axial locations near the blade. In addition, the chordwise distribution of grid points is not symmetric front to back along the blade surface, nor is it symmetric from the suction to the pressure side; this asymmetry increases with blade thickness and stagger. The upstream and downstream boundaries were

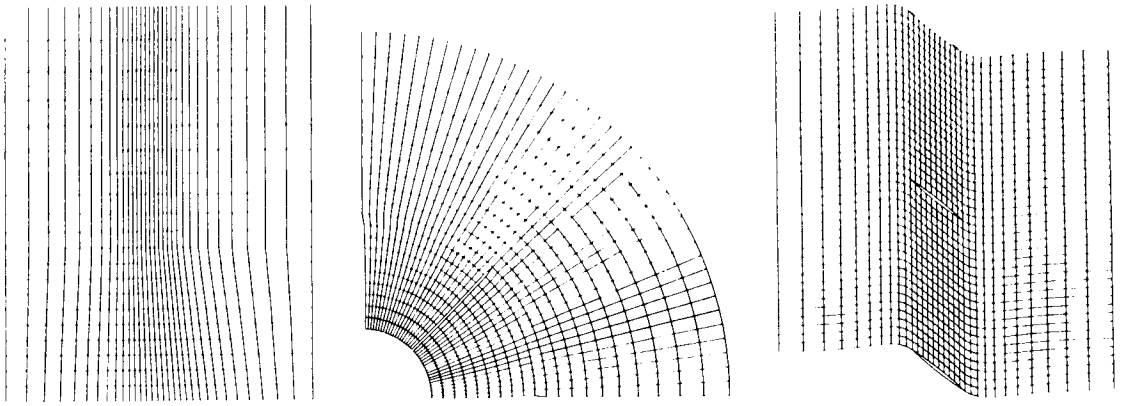

(A) VIEW NORMAL TO AXIS.

(B) VIEW ALONG AXIS SHOWING THE MIDCHORD STATION.

(C) VIEW OF BLADE-TO-BLADE SURFACE SHOWING THREE BLADES. GRID SHOWN IS COARSER IN AXIAL DIRECTION THAN THAT USED.

FIGURE 8.2. - COORDINATES USED IN EULER COMPUTATION.

placed at two chord lengths from the leading and trailing edges of the blade, respectively. These boundaries were positioned differently from the corresponding HSD boundaries because of the difference between the two meshes in the streamwise direction. The outer radial boundary was located as in the HSD mesh, at one blade diameter from the axis.

The computational results for the four propeller cases outlined above will now be discussed. Although the grids used in computing the solutions for these cases are coarse, based on two-dimensional standards, they are realistic for three-dimensional computations. The grid densities used in these calculations are sufficient to provide good overall prediction of the physics of the flow, but with some lack of detail, such as smearing of a shock. It is hoped that the following cases can serve as test cases for other researchers.

Case 1) $\lambda = 100$, $M_R = 0.8$, $\alpha = 0°$

This case was chosen to examine the effect that blade cascading has on the solution. For the value of $\lambda = 100$, the flow is essentially axial. Since the blade is symmetric from front to back and from top to bottom and $\alpha = 0$, the solution should reflect this symmetry if no losses occur in the flow field. For the value of $M_R = 0.8$ and the thin 5 percent thick blade, no shocks were detected in the flow field. The expected symmetry is noticeable in the solutions of both the HSD and the Euler codes. Figure 8.3 shows HSD Mach contours on the blade surface with the minimum contour being 0.75 and the maximum 0.9; the results are identical for the pressure surface and the suction surface. The results reveal the expected drop-off in Mach number with increasing radius. Similar results are shown in Fig. 8.4 where identical contour values are plotted for the Euler code. The contour

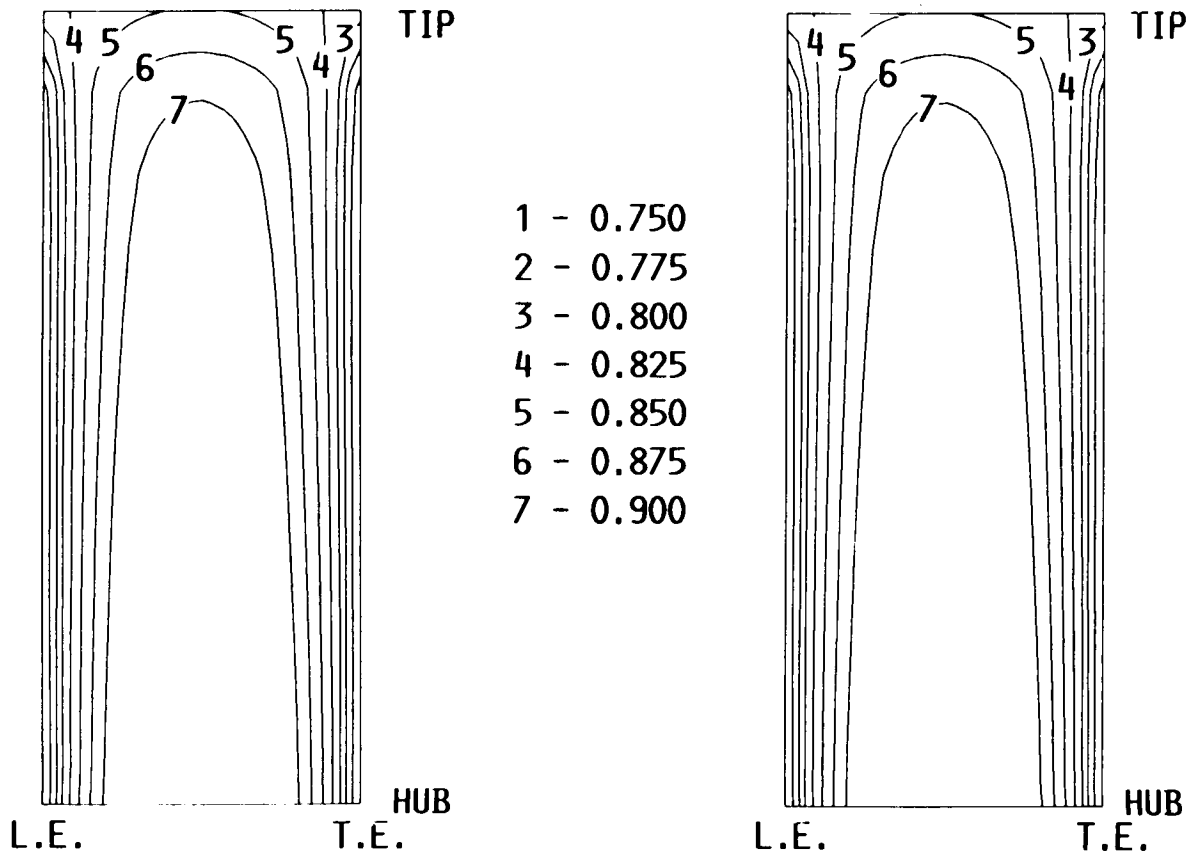

(A) PRESSURE SURFACE. (B) SUCTION SURFACE.

FIGURE 8.3. - MACH CONTOURS OF SMALL DISTURBANCE COMPUTATION ON BLADE SURFACES: ADVANCE RATIO = 100, M_R = 0.8, $\alpha = 0^o$.

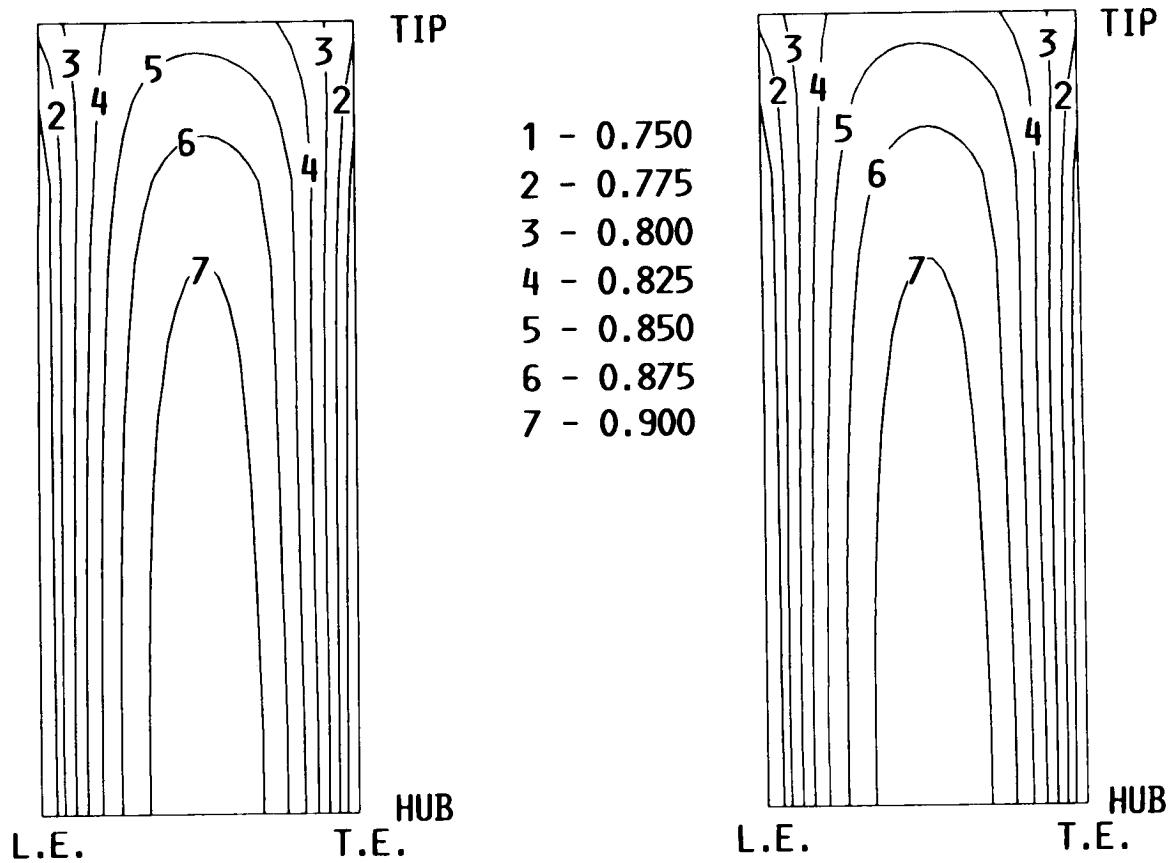

(A) PRESSURE SURFACE. (B) SUCTION SURFACE.

FIGURE 8.4. - MACH CONTOURS OF EULER COMPUTATION ON BLADE SURFACES: ADVANCE RATIO = 100, M_R = 0.8, $\alpha = 0^o$.

shapes obtained from the two codes are very similar, with the only essential difference being that the Mach number produced at a given blade location is higher for the HSD code.

Symmetry is again found for Mach contours in the cross-section planes given in Figs. 8.5 and 8.6 for the HSD and Euler codes, respectively. Again, the shapes obtained by the two codes are similar, with the HSD results showing more flow acceleration through the passage. The similarity in shapes indicates that qualitatively the solutions are being calculated correctly within the interior region of the flow, as well as at the blade surfaces.

The solutions on the blade-to-blade surfaces are given in Figs. 8.7 and 8.8 for the HSD and Euler codes respectively. In each case Mach contours are shown for three different span stations along the blade. The minimum contour value is 0.8. The values of the maximum contours are as follows: 1.0 for Fig. 8.7(a); 0.92 for Fig. 8.7(b); 0.86 for Fig. 8.7(c); 0.88 for Fig. 8.8(a); and 0.86 for Figs. 8.8(b) and 8.8(c). The results are symmetric and support the result that the HSD code predicts flows that agree with the Euler code except in magnitude, at least for subsonic and axial flow.

Case 2) $\lambda = 1$, $M_R = 0.8$, $\alpha = 0°$

This case is presented to isolate the effect of blade rotation. The free-stream axial Mach number is only 0.5657, although $M_R = 0.8$. The effect of operating at a low advance ratio is seen in Figs. 8.9 and 8.10, which give Mach contours on the blade surface, for the HSD and Euler computations, respectively. These contours are given for constant Mach numbers that range from 0.6 to 0.8 in each case. Other than the expected result that the flow Mach number would increase toward the

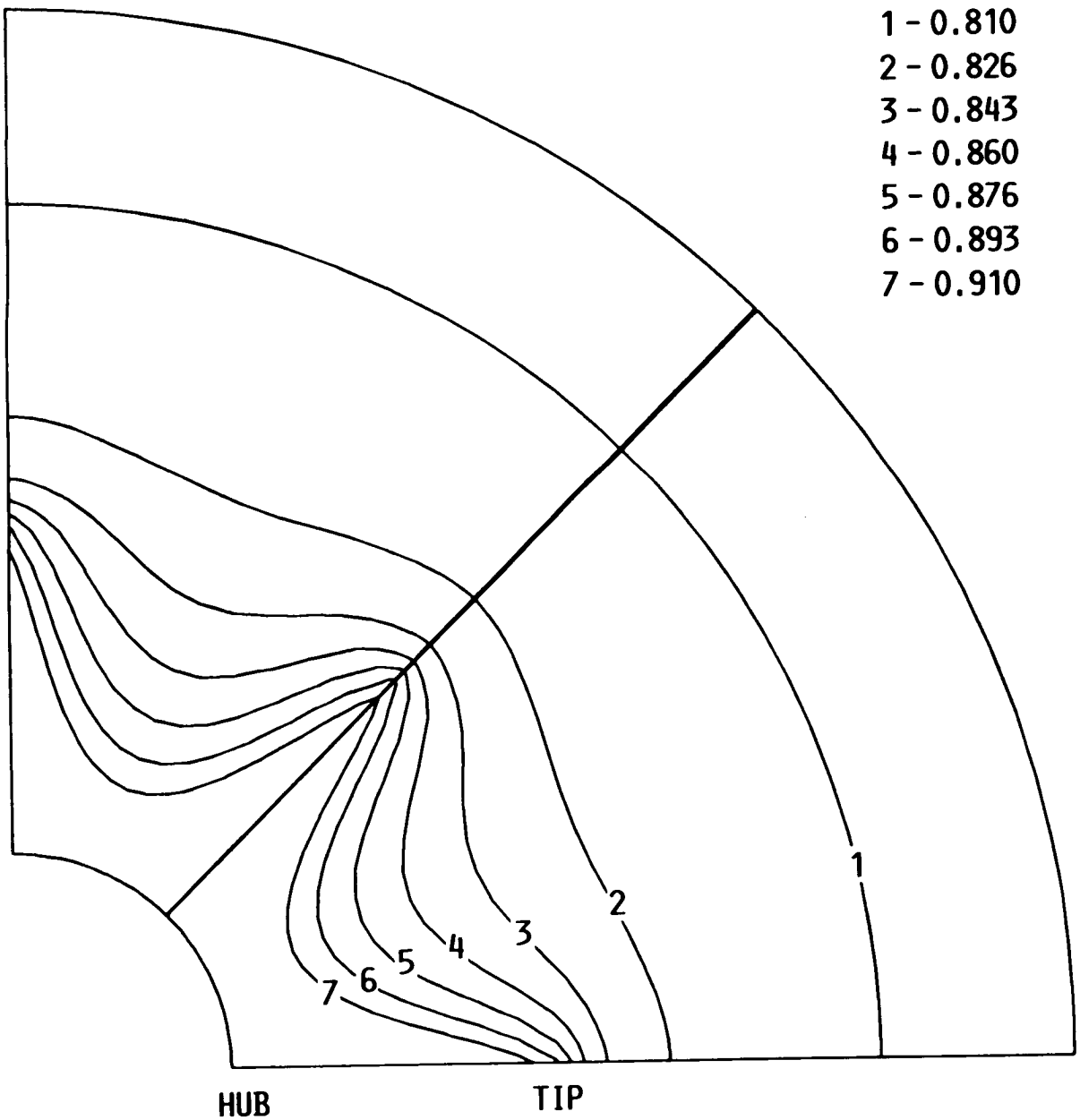

FIGURE 8.5. - MACH CONTOURS OF SMALL DISTURBANCE COMPUTATION IN CROSS PLANE AT MIDCHORD AXIAL LOCATION: ADVANCE RATIO = 100, $M_R = 0.8, \alpha = 0^o$.

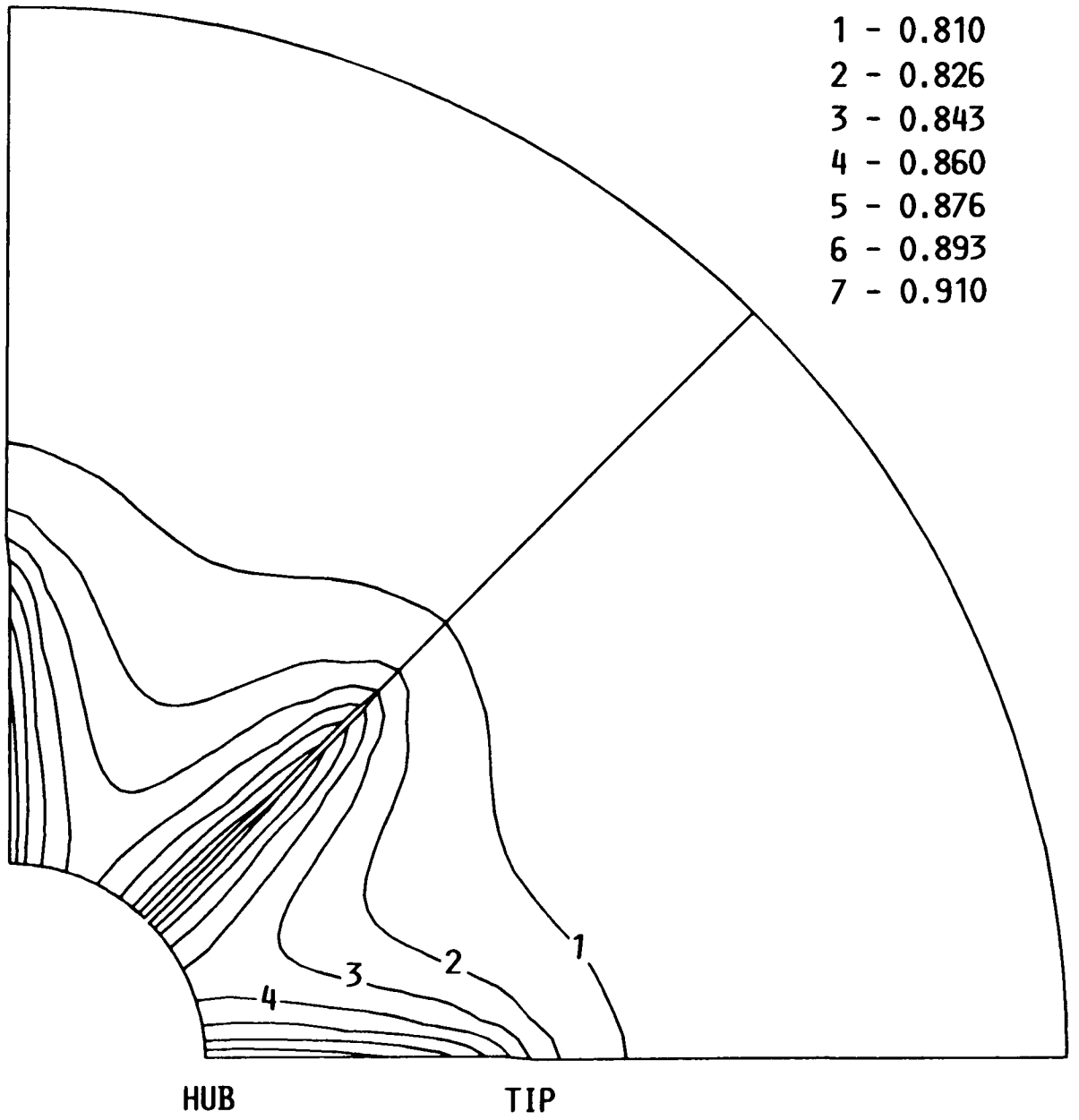

FIGURE 8.6. - MACH CONTOURS OF EULER COMPUTATION IN CROSS PLANE AT MIDCHORD AXIAL LOCATION: ADVANCE RATIO = 100, M_R = 0.8, $\alpha = 0^o$.

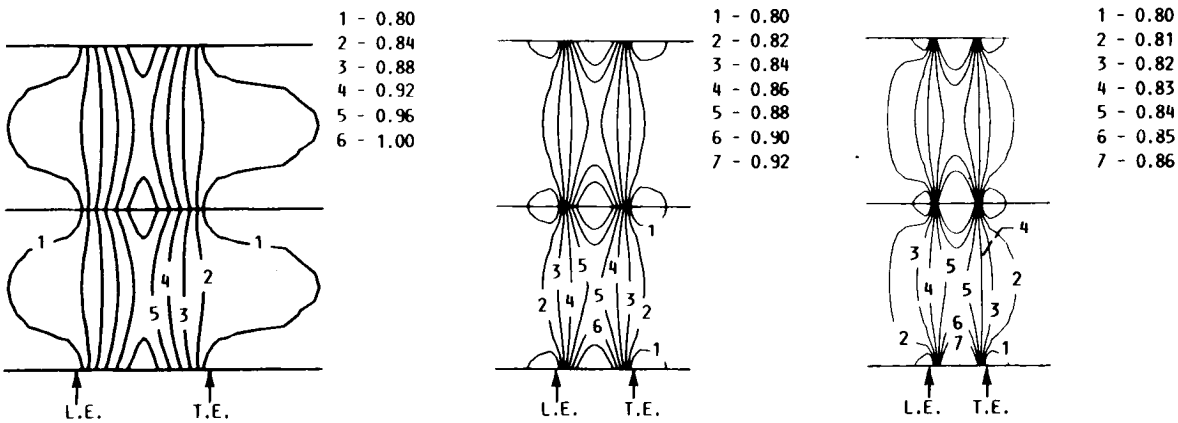

FIGURE 8.7. - MACH CONTOURS OF SMALL DISTURBANCE COMPUTATION ON BLADE-TO-BLADE SURFACES AT VARIOUS SPAN LOCATIONS: ADVANCE RATIO = 100, M_R = 0.8, $\alpha = 0^o$.

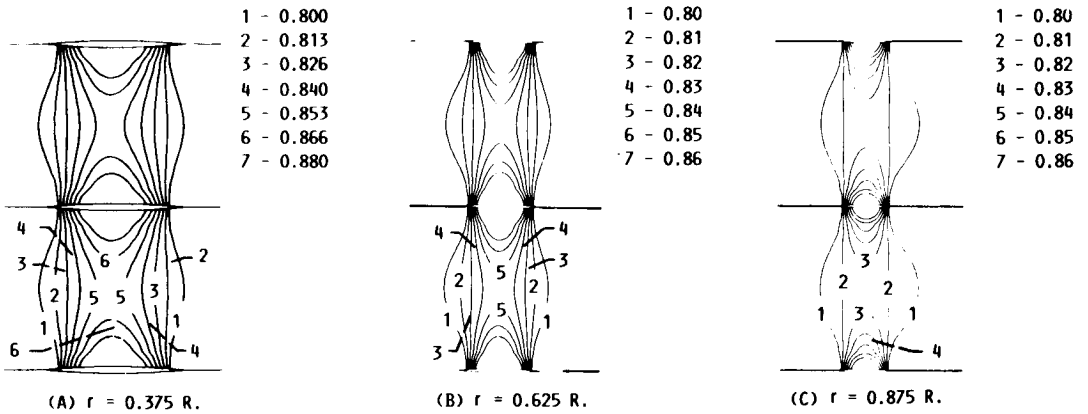

(A) r = 0.375 R. (B) r = 0.625 R. (C) r = 0.875 R.

FIGURE 8.8. - MACH CONTOURS OF EULER COMPUTATION ON BLADE-TO-BLADE SURFACES AT VARIOUS SPAN LOCATIONS: ADVANCE RATIO = 100, M_R = 0.8, $\alpha = 0^0$.

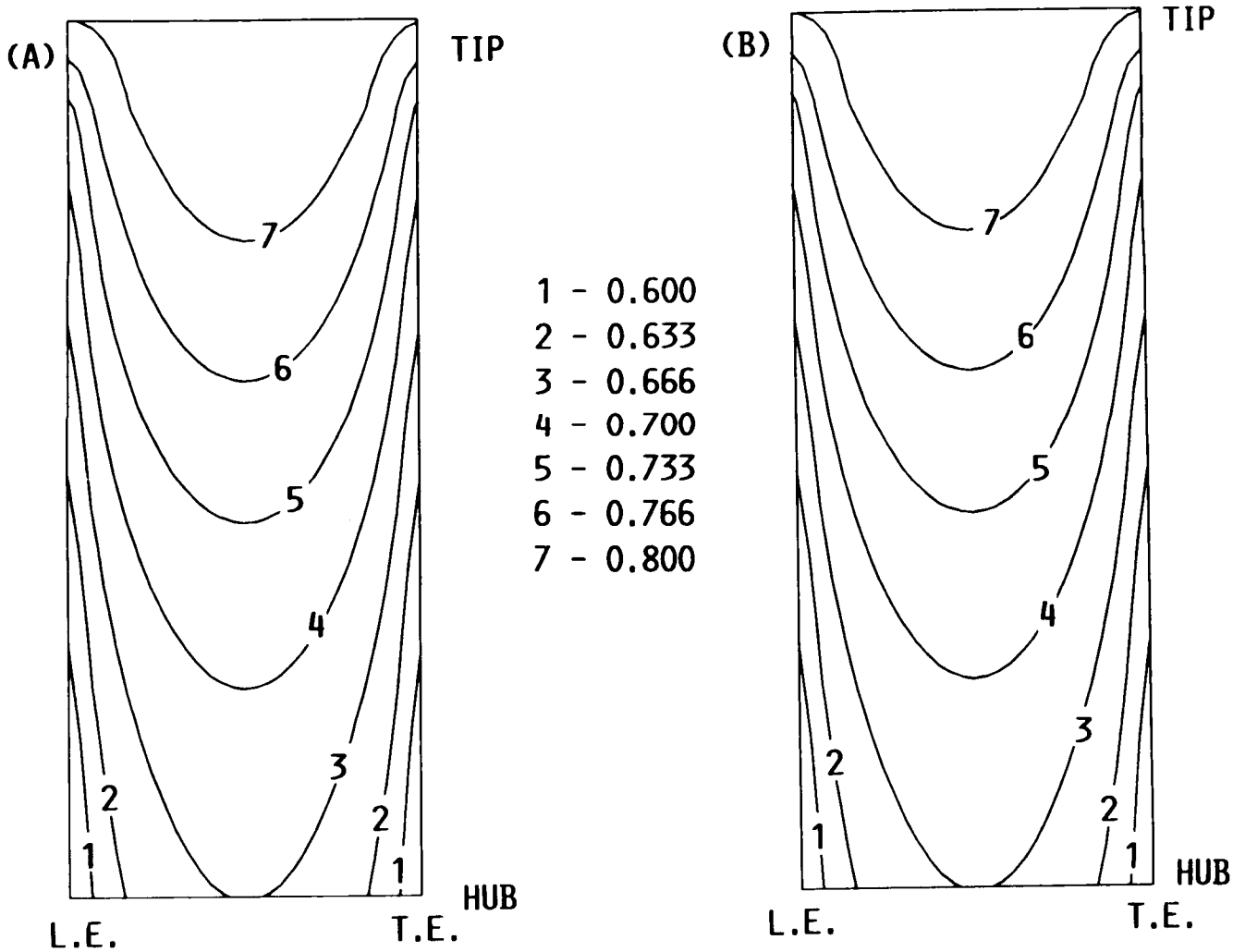

(A) PRESSURE SURFACE. (B) SUCTION SURFACE.

FIGURE 8.9. - MACH CONTOURS OF SMALL DISTURBANCE COMPUTATION ON BLADE SURFACES: ADVANCE RATIO = 1, M_R = 0.8, $\alpha = 0^o$.

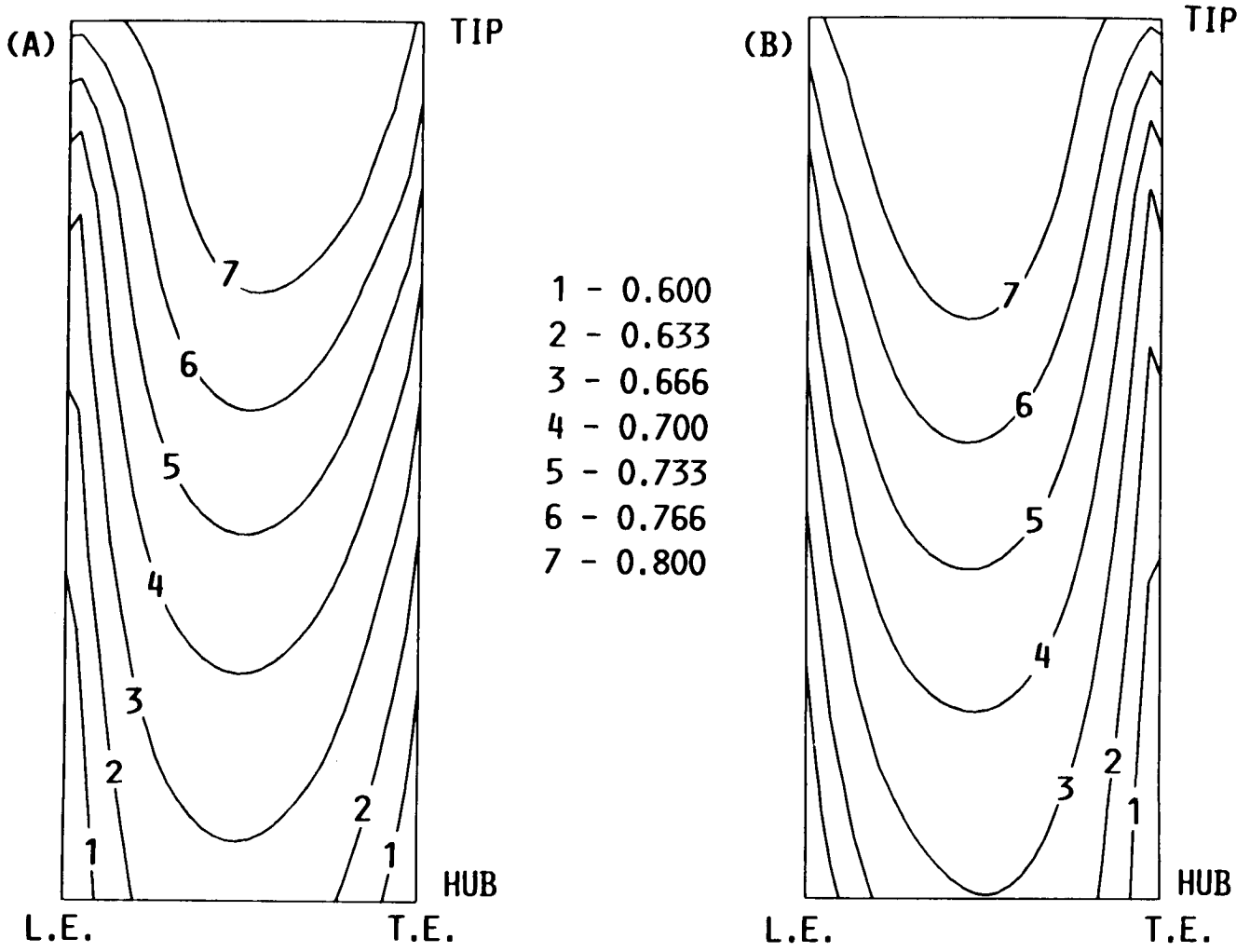

(A) PRESSURE SURFACE. (B) SUCTION SURFACE.

FIGURE 8.10. - MACH CONTOURS OF EULER COMPUTATION ON BLADE SURFACES: ADVANCE RATIO = 1, M_R = 0.8, $\alpha = 0^o$.

blade tip, the Euler contours are asymmetric with the pressure surface, being nearly the inverted image (left to right) as compared to the suction surface. This might be the result of blade stagger which would give an inverted image for a symmetric blade. For the case of isentropic flow, the Mach number on the pressure surface at a given chord location would be the same as that on the suction surface if its location was measured from the opposite end of the blade. To give an example, the maximum Mach number might occur at 60 percent chord, for a given span station, on the pressure surface; it would then have to occur at 40 percent chord on the suction surface. The reason for the observed difference in the magnitude between the pressure and suction contours for the Euler case is not known, but may, in part, be due to the grid asymmetry. While the results of the HSD contours are shown to be symmetric, there is no reason that the maximum Mach number must be at midchord.

The blade-to-blade contours for this case are shown in Figs. 8.11 and 8.12. The HSD results are given for the following range of Mach contours: 0.6 to 0.66 for Fig. 8.11(a); 0.66 to 0.71 for Fig. 8.11(b); and 0.75 to 0.78 for Fig. 8.11(c). The Euler results are presented for the same respective range of Mach contours. The primary difference between the two sets of contours is that the Euler computed contours more closely resemble contours about isolated blades. In the case of the HSD contours, they tend to shift upstream on the pressure side and downstream on the suction side of the blade so as to gradually join together at midchannel.

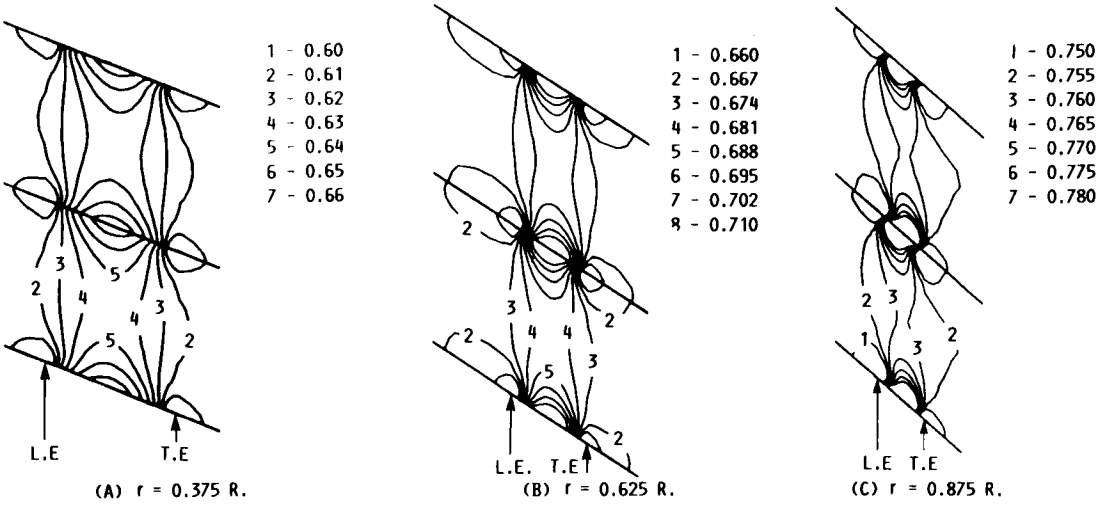

FIGURE 8.11. - MACH CONTOURS OF SMALL DISTURBANCE COMPUTATION ON BLADE-TO-BLADE SURFACES AT VARIOUS SPAN LOCATIONS: ADVANCE RATIO = 1, M_R = 0.8, $\alpha = 0^o$.

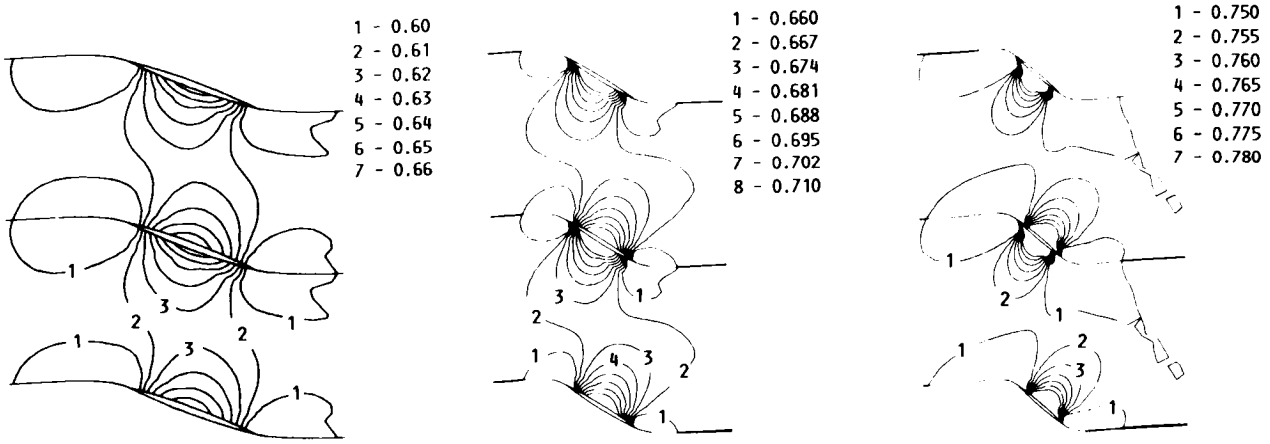

(A) r = 0.375 R. (B) r = 0.625 R. (C) r = 0.875 R.

FIGURE 8.12. - MACH CONTOURS OF EULER COMPUTATION ON BLADE-TO-BLADE SURFACES AT VARIOUS SPAN LOCATIONS: ADVANCE RATIO = 1, $M_R = 0.8$, $\alpha = 0^0$.

Case 3) $\lambda = 1$, $M_R = 1.1$, $\alpha = 0°$

This repeats the previous case, except that now the free-stream Mach number is increased so that it has a value of 0.7778 on the axis and a helical free-stream value of 1.1 at the blade tip. The Mach contours on the blade surface are given in Fig. 8.13 for the HSD computation. The contours are shifted toward the trailing edge on both the pressure and suction surfaces, which show identical contours. Near the tip and trailing edge a very weak shock may exist. In the case of the Euler computation, the rearward shift of peak Mach number is more pronounced. A weak shock probably exists on the suction surface where larger gradients than on the pressure side are indicated in Fig. 8.14.

The blade-to-blade contours for this case are shown in Fig. 8.15 for the HSD computation and in Fig. 8.16 for the Euler computation. For both sets of results, the contour Mach numbers range from: a) 0.82 to 1.0; b) 0.87 to 1.06, and c) 0.99 to 1.16. It is not clear that any shock exists for the HSD computation. However, a weak shock is observable in Fig. 8.16(c) of the Euler computation; it originates near the trailing edge of the suction surface and extends outward to a position upstream of the neighboring blade.

The HSD program was also used to obtain solutions for this test case for three additional grid densities. The grids differed from the standard grid in the number of grid intervals used in the three coordinate directions, whereas the locations of the upstream, downstream, and radial boundaries went unchanged. Also, the type of stretching was the same as for the standard grid. The number of grid intervals for each computational direction is presented in Table 8-3 for each of the three HSD refinement grids. These refinement grids are

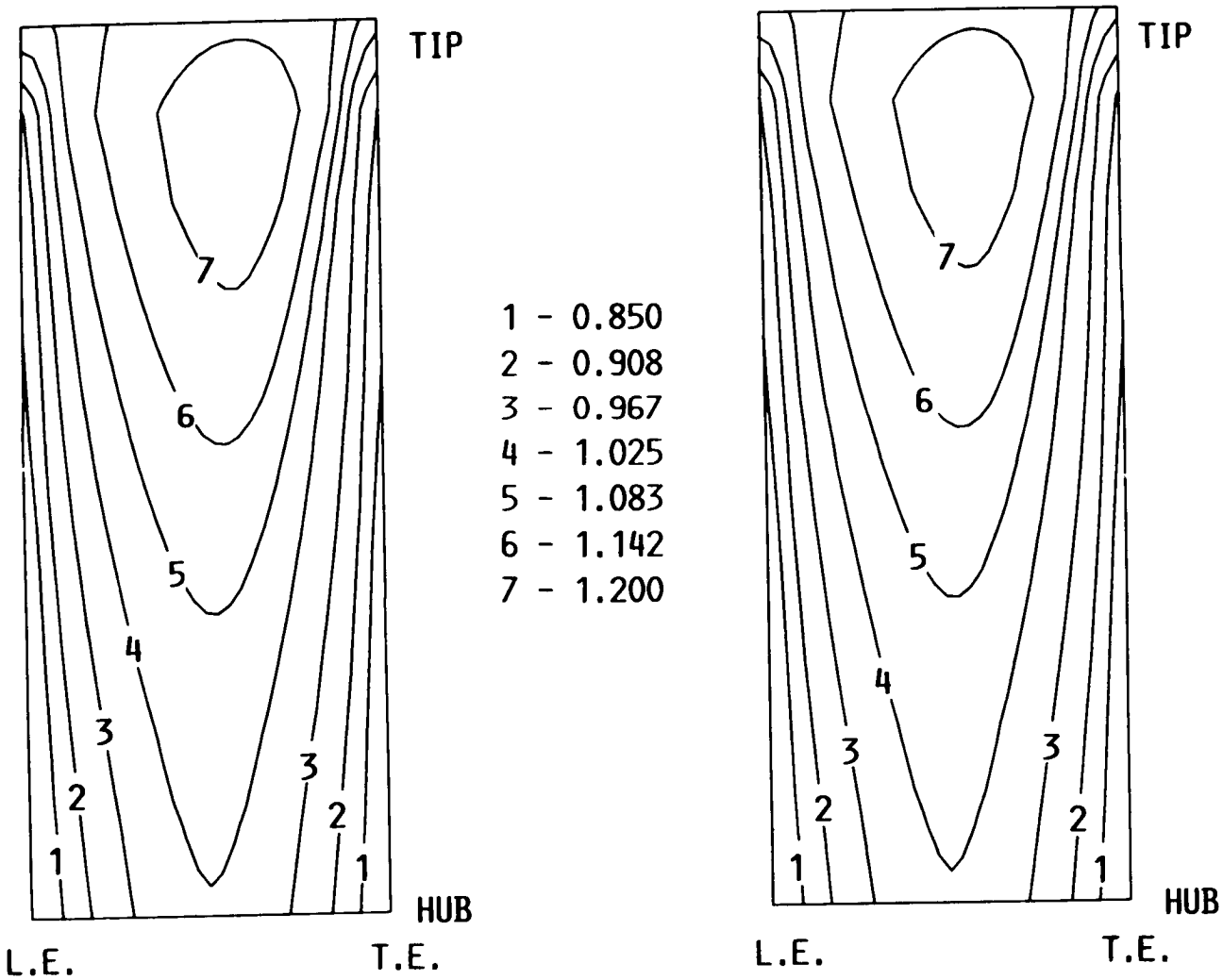

(A) PRESSURE SURFACE.

(B) SUCTION SURFACE.

FIGURE 8.13. - MACH CONTOURS OF SMALL DISTURBANCE COMPUTATION ON BLADE SURFACES: ADVANCE RATIO = 1, M_R = 1.1, $\alpha = 0^o$.

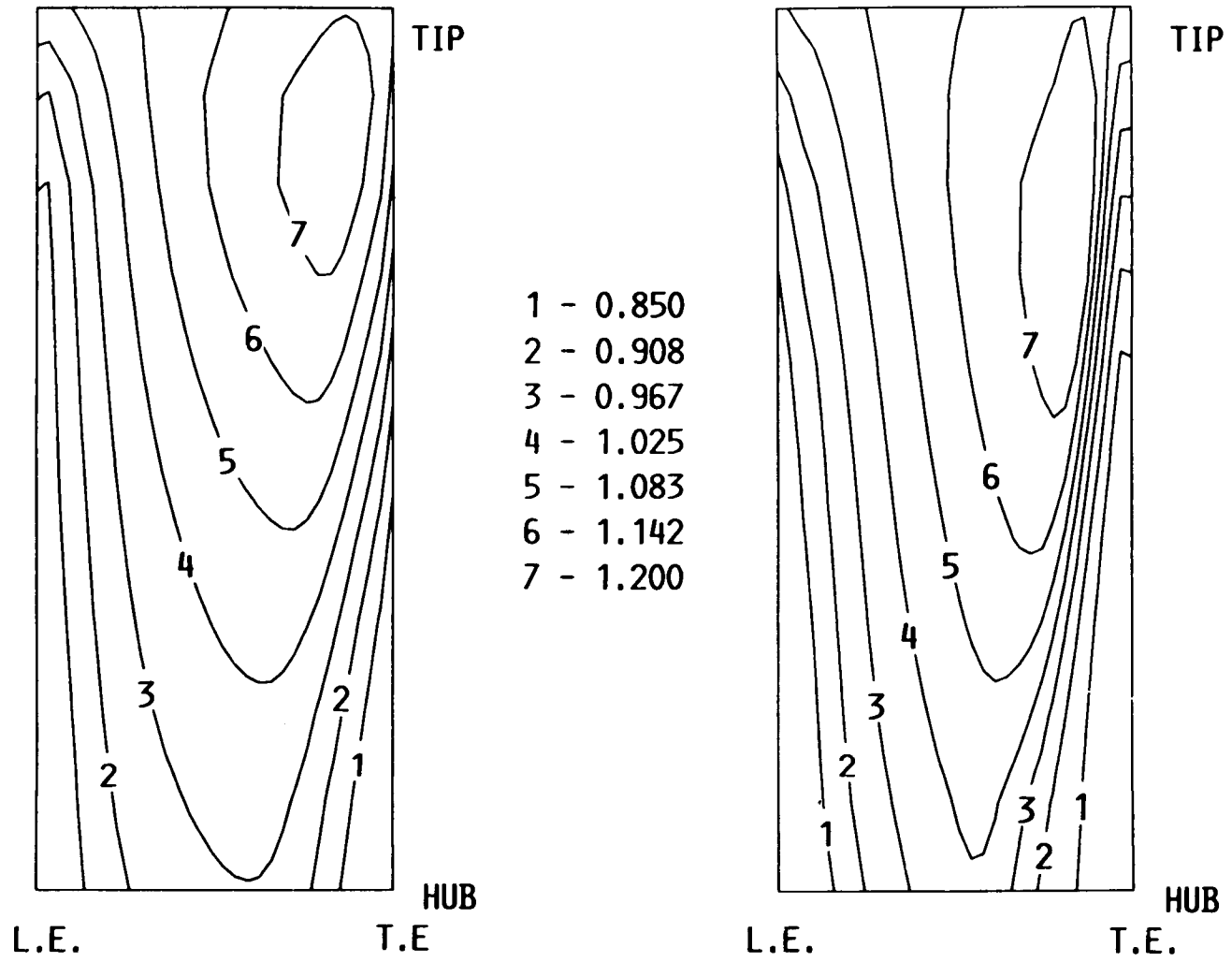

(A) PRESSURE SURFACE. (B) SUCTION SURFACE.

FIGURE 8.14. - MACH CONTOURS OF EULER COMPUTATION ON BLADE SURFACES: ADVANCE RATIO = 1, M_R = 1.1, $\alpha = 0^o$.

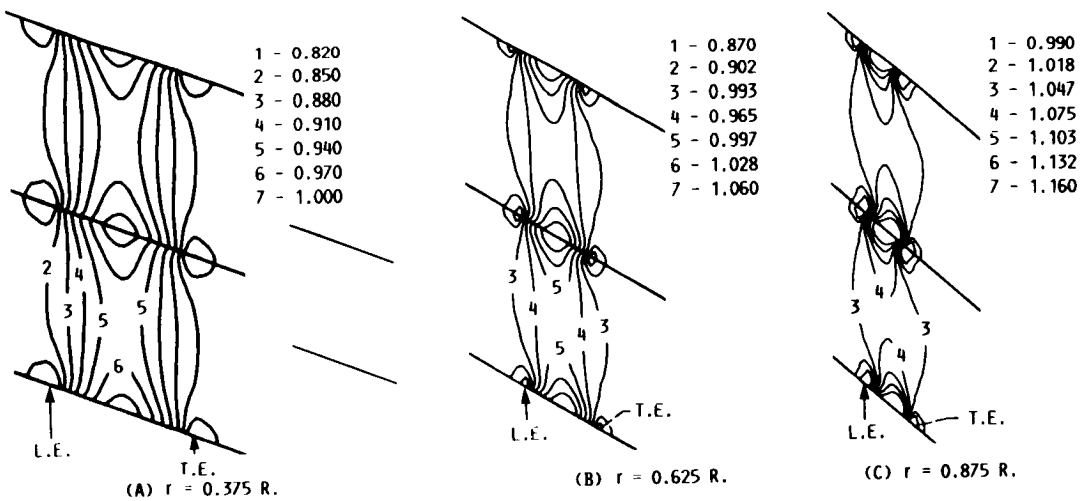

FIGURE 8.15. - MACH CONTOURS OF SMALL DISTURBANCE COMPUTATION ON BLADE-TO-BLADE SURFACES AT VARIOUS SPAN LOCATIONS: ADVANCE RATIO = 1, M_R = 1.1, $\alpha = 0^o$.

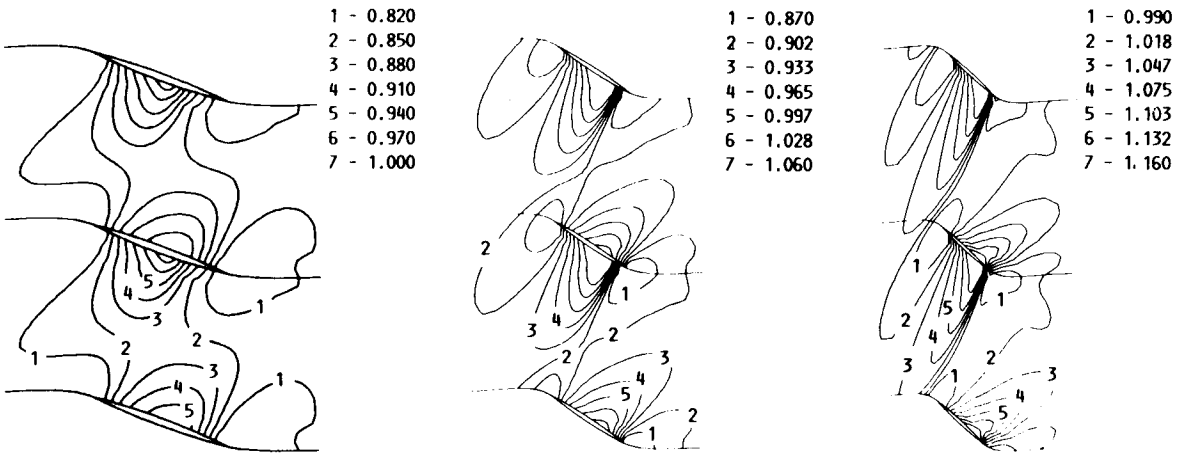

(A) r = 0.375 R. (B) r = 0.625 R. (C) r = 0.875 R.

FIGURE 8.16. - MACH CONTOURS OF EULER COMPUTATION ON BLADE-TO-BLADE SURFACES AT VARIOUS SPAN LOCATIONS: ADVANCE RATIO = 1, M_R = 1.1, $\alpha = 0^0$.

labeled coarse, medium, and fine, corresponding to their respective grid densities. For each of these additional grids, 6 grid intervals stretched from both the upstream boundary to the leading edge and from the trailing edge to the downstream boundary. Also, for each of these grids, 4 grid intervals stretched from the blade tip to the outer radial boundary. The variations among the grids were in the grid density used on the blade surface and the grid density used from blade to blade as follows: (1) the coarse grid contained 10 intervals from the leading edge of the blade to the trailing edge of the blade, 3 intervals from the hub to the blade tip, and 10 intervals from blade to blade; (2) the medium grid contained 20 intervals from the leading edge of the blade to the trailing edge of the blade, 6 intervals from the hub to the blade tip, and 20 intervals from blade to blade, and (3) the fine grid contained 30 intervals from the leading edge of the blade to the trailing edge of the blade, 12 intervals from the hub to the blade tip, and 40 intervals from blade to blade.

Some solution results obtained using the refinement grids are provided in Figs. 8.17(a) to (c) where constant Mach number contours on the pressure surface of the blade are presented for the coarse, medium, and fine grids, respectively. These results are compared with the corresponding results presented earlier in Fig. 8.13(a) for the same range of Mach number contour levels as were obtained using the standard grid. In general, the contour patterns obtained for each of the three refinement grids are similar to the contour pattern for the standard grid. The highest Mach number contour is absent from the results shown in Fig. 8.17(a) since this level exceeds the maximum value computed for the coarse grid density. There are two effects of grid refinement to

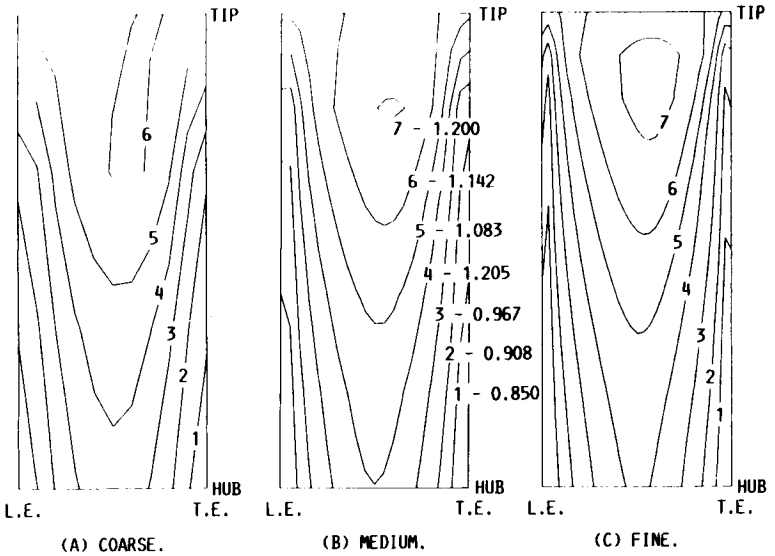

(A) COARSE. (B) MEDIUM. (C) FINE.

FIGURE 8.17. - MACH CONTOURS OF SMALL DISTURBANCE COMPUTATION ON PRESSURE SURFACE OF BLADE USING REFINEMENT GRIDS: ADVANCE RATIO = 1, M_R = 1.1, $\alpha = 0^o$.

be noted: (1) an increase in grid density results in a greater range of Mach numbers being obtained, and (2) an increase in grid density produces a more nearly symmetric contour pattern. Further refinements of the grid were made by increasing the density of the standard grid in each of the three coordinate directions, but only one direction at a time. Contour plots are not presented for these additional grid refinement results, but it is noted that they agreed closely with the contours provided in Fig. 8.13(a) for the standard grid. Based on these additional results and the fact that the contours of the fine grid refinement solution, presented in Fig. 8.17(c), agree closely with the contours for the standard grid solution, the refinement study indicated that the standard grid density is sufficient for most comparison purposes.

To provide information on the convergence properties and the computational requirements of the HSD code, the following data are included for the three grid refinement cases: (1) the overall reduction in the average solution residual; (2) the amount of computational time, and (3) the size of allocated computer memory. After computing 5000 iterations on each grid, the following was found: (1) the average residual decreased by 7 orders of magnitude using the coarse grid, 3.5 orders using the medium grid, and 2 orders using the fine grid; (2) the computational time required was 43 sec using the coarse grid, 204 sec using the medium grid, and 3204 sec using the fine grid, and (3) the memory allocated was 175,000 words for the coarse grid solution, 203,000 words for the medium grid solution, and 330,000 words for the fine grid solution.

Case 4) $\lambda = 1$, $M_R = 1.1$, $\alpha = 2°$

As a final case, the HSD code was used to recalculate the previous case except that a spanwise uniform angle of attack of 2° was used. The Euler code was not used for this case. The Mach contour plots are given in Fig. 8.18 for the blade surfaces and in Fig. 8.19 for the blade-to-blade surfaces. The effect of imposing an angle of attack on the blades resulted in a difference between the pressure and suction contours in the expected direction, i.e., the fluid velocity is now higher on the suction side. The blade-to-blade contours reveal that the flow is accelerated to a greater degree on the suction side. Although a weak shock may exist on either surface, no shock is noted to extend into the fluid from either surface of the blade.

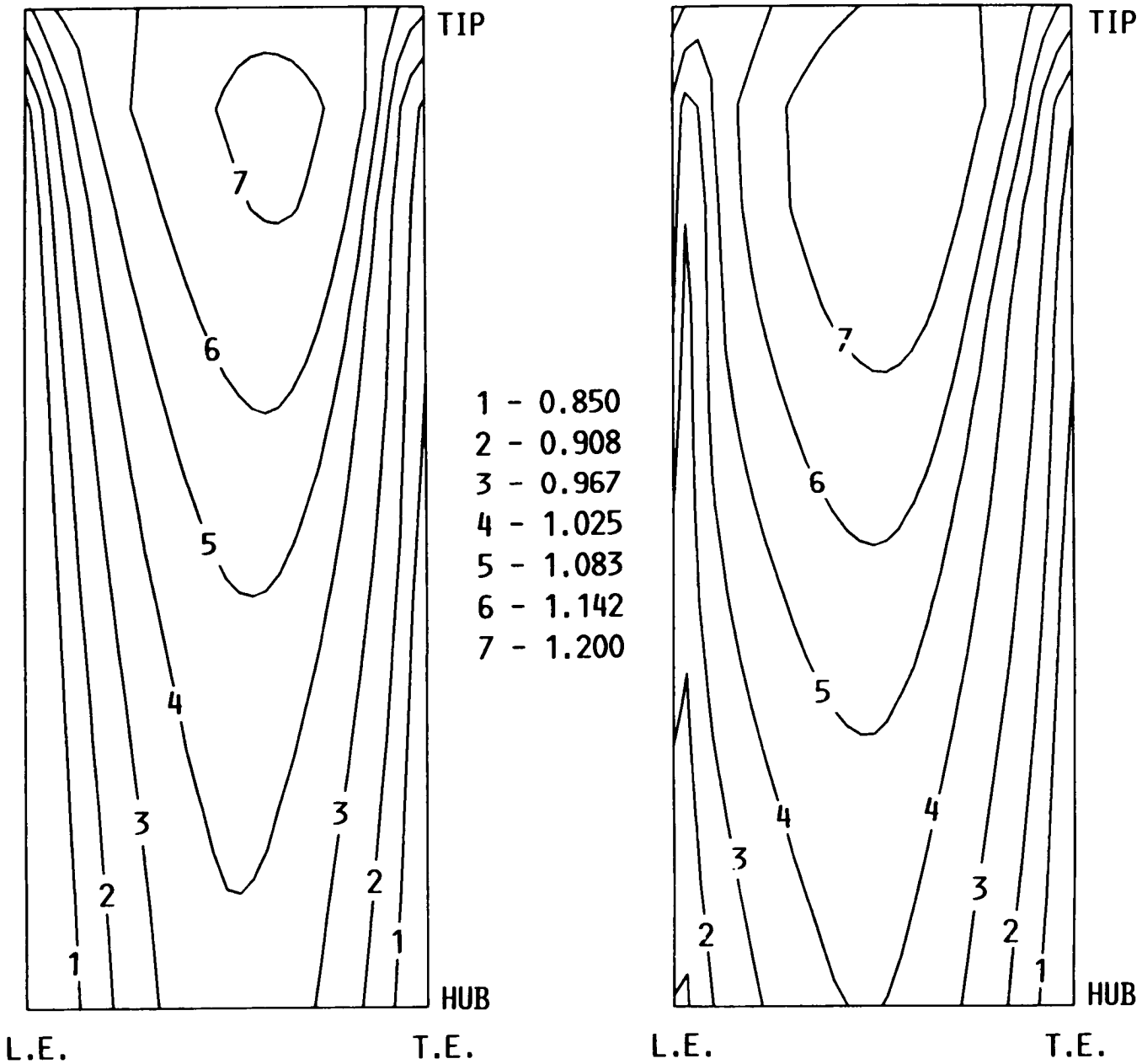

(A) PRESSURE SURFACE. (B) SUCTION SURFACE.

FIGURE 8-18. - MACH CONTOURS OF SMALL DISTURBANCE COMPUTATION ON BLADE SURFACES: ADVANCE RATIO = 1, M_R = 1.1, $\alpha = 2^o$.

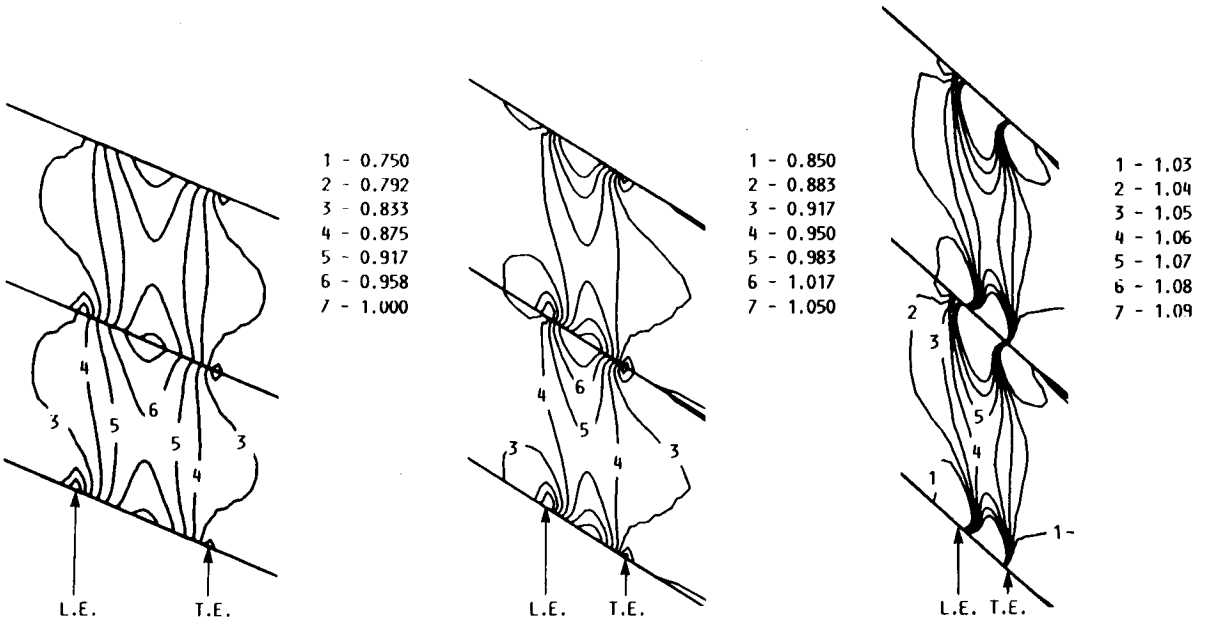

FIGURE 8.19. - MACH CONTOURS OF SMALL DISTURBANCE COMPUTATION ON BLADE-TO-BLADE SURFACES AT VARIOUS SPAN LOCATIONS: ADVANCE RATIO = 1, M_R = 1.1, $\alpha = 2^0$.

TABLE 8-1. - OPERATING PARAMETERS FOR THE FOUR PROPELLER TEST CASES

Case	λ	M_R	α
1	100	0.8	0.0
2	1	0.8	0.0
3	1	1.1	0.0
4	1	1.1	2.0

TABLE 8-2. - NUMBER OF GRID INTERVALS IN EACH MESH REGION FOR THE HSD-SOLUTION STANDARD GRID AND BOTH EULER SOLUTION GRIDS

	Streamwise or axial direction			Radial direction		Circumferential direction
	Upstream boundary to leading edge	Leading edge to trailing edge	Trailing edge to downstream boundary	Hub to blade tip	Blade tip to outer radial boundary	Blade to blade
Standard HSD-solution grid	11	30	11	10	10	20
Euler solution grid for λ = 100	14	30	14	10	10	20
Euler solution grid for λ = 1	15	30	16	10	10	20

TABLE 8-3. - NUMBER OF GRID INTERVALS IN EACH MESH REGION FOR THE HSD-SOLUTION REFINEMENT GRIDS

	Streamwise direction			Radial direction		Circumferential direction
	Upstream boundary to leading edge	Leading edge to trailing edge	Trailing edge to downstream boundary	Hub to blade tip	Blade tip to outer radial boundary	Blade to blade
Coarse HSD-solution grid	6	10	6	3	4	10
Medium HSD-solution grid	6	20	6	6	4	20
Fine HSD-solution grid	6	30	6	12	4	40

IX. CONCLUDING REMARKS

In this thesis the flow over a propeller has been investigated. This investigation involved the following main elements: (1) using a potential formulation, the general tensor form of the equation governing the unsteady, inviscid, irrotational, and isentropic flow over a propeller in a noninertial, blade-fixed coordinate system was developed; (2) based on a coordinate system which is aligned with the undisturbed free-stream helical flow, a disturbance equation of equivalent accuracy to the general tensor equation was established in which the unknown is the perturbation potential, measured by its variation from the free-stream potential; (3) a systematic simplification of the perturbation equation was made, based on the scaling parameters characteristic of an advanced turboprop, thus leading to the establishment of a low-frequency, small disturbance equation for an unsteady, approximate (or small) perturbation potential; (4) the corresponding boundary conditions for the approximate perturbation potential were derived for both the solid surface and the farfield boundaries; (5) a new periodic helical coordinate system was introduced which provided for the straightforward treatment of the blade-surface boundary conditions and, also, the treatment of periodic boundary conditions for a cascade; (6) an ADI scheme, previously used to solve for flow about a helicopter rotor tip using Cartesian coordinates, was extended to include the capability of solving the propeller equation when more than one cross derivative term is retained; (7) a computer program, which was structured directly from

the program used to calculate the solution to the unsteady disturbance equation for flow over a helicopter rotor tip, was made which solved the unsteady small disturbance equation for propeller flow using helical coordinates; (8) steady-state solutions were calculated using the computer program developed here for four distinct propeller test cases, which included both subsonic and transonic free-stream helical flow, and (9) the results obtained for the four steady test cases were discussed and compared with corresponding results from an Euler solution program.

The test cases presented in the last chapter were chosen because they serve as good prototypes for initial propeller studies. By inspection of the results obtained above, by either solution program, the flow of each case appears to lie within the range of computing capability of a small disturbance approach. In particular, no strong shocks were detected, nor did the computed flow depart by more than an acceptable extent from the free-stream state. Thus, for these studies, the flows appear to lie within the solution range governed, not only by the more complete Euler equations, but by the small disturbance equation as well.

In regard to the above remarks, it is emphasized that an obvious goal in undertaking this investigation was to determine if a small disturbance approach, in the manner applied here, could be used to solve for the steady flow over lightly loaded propeller blades operating in the transonic regime. This goal was accomplished and illustrated for a number of test cases. Another central goal was to provide an estimate on the validity of the solutions obtained. Lacking exact solutions, an Euler solution code was used to provide comparison solutions for each of the test cases. The results of the test cases presented in Chapter VIII

indicate that, although both the helical small disturbance solution program and the Euler solution program provide reasonable solutions, enough differences exist between the two codes to warrant further investigation. These additional investigations should be conducted toward the purpose of verifying each of the programs, as neither can be considered as providing the exact solution. In particular, the difference occurring between the results of the two solution programs in the magnitude of the constant Mach number contours for case 1 should be resolved. Similarly, the difference between the results of the two programs for the blade-to-blade contours needs to be explained. Some of the differences may be attributed to the absence of a common mesh.

As noted in Chapter VIII, the individual meshes used in these calculations were coarse. The density of the mesh was limited by the memory capacity of the computer. This limitation in capacity impacted the Euler program directly, since it required several times the memory capacity of the small disturbance program; the mesh density used in the small disturbance program was essentially set to match that used in the Euler program. Nevertheless, the grid refinement results obtained for the small disturbance solution of case 3 indicate that the grid density was reasonable, with the conclusion that further refinement of the grid was not going to result in large changes in the distribution of the Mach number contours. In addition to the mesh coarseness, other variations in mesh characteristics existed between the two codes. Some of the computational differences between the two codes might have been resolved if a common mesh had been used. As a final remark concerning solution verification, it is often the case that the verification of a solution is the most difficult step and one that is dependent on the existence

of solutions from other programs. In the case of the propeller, the capability to solve the flow is only now emerging, and hence the verification process will certainly be an ongoing one. It is hoped that the flow cases presented here will serve as test cases for other efforts.

A few comments will now be made concerning the potential value of the small disturbance computer program. In its present form, the program is capable of solving flow about lightly loaded blades, where the flow is steady in a blade-fixed coordinate system. However, the governing equation developed and presented in Chapter IV is for an unsteady flow. The decision to study only steady flow cases in this investigation was made not because of a particular limitation in the method, but because the steady flow problem was deemed sufficiently important and difficult to be treated separately. The relative value of the small perturbation method, as compared to methods based on equations valid for more general flows, such as the full potential equation or Euler equations, is greater for unsteady flow than for steady flow. The reason for this is that the computational resources, both in the memory capacity and speed of the computer, required to solve an unsteady flow are much greater than the resources required for the solution of a steady flow. Clearly, the reduction in computational expense offered by a small disturbance approach in comparison to, say an Euler equation approach, will be compounded when the use of either computer storage or computer time is increased.

As an example of a practical circumstance that illustrates the additional resources needed for solving an unsteady flow, the restrictions on the time step is an obvious case in point. The time

step must be restricted to a degree which allows the unsteady phenomena to be resolved; this is a significant limitation, and one which is often further complicated by the existence of fundamental time scales of widely differing magnitude. The minimum time step, corresponding to the smallest time scale required to resolve the flow, essentially determines the overall expenditure of computer time.

As another example which illustrates the additional demands made on computer resources in the case of an unsteady problem, the computational mesh size is mentioned. For most steady problems involving a farfield boundary surrounding a body, the computational mesh is stretched, so as to produce a grid having larger intervals away from the body than near it. This is especially typical with respect to transonic flow problems, where the decay of perturbations traveling lateral to the flow is extremely small, and consequently, the farfield is often placed 100 body lengths away. With a distant placement of farfield boundaries, a stretched grid is highly desirable, as it offers a significant reduction in mesh points in comparison to an unstretched grid; the magnitude of the grid stretching, of course, affects the solution accuracy. However, when using a stretched grid for computing an unsteady flow, additional errors, beyond those encountered for steady flow, are introduced. An example of the cause of such errors is the inaccuracy that occurs in the replication of an outgoing wave when it travels through a grid which is stretched. Near the body where the grid is finely spaced, the characteristics of the wave may be well represented; away from the body, where the grid is coarse, the wave may be distorted, both in magnitude and frequency. Furthermore, the resulting distorted wave may be reflected back toward the body,

whereupon, after further distortion occurring on its return path, it later reaches the body, but with a different wavelength and a different magnitude than it would have had if a uniform grid had been used.

Additional concerns, beyond the time-step and mesh size limitations, arise in the case of unsteady flow, and include the proper treatment of an aerodynamic body displaced from its equilibrium position due the action of fluid forces. Many of these concerns may be adequately addressed by adopting a perturbation approach. The example of the restriction on mesh size discussed above illustrates the advantages of a perturbation approach of the type used in the present investigation. For the same grid density, a small disturbance approach will require only a small fraction of the amount of computer memory as, say an Euler solution approach. With a given amount of computer memory, a finer grid, stretched or unstretched, can be used with the small disturbance approach in comparison with the same type of grid used for the Euler code. Furthermore, a small disturbance approach is computationally more efficient with respect to computer time, in general, than methods solving the more general equations. Since, as was discussed above, the unsteady flow case requires a greater number of mesh points, the computational savings of an efficient code is compounded above the savings realized for steady flow calculations because the computational time required to complete a solution iteration increases in proportion to the total number of mesh points. In view of the above remarks, and considering current computer capabilities, the small disturbance approach presents a viable method of solving both steady and unsteady propeller flow.

Based on this conclusion, a few suggestions are made regarding possible future investigations of propeller flow using the helical small disturbance approach. These suggestions include methods of improving on the above investigation and also possible extensions to the scope of the investigation. As a first step, test-case comparisons similar to those studied here should be computed using a common mesh. As a means of providing a common mesh, a more general helical coordinate system than the one presented in this thesis has already been developed. This newer helical coordinate system conforms to the exact blade shape, rather than the mean chord position. This means that the small disturbance boundary conditions can be replaced by actual blade surface boundary conditions. The new coordinate system is suitable for other inviscid flow solvers, and thus provides a common mesh upon which comparison solutions could be computed. Additional studies could also be made investigating the effect of using the exact blade boundary, rather than the mean chord position, as the location for the blade surface boundary condition. For unsteady flow which may involve blade flutter, the equilibrium position of the blade may be used in place of the exact location of the blade, if the blade deflection is small. In this way, the small disturbance approach to the treatment of the blade boundary condition can be accurately extended to unsteady flow. These are some of the possible areas which may be examined in future studies. Should any additional work along these lines be undertaken, the approach chosen should be as simple as reasonable accuracy allows.

APPENDIX A - HELICAL COORDINATE TRANSFORMATION FOR A CASCADE

In this section, the metric tensor components are derived and the Jacobian is determined for a general transformation between orthogonal Cartesian coordinates x^i and helical coordinates y^j. The Cartesian coordinates will be given as functions of the helical coordinates which is expressed formally by

$$x^i = x^i(y^j) \qquad i,j = 1,2,3. \tag{A1}$$

Both x^i and y^j are right-handed triplets. To avoid carrying along the superscript notation, the following assignments are made

$$x^1 = x,\ x^2 = y,\ x^3 = z \tag{A2}$$

for the Cartesian coordinates and

$$y^1 = \gamma,\ y^2 = r,\ y^3 = \xi \tag{A3}$$

for the helical coordinates. The transformation of coordinates is then defined through

$$x = x(\gamma,r,\xi) = r \sin \vartheta \tag{A4}$$

$$y = y(\gamma,r,\xi) = r \cos \vartheta \tag{A5}$$

$$z = z(\gamma,r,\xi) = -\gamma \frac{V}{U} + A(r)B(\xi) \tag{A6}$$

where

$$\vartheta = \frac{\Omega\gamma}{U} + \frac{\xi}{R} \tag{A7}$$

and is measured from the y-axis as is shown in Fig. (6-2). The total or helical velocity U and the axial velocity V are each functions of r and are connected by the rotational velocity Ω through the Pythagorean relation given by

$$U = U(r) = \left[(\Omega r)^2 + V^2(r)\right]^{1/2} \tag{A8}$$

The significance of the functions $A(r)$ and $B(\xi)$ and their actual forms were considered in Chapter V. Here they are assumed to be reasonable functions of r and ξ respectively.

By defining

$$U' = \frac{dU}{dr}\,, \quad V' = \frac{dV}{dr}\,, \quad A' = \frac{dA}{dr}\,, \quad \text{and} \quad B' = \frac{dB}{d\xi}\,, \tag{A9}$$

the individual partial derivatives of the Cartesian coordinates, which will be needed, can be expressed as

$$\frac{\partial x^1}{\partial y^1} \equiv \frac{\partial x}{\partial \gamma} = \frac{\Omega r}{U} \cos \vartheta \tag{A10}$$

$$\frac{\partial x^1}{\partial y^2} \equiv \frac{\partial x}{\partial r} = \sin \vartheta + r \frac{\partial \vartheta}{\partial r} \cos \vartheta \tag{A11}$$

$$\frac{\partial x^1}{\partial y^3} \equiv \frac{\partial x}{\partial \xi} = \frac{r}{R} \cos \vartheta \tag{A12}$$

$$\frac{\partial x^2}{\partial y^1} \equiv \frac{\partial y}{\partial \gamma} = -\frac{\Omega r}{U} \sin \vartheta \tag{A13}$$

$$\frac{\partial x^2}{\partial y^2} \equiv \frac{\partial y}{\partial r} = \cos \vartheta - r \frac{\partial \vartheta}{\partial r} \sin \vartheta \tag{A14}$$

$$\frac{\partial x^2}{\partial y^3} \equiv \frac{\partial y}{\partial \xi} = -\frac{r}{R} \sin \vartheta \tag{A15}$$

$$\frac{\partial x^3}{\partial y^1} \equiv \frac{\partial z}{\partial \gamma} = -\frac{V}{U} \tag{A16}$$

$$\frac{\partial x^3}{\partial y^2} \equiv \frac{\partial z}{\partial r} = \left(\frac{V}{U^2} U' - \frac{V'}{U}\right)\gamma + A'B \tag{A17}$$

$$\frac{\partial x^3}{\partial y^3} \equiv \frac{\partial z}{\partial \xi} = AB'. \tag{A18}$$

A necessary and sufficient condition for the transformation relations to be independent is that the Jacobian J of the transformation, namely

$$J = \left|\frac{\partial x^i}{\partial y^j}\right| \equiv \begin{vmatrix} \frac{\partial x^1}{\partial y^1} & \frac{\partial x^1}{\partial y^2} & \frac{\partial x^1}{\partial y^3} \\ \frac{\partial x^2}{\partial y^1} & \frac{\partial x^2}{\partial y^2} & \frac{\partial x^2}{\partial y^3} \\ \frac{\partial x^3}{\partial y^1} & \frac{\partial x^3}{\partial y^2} & \frac{\partial x^3}{\partial y^3} \end{vmatrix}, \tag{A19}$$

be nonzero. The partial derivatives given by equations (A10) through (A18) can be used to evaluate J; which is expressed in mixed form to reduce the algebra, as

$$J = \begin{vmatrix} \frac{\Omega r}{U}\cos\vartheta & \sin\vartheta + r\frac{\partial\vartheta}{\partial r}\cos\vartheta & \frac{r}{R}\cos\vartheta \\ -\frac{\Omega r}{U}\sin\vartheta & \cos\vartheta - r\frac{\partial\vartheta}{\partial r}\sin\vartheta & -\frac{r}{R}\sin\vartheta \\ -\frac{V}{U} & \frac{\partial z}{\partial r} & \frac{\partial z}{\partial \xi} \end{vmatrix}. \tag{A20}$$

Expanding the determinant produces the following:

$$J = \frac{\Omega r}{U}\frac{\partial z}{\partial \xi}\left(\cos^2\vartheta - r\frac{\partial\vartheta}{\partial r}\cos\vartheta\sin\vartheta\right) + \frac{V}{U}\frac{r}{R}\left(\sin^2\vartheta + r\frac{\partial\vartheta}{\partial r}\cos\vartheta\sin\vartheta\right)$$
$$+ \frac{\Omega r}{U}\frac{\partial z}{\partial \xi}\left(\sin^2\vartheta + r\frac{\partial\vartheta}{\partial r}\cos\vartheta\sin\vartheta\right) + \frac{V}{U}\frac{r}{R}\left(\cos^2\vartheta - r\frac{\partial\vartheta}{\partial r}\cos\vartheta\sin\vartheta\right)$$
$$- \frac{r}{R}\frac{\Omega r}{U}\frac{\partial z}{\partial r}\cos\vartheta\sin\vartheta + \frac{r}{R}\frac{\Omega r}{U}\frac{\partial z}{\partial r}\cos\vartheta\sin\vartheta = \frac{V}{U}\frac{r}{R} + \frac{\Omega r}{U}\frac{\partial z}{\partial \xi}. \tag{A21}$$

From this, the transformation is seen to be valid in the domain where $J \neq 0$, i.e.,

$$\frac{\partial z}{\partial \xi} \neq -\frac{V}{\Omega R} \equiv -\lambda. \tag{A22}$$

The covariant metric tensor components g_{ij} can be determined using

$$g_{ij} = \frac{\partial x^m}{\partial y^i}\frac{\partial x^m}{\partial y^j}, \tag{A23}$$

This will be used to find each of the six distinct g_{ij}. First, to find g_{11} the following three terms are easily developed:

$$\frac{\partial x^1}{\partial y^1}\frac{\partial x^1}{\partial y^1} \equiv \left(\frac{\partial x}{\partial \gamma}\right)^2 = \left(\frac{\Omega r}{U}\right)^2 \cos^2\vartheta$$

$$\frac{\partial x^2}{\partial y^1}\frac{\partial x^2}{\partial y^1} \equiv \left(\frac{\partial y}{\partial \gamma}\right)^2 = \left(\frac{\Omega r}{U}\right)^2 \sin^2\vartheta$$

$$\frac{\partial x^3}{\partial y^1}\frac{\partial x^3}{\partial y^1} \equiv \left(\frac{\partial z}{\partial \gamma}\right)^2 = \left(\frac{V}{U}\right)^2.$$

Adding the three terms as prescribed by Eq. (A23) gives

$$g_{11} = \left(\frac{\Omega r}{U}\right)^2 + \left(\frac{V}{U}\right)^2 = 1, \tag{A24}$$

which follows from Eq. (A28). Similarly, the terms for g_{22} are

$$\frac{\partial x^1}{\partial y^2}\frac{\partial x^1}{\partial y^2} \equiv \left(\frac{\partial x}{\partial r}\right)^2 = \sin^2\vartheta + 2r\frac{\partial \vartheta}{\partial r}\cos\vartheta\sin\vartheta + r^2\left(\frac{\partial \vartheta}{\partial r}\right)^2\cos^2\vartheta$$

$$\frac{\partial x^2}{\partial y^2}\frac{\partial x^2}{\partial y^2} \equiv \left(\frac{\partial y}{\partial r}\right)^2 = \cos^2\vartheta - 2r\frac{\partial \vartheta}{\partial r}\cos\vartheta\sin\vartheta + r^2\left(\frac{\partial \vartheta}{\partial r}\right)^2\sin^2\vartheta$$

$$\frac{\partial x^3}{\partial y^2}\frac{\partial x^3}{\partial y^2} \equiv \left(\frac{\partial z}{\partial r}\right)^2 = \left[\left(\frac{V}{U^2}U' - \frac{V'}{U}\right)\gamma + A'B\right]^2$$

and, thus

$$g_{22} = 1 + r^2\left(\frac{\partial \vartheta}{\partial r}\right)^2 + \left(\frac{\partial z}{\partial r}\right)^2 \tag{A25}$$

For g_{33}

$$\frac{\partial x^1}{\partial y^3}\frac{\partial x^1}{\partial y^3} \equiv \left(\frac{\partial x}{\partial \xi}\right)^2 = \left(\frac{r}{R}\right)^2 \cos^2 \vartheta$$

$$\frac{\partial x^2}{\partial y^3}\frac{\partial x^2}{\partial y^3} \equiv \left(\frac{\partial y}{\partial \xi}\right)^2 = \left(\frac{r}{R}\right)^2 \sin^2 \vartheta$$

$$\frac{\partial x^3}{\partial y^3}\frac{\partial x^3}{\partial y^3} \equiv \left(\frac{\partial z}{\partial \xi}\right)^2 = (AB')^2$$

and, thus

$$g_{33} = \left(\frac{r}{R}\right)^2 + \left(\frac{\partial z}{\partial \xi}\right)^2. \tag{A26}$$

For g_{12}

$$\frac{\partial x^1}{\partial y^1}\frac{\partial x^1}{\partial y^2} \equiv \frac{\partial x}{\partial \gamma}\frac{\partial x}{\partial r} = \frac{\Omega r}{U}\cos \vartheta \sin \vartheta + \frac{\Omega r}{U} r \frac{\partial \vartheta}{\partial r}\cos^2 \vartheta$$

$$\frac{\partial x^2}{\partial y^1}\frac{\partial x^2}{\partial y^2} \equiv \frac{\partial y}{\partial \gamma}\frac{\partial y}{\partial r} = -\frac{\Omega r}{U}\cos \vartheta \sin \vartheta + \frac{\Omega r}{U} r \frac{\partial \vartheta}{\partial r}\sin^2 \vartheta$$

$$\frac{\partial x^3}{\partial y^1}\frac{\partial x^3}{\partial y^2} \equiv \frac{\partial z}{\partial \gamma}\frac{\partial z}{\partial r} = -\frac{V}{U}\left[-\frac{\gamma}{U}\left(V' - \frac{V}{U}U'\right) + A'B\right]$$

and, thus

$$g_{12} = \frac{\Omega r}{U} r \frac{\partial \vartheta}{\partial r} - \frac{V}{U}\frac{\partial z}{\partial r}. \tag{A27}$$

For g_{13}

$$\frac{\partial x^1}{\partial y^1}\frac{\partial x^1}{\partial y^3} \equiv \frac{\partial x}{\partial \gamma}\frac{\partial x}{\partial \xi} = \frac{\Omega r}{U}\frac{r}{R}\cos^2 \vartheta$$

$$\frac{\partial x^2}{\partial y^1}\frac{\partial x^2}{\partial y^3} \equiv \frac{\partial y}{\partial \gamma}\frac{\partial y}{\partial \xi} = \frac{\Omega r}{U}\frac{r}{R}\sin^2 \vartheta$$

$$\frac{\partial x^3}{\partial y^1}\frac{\partial x^3}{\partial y^3} \equiv \frac{\partial z}{\partial \gamma}\frac{\partial z}{\partial \xi} = -\frac{V}{U}AB'$$

and, thus

$$g_{13} = \frac{\Omega r}{U}\,\frac{r}{R} - \frac{V}{U}\,AB'. \tag{A28}$$

For g_{23}

$$\frac{\partial x^1}{\partial y^2}\,\frac{\partial x^1}{\partial y^3} \equiv \frac{\partial x}{\partial r}\,\frac{\partial x}{\partial \xi} = \frac{r}{R}\cos\vartheta\,\sin\vartheta + \frac{r}{R}\,r\,\frac{\partial \vartheta}{\partial r}\cos^2\vartheta$$

$$\frac{\partial x^2}{\partial y^2}\,\frac{\partial x^2}{\partial y^3} \equiv \frac{\partial y}{\partial r}\,\frac{\partial y}{\partial \xi} = -\frac{r}{R}\cos\vartheta\,\sin\vartheta + \frac{r}{R}\,r\,\frac{\partial \vartheta}{\partial r}\sin^2\vartheta$$

$$\frac{\partial x^3}{\partial y^2}\,\frac{\partial x^3}{\partial y^3} \equiv \frac{\partial z}{\partial r}\,\frac{\partial z}{\partial \xi} = \left[\left(\frac{V}{U^2}\,U' - \frac{V'}{U}\right)\gamma + A'B\right]AB'$$

and, thus

$$g_{23} = \frac{r}{R}\,r\,\frac{\partial \vartheta}{\partial r} + \frac{\partial z}{\partial r}\,\frac{\partial z}{\partial \xi} \tag{A29}$$

or

$$g_{23} = -\frac{\Omega r}{U}\,\frac{r}{R}\,\frac{U'\gamma}{U} + \left[\left(\frac{V}{U^2}\,U' - \frac{V'}{U}\right)\gamma + A'B\right]AB'. \tag{A30}$$

We can collect g_{11}, g_{22}, g_{33}, g_{12}, g_{13}, and g_{23} into the matrix

$$g_{ij} = \begin{bmatrix} 1 & \dfrac{\Omega r}{U}\,r\,\dfrac{\partial \vartheta}{\partial r} - \dfrac{V}{U}\,\dfrac{\partial z}{\partial r} & \dfrac{\Omega r}{U}\,\dfrac{r}{R} - \dfrac{V}{U}\,\dfrac{\partial z}{\partial \xi} \\ \dfrac{\Omega r}{U}\,r\,\dfrac{\partial \vartheta}{\partial r} - \dfrac{V}{U}\,\dfrac{\partial z}{\partial r} & 1 + r^2\left(\dfrac{\partial \vartheta}{\partial r}\right)^2 + \left(\dfrac{\partial z}{\partial r}\right)^2 & \dfrac{r}{R}\,r\,\dfrac{\partial \vartheta}{\partial r} + \dfrac{\partial z}{\partial r}\,\dfrac{\partial z}{\partial \xi} \\ \dfrac{\Omega r}{U}\,\dfrac{r}{R} - \dfrac{V}{U}\,\dfrac{\partial z}{\partial \xi} & \dfrac{r}{R}\,r\,\dfrac{\partial \vartheta}{\partial r} + \dfrac{\partial z}{\partial r}\,\dfrac{\partial z}{\partial \xi} & \left(\dfrac{r}{R}\right)^2 + \left(\dfrac{\partial z}{\partial \xi}\right)^2 \end{bmatrix} \tag{A31}$$

The Det g_{ij} can be readily calculated. To simplify the notation, let

$$\alpha = \frac{\partial z}{\partial r}\,, \quad \beta = \frac{\partial z}{\partial \xi}\,, \quad \text{and} \quad \eta = r\,\frac{\partial \vartheta}{\partial r} \tag{A32}$$

where α, β, and η are used only for convenience and are independent of their use elsewhere in the text. The determinant of g_{ij}, when expanded, gives

$$\text{Det } g_{ij} = \left[1 + \eta^2 + \alpha^2 - \left(\frac{\Omega r}{U}\right)^2 \eta^2 + 2\,\frac{V}{U}\,\frac{\Omega r}{U}\,\eta\alpha - \left(\frac{V}{U}\right)^2 \alpha^2\right]\left[\left(\frac{r}{R}\right)^2 + \beta^2\right]$$

$$- \left[1 + \eta^2 + \alpha^2\right]\left[\left(\frac{\Omega r}{U}\right)^2 \left(\frac{r}{R}\right)^2 - 2\,\frac{\Omega r}{U}\,\frac{r}{R}\,\frac{V}{U}\,\beta + \left(\frac{V}{U}\right)^2 \beta^2\right]$$

$$+ 2\left(\frac{\Omega r}{U}\,\eta - \frac{V}{U}\,\alpha\right)\left(\frac{r}{R}\,\eta + \alpha\beta\right)\left(\frac{\Omega r}{U}\,\frac{r}{R} - \frac{V}{U}\,\beta\right)$$

$$- \left(\frac{r}{R}\right)^2 \eta^2 - 2\,\frac{r}{R}\,\eta\alpha\beta - \alpha^2\beta^2. \qquad \text{(A33)}$$

Further expansion and use of the identity

$$\left(\frac{\Omega r}{U}\right)^2 + \left(\frac{V}{U}\right)^2 = 1 \qquad \text{(A34)}$$

yields

$$\text{Det } g_{ij} = \left(\frac{r}{R}\right)^2 + \left(\frac{r}{R}\right)^2 \left(\frac{V}{U}\right)^2 \eta^2 + \left(\frac{r}{R}\right)^2 \left(\frac{\Omega r}{U}\right)^2 \alpha^2 + 2\left(\frac{r}{R}\right)^2 \frac{V}{U}\,\frac{\Omega r}{U}\,\eta\alpha + \beta^2$$

$$+ \left(\frac{V}{U}\right)^2 \eta^2\beta^2 + \left(\frac{\Omega r}{U}\right)^2 \alpha^2\beta^2 + 2\,\frac{V}{U}\,\frac{\Omega r}{U}\,\alpha\eta\beta^2 - \left(\frac{\Omega r}{U}\right)^2 \left(\frac{r}{R}\right)^2 + 2\,\frac{\Omega r}{U}\,\frac{r}{R}\,\frac{V}{U}\,\beta$$

$$- \left(\frac{V}{U}\right)^2 \beta^2 - \left(\frac{\Omega r}{U}\right)^2 \left(\frac{r}{R}\right)^2 \eta^2 + 2\,\frac{\Omega r}{U}\,\frac{r}{R}\,\frac{V}{U}\,\eta^2\beta - \left(\frac{V}{U}\right)^2 \eta^2\beta^2 - \left(\frac{\Omega r}{U}\right)^2 \left(\frac{r}{R}\right)^2 \alpha^2$$

$$+ 2\,\frac{\Omega r}{U}\,\frac{r}{R}\,\frac{V}{U}\,\alpha^2\beta - \left(\frac{V}{U}\right)^2 \alpha^2\beta^2 + 2\left(\frac{r}{R}\right)^2 \left(\frac{\Omega r}{U}\right)^2 \eta^2 - 2\,\frac{r}{R}\,\frac{V}{U}\,\frac{\Omega r}{U}\,\eta^2\beta$$

$$+ 2\,\frac{r}{R}\left(\frac{\Omega r}{U}\right)^2 \eta\alpha\beta - 2\,\frac{\Omega r}{U}\,\frac{V}{U}\,\eta\alpha\beta^2 - 2\left(\frac{r}{R}\right)^2 \frac{\Omega r}{U}\,\frac{V}{U}\,\eta\alpha - 2\,\frac{r}{R}\,\frac{V}{U}\,\frac{\Omega r}{U}\,\alpha^2\beta$$

$$+ 2\,\frac{r}{R}\left(\frac{V}{U}\right)^2 \eta\alpha\beta + 2\left(\frac{V}{U}\right)^2 \alpha^2\beta^2 - \left(\frac{r}{R}\right)^2 \eta^2 - 2\,\frac{r}{R}\,\eta\alpha\beta - \alpha^2\beta^2. \qquad \text{(A35)}$$

Cancellation reduces Eq. (A35) to the following form

$$\text{Det } g_{ij} = \left(\frac{r}{R}\right)^2 \left(\frac{V}{U}\right)^2 + 2\,\frac{\Omega r}{U}\,\frac{r}{R}\,\frac{V}{U}\,\beta + \left(\frac{\Omega r}{U}\right)^2 \beta^2 \qquad \text{(A36)}$$

or

$$g = \text{Det } g_{ij} = \left(\frac{r}{R}\,\frac{V}{U} + \frac{\Omega r}{U}\,\frac{\partial z}{\partial \xi}\right)^2. \qquad \text{(A37)}$$

Comparison of this result with Eq. (A21) shows that

$$J = (g)^{1/2}, \tag{A38}$$

exactly as it must.

The contravariant metric tensors g^{ij} can be calculated from g_{ij} and g using the general relation

$$g^{ij} = \frac{G^{ij}}{g}, \tag{A39}$$

where G^{ij} are the corresponding minors of the determinant g. The g^{ij} are determined as follows:

$$g^{11} = \frac{1}{g}\left(g_{22}g_{33} - g_{23}^2\right)$$

$$g^{11} = \frac{1}{g}\left\{\left[1 + \eta^2 + \alpha^2\right]\left[\left(\frac{r}{R}\right)^2 + \beta^2\right] - \left[\frac{r}{R}\,\eta + \alpha\beta\right]^2\right\}$$

$$= \frac{1}{g}\left[\left(\frac{r}{R}\right)^2 + \beta^2 + \eta^2\beta^2 + \left(\frac{r}{R}\right)^2\alpha^2 - 2\,\frac{r}{R}\,\eta\alpha\beta\right]$$

therefore,

$$g^{11} = \frac{1}{g}\left[\left(\frac{r}{R}\right)^2 + \beta^2 + \left(\frac{r}{R}\,\alpha - \eta\beta\right)^2\right]. \tag{A40}$$

$$g^{22} = \frac{1}{g}\left(g_{11}g_{33} - g_{13}^2\right)$$

$$= \frac{1}{g}\left[\left(\frac{r}{R}\right)^2 + \beta^2 - \left(\frac{\Omega r}{U}\,\frac{r}{R} - \frac{V}{U}\,\beta\right)^2\right]$$

$$= \frac{1}{g}\left[\left(\frac{r}{R}\right)^2\left(\frac{V}{U}\right)^2 + 2\,\frac{\Omega r}{U}\,\frac{r}{R}\,\frac{V}{U}\,\beta + \left(\frac{\Omega r}{U}\right)^2\beta^2\right]$$

therefore,

$$g^{22} = \frac{1}{g}\left(\frac{r}{R}\,\frac{V}{U} + \frac{\Omega r}{U}\,\beta\right)^2 = 1. \tag{A41}$$

$$g^{33} = \frac{1}{g}\left(g_{11}g_{22} - g_{12}^2\right)$$

$$= \frac{1}{g}\left[1 + \eta^2 + \alpha^2 - \left(\frac{\Omega r}{U}\,\eta - \frac{V}{U}\,\alpha\right)^2\right]$$

$$= \frac{1}{g}\left[1 + \left(\frac{V}{U}\right)^2 \eta^2 + 2\,\frac{\Omega r}{U}\,\frac{V}{U}\,\eta\alpha + \left(\frac{\Omega r}{U}\right)^2 \alpha^2\right]$$

therefore,

$$g^{33} = \frac{1}{g}\left[1 + \left(\frac{V}{U}\,\eta + \frac{\Omega r}{U}\,\alpha\right)^2\right]. \tag{A42}$$

$$g^{12} = -\frac{1}{g}\,(g_{21}g_{33} - g_{31}g_{23})$$

$$= -\frac{1}{g}\left\{\left(\frac{\Omega r}{U}\,\eta - \frac{V}{U}\,\alpha\right)\left[\left(\frac{r}{R}\right)^2 + \beta^2\right] - \left(\frac{\Omega r}{U}\,\frac{r}{R} - \frac{V}{U}\,\beta\right)\left(\frac{r}{R}\,\eta + \alpha\beta\right)\right\}$$

$$= -\frac{1}{g}\left\{\left[\frac{r}{R}\,\frac{V}{U} + \frac{\Omega r}{U}\,\beta\right]\eta\beta - \frac{r}{R}\left[\frac{r}{R}\,\frac{V}{U} + \frac{\Omega r}{U}\,\beta\right]\alpha\right\}$$

$$= -\frac{1}{g}\left(\frac{r}{R}\,\frac{V}{U} + \frac{\Omega r}{U}\,\beta\right)\left(\eta\beta - \frac{r}{R}\,\alpha\right)$$

therefore,

$$g^{12} = \frac{1}{\sqrt{g}}\left(\frac{r}{R}\,\alpha - \eta\beta\right). \tag{A43}$$

$$g^{13} = \frac{1}{g}\,(g_{21}g_{32} - g_{31}g_{22})$$

$$g^{13} = \frac{1}{g}\left[\left(\frac{\Omega r}{U}\,\eta - \frac{V}{U}\,\alpha\right)\left(\frac{r}{R}\,\eta + \alpha\beta\right) - \left(\frac{\Omega r}{U}\,\frac{r}{R} - \frac{V}{U}\,\beta\right)\left(1 + \eta^2 + \alpha^2\right)\right]. \tag{A44}$$

Finally

$$g^{23} = -\frac{1}{g}\,(g_{11}g_{32} - g_{31}g_{12})$$

$$g^{23} = -\frac{1}{g}\left[\frac{r}{R}\,\eta + \alpha\beta - \left(\frac{\Omega r}{U}\,\frac{r}{R} - \frac{V}{U}\,\beta\right)\left(\frac{\Omega r}{U}\,\eta - \frac{V}{U}\,\alpha\right)\right]$$

$$= -\frac{1}{g}\left\{\left(\frac{V}{U}\right)^2 \frac{r}{R}\,\eta + \frac{\Omega r}{U}\,\frac{V}{U}\,\frac{r}{R}\,\alpha + \beta\left[\frac{\Omega r}{U}\,\frac{V}{U}\,\eta + \left(\frac{\Omega r}{U}\right)^2 \alpha\right]\right\}$$

$$= -\frac{1}{g}\left(\frac{r}{R}\,\frac{V}{U} + \frac{\Omega r}{U}\,\beta\right)\left(\frac{V}{U}\,\eta + \frac{\Omega r}{U}\,\alpha\right)$$

therefore,

$$g^{23} = -\frac{1}{\sqrt{g}}\left(\frac{V}{U}\,\eta + \frac{\Omega r}{U}\,\alpha\right). \tag{A45}$$

The g^{ij} can be expressed in the symmetric matrix form similar to Eq. (A31) as

$$g^{ij} = \begin{bmatrix} \frac{1}{g}\left[\left(\frac{r}{R}\right)^2 + \beta^2 + \left(\frac{r}{R}\alpha - \eta\beta\right)^2\right] & \frac{1}{\sqrt{g}}\left(\frac{r}{R}\alpha - \eta\beta\right) & \frac{1}{g}\left[\left(\frac{\Omega r}{U}\eta - \frac{V}{U}\alpha\right)\left(\frac{r}{R}\eta + \alpha\beta\right) - \left(\frac{\Omega r}{U}\frac{r}{R} - \frac{V}{U}\beta\right)\left(1 + \eta^2 + \beta^2\right)\right] \\ g^{12} & 1 & -\frac{1}{\sqrt{g}}\left(\frac{V}{U}\eta + \frac{\Omega r}{U}\alpha\right) \\ g^{13} & g^{23} & \frac{1}{g}\left[1 + \left(\frac{V}{U}\eta + \frac{\Omega r}{U}\alpha\right)^2\right] \end{bmatrix}. \tag{A46}$$

Expanding the determinant of the above matrix for the contravariant metric tensor components provides a check of the algebra and gives

$$\begin{aligned} \text{Det } g^{ij} = \frac{1}{g^2}\Bigg\{ & \left[\left(\frac{r}{R}\right)^2 + \beta^2 + \left(\frac{r}{R}\alpha - \eta\beta\right)^2\right]\left[1 + \left(\frac{V}{U}\eta + \frac{\Omega r}{U}\alpha\right)^2\right] \\ & - \left[\left(\frac{r}{R}\right)^2 + \beta^2 + \left(\frac{r}{R}\alpha - \eta\beta\right)^2\right]\left(\frac{V}{U}\eta + \frac{\Omega r}{U}\alpha\right)^2 - 2\left(\frac{r}{R}\alpha - \eta\beta\right)\left(\frac{V}{U}\eta + \frac{\Omega r}{U}\alpha\right) \\ & \times \left[\left(\frac{\Omega r}{U}\eta - \frac{V}{U}\alpha\right)\left(\frac{r}{R}\eta + \alpha\beta\right) - \left(\frac{\Omega r}{U}\frac{r}{R} - \frac{V}{U}\beta\right)\left(1 + \eta^2 + \alpha^2\right)\right] \\ & - \left[\left(\frac{\Omega r}{U}\eta - \frac{V}{U}\alpha\right)\left(\frac{r}{R}\eta + \alpha\beta\right) - \left(\frac{\Omega r}{U}\frac{r}{R} - \frac{V}{U}\beta\right)\left(1 + \eta^2 + \alpha^2\right)\right]^2 \\ & - \left(\frac{r}{R}\alpha - \eta\beta\right)^2\left[1 + \left(\frac{V}{U}\eta + \frac{\Omega r}{U}\alpha\right)^2\right]\Bigg\}. \end{aligned}$$

This simplifies to the following form after cancellation of some of the terms

$$\begin{aligned} \text{Det } g^{ij} = \frac{1}{g^2}\Bigg\{ & \left(\frac{r}{R}\right)^2 + \beta^2 - \left[\left(\eta\beta - \frac{r}{R}\alpha\right)\left(\frac{V}{U}\eta + \frac{\Omega r}{U}\alpha\right)\right. \\ & \left. - \left(\frac{\Omega r}{U}\eta - \frac{V}{U}\alpha\right)\left(\frac{r}{R}\eta + \alpha\beta\right) + \left(\frac{\Omega r}{U}\frac{r}{R} - \frac{V}{U}\beta\right)\left(1 + \eta^2 + \alpha^2\right)\right]^2\Bigg\}. \end{aligned}$$

In turn, this expression can be expanded to give

$$\text{Det } g^{ij} = \frac{1}{g^2}\left[\left(\frac{r}{R}\right)^2 + \beta^2 - \left(\frac{V}{U}\beta\eta^2 + \frac{\Omega r}{U}\eta\alpha\beta - \frac{r}{R}\frac{V}{U}\eta\alpha - \frac{\Omega r}{U}\frac{r}{R}\alpha^2 - \frac{\Omega r}{U}\frac{r}{R}\eta^2 - \frac{\Omega r}{U}\eta\alpha\beta + \frac{r}{R}\frac{V}{U}\eta\alpha + \frac{V}{U}\alpha^2\beta + \frac{\Omega r}{U}\frac{r}{R} - \frac{V}{U}\beta + \frac{\Omega r}{U}\frac{r}{R}\eta^2 - \frac{V}{U}\eta^2\beta + \frac{\Omega r}{U}\frac{r}{R}\alpha^2 - \frac{V}{U}\alpha^2\beta\right)^2\right].$$

More cancellation brings

$$\text{Det } g^{ij} = \frac{1}{g^2}\left[\left(\frac{r}{R}\right)^2 + \beta^2 - \left(\frac{\Omega r}{U}\right)^2\left(\frac{r}{R}\right)^2 + 2\frac{\Omega r}{U}\frac{r}{R}\frac{V}{U}\beta - \left(\frac{V}{U}\right)^2\beta^2\right].$$

Using the identity given in Eq. (A34), leads to

$$\text{Det } g^{ij} = \frac{1}{g^2}\left[\left(\frac{r}{R}\frac{V}{U}\right)^2 + 2\frac{\Omega r}{U}\frac{r}{R}\frac{V}{U}\beta + \left(\frac{\Omega r}{U}\right)^2\beta^2\right].$$

Using Eq. (A37), we finally have

$$\text{Det } g^{ij} = \frac{1}{g^2}\left[\frac{r}{R}\frac{V}{U} + \frac{\Omega r}{U}\beta\right]^2 = \frac{g}{g^2} = \frac{1}{g}. \qquad \text{(A47)}$$

Special Cases of Coordinates

Two special cases are now given. In the first case, for $A = 0$ in Eq. (A6) and with V equal to a constant, we have the case where ξ is a purely circumferential direction and

$$g_{ij} = \begin{bmatrix} 1 & -\frac{\Omega^2\gamma r}{U^2} & \frac{\Omega r^2}{RU} \\ g_{12} & 1 + \left(\frac{\Omega r}{U}\right)^2\left(\frac{\Omega\gamma}{U}\right)^2 & -\left(\frac{\Omega r}{U}\right)^3\frac{\gamma}{R} \\ g_{13} & g_{23} & \left(\frac{r}{R}\right)^2 \end{bmatrix} \qquad \text{(A48)}$$

and,

$$g^{ij} = \begin{bmatrix} \left(\frac{U}{V}\right)^2 + \left(\frac{\Omega\gamma}{U}\right)^2 \left(\frac{\Omega r}{U}\right)^2 & \frac{\Omega^2 \gamma r}{U^2} & -\frac{U}{V}\frac{\Omega R}{V} \\ g^{12} & 1 & 0 \\ g^{13} & 0 & \left(\frac{U}{V}\right)^2 \left(\frac{R}{r}\right)^2 \end{bmatrix}. \qquad \text{(A49)}$$

In this case $J = (r/R)(V/U)$.

In the second case, again, V is a constant, here, however, $A = (\Omega R/V)(r/R)^2$ and $B = \xi$. This produces a coordinate system where the ξ curves are helices with the arc length inversely proportional to r. The metric tensor components are

$$g_{ij} = \begin{bmatrix} 1 & -\frac{\Omega r}{U}\left(\frac{\Omega\gamma}{U} + 2\frac{\xi}{R}\right) & 0 \\ g_{12} & 1 + \left(\frac{\Omega r}{U}\right)^2 \left(\frac{\Omega\gamma}{U}\right)^2 + 4\left(\frac{\Omega r}{U}\right)^2 \frac{\Omega\gamma}{U}\frac{\xi}{R} + \left(2\frac{\Omega R}{V}\frac{r}{R}\frac{\xi}{R}\right)^2 & 2\left(\frac{\Omega R}{V}\right)^2 \left(\frac{r}{R}\right)^3 \frac{\xi}{R} \\ 0 & g_{23} & \left(\frac{r}{R}\right)^2 \left[1 + \left(\frac{\Omega R}{V}\right)^2 \left(\frac{r}{R}\right)^2\right] \end{bmatrix} \qquad \text{(A50)}$$

and,

$$\begin{bmatrix} 1 + \left(\frac{\Omega r}{U}\right)^2 \left(\frac{\Omega\gamma}{U} + 2\frac{\xi}{R}\right)^2 & \frac{\Omega r}{U}\left(\frac{\Omega\gamma}{U} + 2\frac{\xi}{R}\right) & g^{31} \\ g^{12} & 1 & 2\left(\frac{\Omega R}{V}\right)^2 \left(\frac{r}{R}\right)^3 \frac{\xi}{R} \\ -2\left(\frac{\Omega R}{U}\right)^3 \left(\frac{r}{R}\right)^2 \frac{\xi}{R} \times \left(\frac{\Omega\gamma}{U} + 2\frac{\xi}{R}\right) & g^{23} & \left(\frac{VR}{Ur}\right)^2 + 4\left(\frac{\Omega R}{U}\right)^4 \left(\frac{r\xi}{R^2}\right)^2 \end{bmatrix}. \qquad \text{(A51)}$$

In this case $J = (r/R)(U/V)$.

APPENDIX B - HELICAL COORDINATE TRANSFORMATION FOR AN ISOLATED BLADE

The transformation is given here for the helical coordinates used for flow about an isolated blade with a tip radius R which is rotating with constant angular speed Ω and advancing at a constant axial speed V. The covariant metric tensor components g_{ij} and the contravariant components g^{ij} are also given for reference. Let x^1, x^2, x^3 be a right-handed orthogonal Cartesian coordinate system and y^1, y^2, y^3 be a right handed helical coordinate system as shown in Fig. (6.1). The transformation of the helical coordinates to the Cartesian coordinates is given by

$$x^1 = y^2 \sin \vartheta \tag{B1}$$

$$x^2 = y^2 \cos \vartheta \tag{B2}$$

$$x^3 = -\frac{V}{U} y^1 + \frac{\Omega}{U} y^2 y^3 \tag{B3}$$

where the angle ϑ is measured from the y^2-axis as shown in Fig. (6.1) and given by

$$\vartheta = \frac{\Omega}{U} y^1 + \frac{V}{U} \frac{y^3}{y^2} . \tag{B4}$$

Here, the total velocity U is given as

$$U = \left[(\Omega y^2)^2 + V^2 \right]^{1/2} \tag{B5}$$

The covariant metric tensor components g_{ij} are

$$g_{ij} = \begin{vmatrix} 1 & -\frac{\Omega y^2}{U}\left(\vartheta + \frac{Vy^3}{Uy^2}\right) & 0 \\ g_{12} & 1 + \left[\left(\frac{\Omega y^2}{U}\right)^2 \vartheta + \frac{Vy^3}{Uy^2}\right]^2 + \left(\frac{\Omega y^2}{U}\,\frac{V}{U}\,\vartheta\right)^2 & -\left(\frac{V}{U}\right)^2 \frac{y^3}{y^2} \\ 0 & g_{23} & 1 \end{vmatrix} \qquad \text{(B6)}$$

and the contravariant components are

$$g^{ij} = \begin{vmatrix} 1 + (g_{12})^2 & -g_{12} & g_{12}g_{23} \\ -g_{12} & 1 & -g_{23} \\ g_{12}g_{23} & -g_{23} & 1 + (g_{23})^2 \end{vmatrix}. \qquad \text{(B7)}$$

Since for these coordinates Det $g_{ij} \equiv g = 1$, then the Jacobian J of the transformation is unity, $J = 1$.

APPENDIX C - PARTIAL DERIVATIVES FOR COORDINATE STRETCHING

Given coordinates γ, r, ξ which are functions of the coordinates $\bar{\gamma},\bar{r},\bar{\xi}$ defined by

$$\gamma = \gamma(\bar{\gamma}, \bar{r}), \quad r = r(\bar{r}), \quad = \xi(\bar{\xi}), \tag{C1}$$

the following relationships between the partial derivatives are obtained:

$$\frac{\partial\varphi}{\partial\gamma} = \frac{\partial\varphi}{\partial\bar{\gamma}}\frac{\partial\bar{\gamma}}{\partial\gamma} \tag{C2}$$

$$\frac{\partial\varphi}{\partial r} = \frac{\partial\varphi}{\partial\bar{\gamma}}\frac{\partial\bar{\gamma}}{\partial r} + \frac{\partial\varphi}{\partial\bar{r}}\frac{\partial\bar{r}}{\partial r} \tag{C3}$$

$$\frac{\partial\varphi}{\partial\xi} = \frac{\partial\varphi}{\partial\bar{\xi}}\frac{\partial\bar{\xi}}{\partial\xi} \tag{C4}$$

$$\frac{\partial^2\varphi}{\partial\gamma^2} = \frac{\partial^2\varphi}{\partial\bar{\gamma}^2}\left(\frac{\partial\bar{\gamma}}{\partial\gamma}\right)^2 + \frac{\partial\varphi}{\partial\bar{\gamma}}\frac{\partial^2\bar{\gamma}}{\partial\gamma^2} \tag{C5}$$

$$\frac{\partial^2\varphi}{\partial r^2} = \frac{\partial^2\varphi}{\partial\bar{\gamma}^2}\left(\frac{\partial\bar{\gamma}}{\partial r}\right)^2 + 2\frac{\partial^2\varphi}{\partial\bar{\gamma}\partial\bar{r}}\frac{\partial\bar{\gamma}}{\partial r}\frac{\partial\bar{r}}{\partial r} + \frac{\partial\varphi}{\partial\bar{\gamma}}\frac{\partial^2\bar{\gamma}}{\partial r^2} + \frac{\partial^2\varphi}{\partial\bar{r}^2}\left(\frac{\partial\bar{r}}{\partial r}\right)^2 + \frac{\partial\varphi}{\partial\bar{r}}\frac{\partial^2\bar{r}}{\partial r^2} \tag{C6}$$

$$\frac{\partial^2\varphi}{\partial\xi^2} = \frac{\partial^2\varphi}{\partial\bar{\xi}^2}\left(\frac{\partial\bar{\xi}}{\partial\xi}\right)^2 + \frac{\partial\varphi}{\partial\bar{\xi}}\frac{\partial^2\bar{\xi}}{\partial\xi^2} \tag{C7}$$

$$\frac{\partial^2\varphi}{\partial\gamma\partial r} = \frac{\partial^2\varphi}{\partial\bar{\gamma}^2}\frac{\partial\bar{\gamma}}{\partial\gamma}\frac{\partial\bar{\gamma}}{\partial r} + \frac{\partial^2\varphi}{\partial\bar{\gamma}\partial\bar{r}}\frac{\partial\bar{\gamma}}{\partial\gamma}\frac{\partial\bar{r}}{\partial r} + \frac{\partial\varphi}{\partial\bar{\gamma}}\frac{\partial^2\bar{\gamma}}{\partial\gamma\partial r} \tag{C8}$$

$$\frac{\partial^2\varphi}{\partial\gamma\partial\xi} = \frac{\partial^2\varphi}{\partial\bar{\gamma}\partial\bar{\xi}}\frac{\partial\bar{\gamma}}{\partial\gamma}\frac{\partial\bar{\xi}}{\partial\xi} \tag{C9}$$

$$\frac{\partial^2\varphi}{\partial r\partial\xi} = \frac{\partial^2\varphi}{\partial\bar{r}\partial\bar{\xi}}\frac{\partial\bar{r}}{\partial r}\frac{\partial\bar{\xi}}{\partial\xi} + \frac{\partial^2\varphi}{\partial\bar{\gamma}\partial\bar{\xi}}\frac{\partial\bar{\gamma}}{\partial r}\frac{\partial\bar{\xi}}{\partial\xi}\,. \tag{C10}$$

REFERENCES

1. Caradonna, F.X.; and Philippe, J.J.: The Flow Over a Helicopter Blade Tip in the Transonic Regime. Vertica, vol. 2, no. 1, 1978, pp. 43-60.
2. Caradonna, F.X.; and Isom, M.P.: Subsonic and Transonic Potential Flow Over Helicopter Rotor Blades. AIAA J., vol. 10, no. 12, Dec. 1972, pp. 1606-1612.
3. Caradonna, F.X.; and Isom, M.P.: Numerical Calculation of Unsteady Transonic Potential Flow Over Helicopter Rotor Blades. AIAA J., vol. 14, no. 4, Apr. 1976, pp. 482-488.
4. Caradonna, F.X.: The Transonic Flow on a Helicopter Rotor. Ph.D. Thesis, Stanford University, 1978.
5. Isom, M.P.: Unsteady Subsonic and Transonic Potential Flow Over Helicopter Rotor Blades. NASA CR-2463, 1974.
6. Celestina, M.L.; Mulac, R.A.; and Adamcyck, J.J.: A Numerical Simulation of the Inviscid Flow Through a Counterrotating Propeller. J. Turbomachinery, vol. 108, no. 2, Oct. 1986, pp. 187-193.
7. Glauert, H.: The Elements of Aerofoil and Airscrew Theory. Cambridge University Press, 1947, Chapter 15-16.
8. Von Mises, R.: Theory of Flight. Dover Publications, New York, 1959, Part Three.
9. Betz, H.: Schraubenpropeller mit Geringsten Energieverlust. Nachr. Ges. Wiss. Goettingen Math. Phys. Kl., 1919.

10. Goldstein, S.: On the Vortex Theory of Screw Propellers. Proc. R. Soc. London A, vol. 123, no. 792, Apr. 6, 1929, pp. 440-465.

11. Reissner, H.: On the Relation Between Thrust and Torque Distribution and the Dimensions and the Arrangement of Propeller-Blades. Philos. Mag. Ser. 7, vol. 24, no. 163, Nov. 1937, pp. 745-771.

12. Reissner, H.: On the Vortex Theory of the Screw Propeller. J. Aeronaut. Sci., vol. 5, no. 1, Nov. 1937, pp. 1-7.

13. Reissner, H.: A Generalized Vortex Theory of the Screw Propeller and its Application. NACA TN-750, 1940.

14. Lamb, H.: The Magnetic Field of a Helix. Cambridge Phil. Soc. Proc., vol. 21, June 15, 1923, pp. 477-481.

15. Kawada, S.: Induced Velocity by Helical Vortices. J. Aeronaut. Sci., vol. 3, no. 3, Jan. 1936, pp. 86-87.

16. Theodorsen, T.: The Theory of Propellers, I - Determination of the Circulation Function and the Mass Coefficient for Dual-Rotating Propellers. NACA Rept-775, 1944.

17. Theodorsen, T.: The Theory of Propellers, II - Method for Calculating the Axial Interference Velocity. NACA Rept-776, 1944.

18. Theordorsen, T.: The Theory of Propellers, III - The Slipstream Contraction With Numerical Values for Two-Blade and Four-Blade Propellers. NACA Rept-777, 1944.

19. Theodorsen, T.: The Theory of Propellers, IV. - Thrust, Energy, and Efficiency Formulas for Single- and Dual-Rotating Propellers With Ideal Circulation Distribution. NACA Rept-778, 1944.

20. Theodorsen, T.: The Theory of Propellers. McGraw-Hill, 1948.

21. Busemann, A.: Theory of the Propeller in Compressible Flow. Proceedings of the Third Midwestern Conference on Fluid Mechanics, University of Minnesota, Minneapolis, MN, 1953, pp. 267-286.

22. Davidson, R.E.: Linearized Potential Theory of Propeller Induction in a Compressible Flow. NACA TN-2983, 1953.

23. Hanson, D.B.: Compressible Helicoidal Surface Theory for Propeller Aerodynamics and Noise. AIAA J., vol. 21, no. 6, June 1983, pp. 881-889.

24. Goldstein, M.E.: Aeroacoustics. McGraw-Hill, 1976.

25. Courant, R.; Friedrichs, K.O.; and Lewy, H.: Uber die Partiellen Differenzengleichungen der Mathematischen Physik. Math. Ann., vol. 100, 1928, p. 32.

26. Garabedian, P.R.: Partial Differential Equations. John Wiley & Sons, 1964.

27. Courant, R.; and Hilbert, D.: Methods of Mathematical Physics. Vol. I and II, Interscience Publishers, 1953, 1962.

28. Kevorkain, J.: First Order Partial Differential Equations. Handbook of Applied Mathematics, C.E. Pearson, ed., Van Nostrand Reinhold, 1974, Chapter 8.

29. Lax, P.D.: Hyperbolic Systems of Conservation Laws and the Mathematical Theory of Shock Waves. Society for Industrial and Applied Mathematics, 1973.

30. Klopher, G.H.; and Nixon, D.: Nonisentropic Potential Formulation for Transonic Flows. AIAA J., vol. 22, no. 6, June 1984, pp. 770-776.

31. Emmons, H.W.: Flow of a Compressible Fluid Past a Symmetrical Airfoil in a Wind Tunnel and in Free Air. NACA TN-1746, 1948.

32. Moretti, G.: The λ-scheme. Comput. Fluids, vol. 7, no. 3, Sept. 1979, pp. 191-205.

33. Zannetti, L.; and Colasurdo, G.: Unsteady Compressible Flow: A Computational Method Consistent With the Physical Phenomena. AIAA J., vol. 19, no. 7, July 1981, pp. 852-856.

34. von Neumann, J.; and Richtmyer, R.D.: A Method for the Numerical Calculation of Hydrodynamic Shocks. J. Appl. Phys., vol. 21, no. 3, Mar. 1950, pp. 232-237.

35. Cole, J.D.: Twenty Years of Transonic Flow. AIAA Paper 69-659, June 1969. (Boeing Document D1-82-0878).

36. Newman, P.A.; and Allison, D.O.: Annotated Bibliography on Transonic Flow Theory. NASA TM X-2363, 1971.

37. Yoshihara, Y.: A Survey of Computational Methods for 2D and 3D Transonic Flows With Shocks. Advances in Numerical Fluid Dynamics, AGARD-LS-64, 1973, pp. 6-1 to 6-35.

38. Ballhaus, W.F.: Some Recent Progress in Transonic Flow Computations. Computational Fluid Dynamics, Vol. 1, VKI Lecture Series-87-VOL-1, von Karman Institute for Fluid Dynamics, Rhode-St-Genese, Belgium, 1976.

39. Jameson, A.: Transonic Flow Calculations. MAE Report 1651, Princeton University, 1983.

40. Magnus, R.; and Yoshihara, H.: Inviscid Transonic Flow Over Airfoils. AIAA J., vol. 8, no. 12, Dec. 1970, pp. 2157-2162.

41. Murman, E.M.; and Cole, J.D.: Calculation of Plane Steady Transonic Flows. AIAA J., vol. 9, no. 1, Jan. 1971, pp. 114-121.

42. Murman, E.M.: Analysis of Embedded Shock Waves Calculated by Relaxation Methods. AIAA Computational Fluid Dynamics Conference, AIAA, 1973, pp. 27-40.

43. Murman, E.M.; and Krupp, J.A.: Solution of the Transonic Potential Equation Using a Mixed Finite Difference System. Numerical Methods in Fluid Dynamics, M. Holt, ed., (Lecture Notes in Physics, Vol. 8), Springer-Verlag, Berlin, 1971, pp. 199-206.

44. Krupp, J.A.; and Murman, E.M.: The Numerical Calculation of Steady Transonic Flows Past Thin Lifting Airfoils and Slender Bodies. AIAA Paper 71-566, June 1971.

45. Murman, E.M.; Bailey, F.R.; and Johnson, M.L.: TSFOIL - A Computer Code for Two-Dimensional Transonic Calculations, Including Wind-Tunnel Wall Effects and Wave-Drag Evaluation. Aerodynamic Analyses Requiring Advanced Computers, Part 1, NASA SP-347, 1975, pp. 769-788.

46. Cole, J.D.: Perturbation Methods in Applied Mathematics. Blaisdell Publishing Co., 1968.

47. Spreiter, J.R.: On Alternative Forms for the Basic Equations of Transonic Flow Theory. J. Aeronaut. Sci., vol. 21, no. 1, Jan. 1954, pp. 70-72.

48. Krupp, J.A.: The Numerical Calculation of Plane Steady Transonic Flows Past Thin Lifting Airfoils. Ph.D. Thesis, University of Washington, 1971.

49. Enqguist, B.; and Osher, S.: Stable and Entropy Satisfying Approximations for Transonic Flow Calculations. Math. Comput., vol. 34, no. 149, Jan. 1980, pp. 45-75.

50. Ballhaus, W.F.; and Steger, J.L.: Implicit Approximat-Factorization Schemes for the Low-Frequency Transonic Equation. NASA TM X-73082, 1975.

51. Douglas, J.: Alternating Direction Methods for Three Space Variables. Numer. Math., vol. 4, 1961, pp. 41-63.

52. Douglas, J.; and Gunn, J.E.: A General Formulation of Alternating Direction Methods Part I. Parabolic and Hyperbolic Problems. Numer. Math., vol. 6, 1964, pp. 428-453.

53. Jameson, A.: Iterative Solution of Transonic Flows Over Airfoils and Wings, Including Flows at Mach 1. Commun. Pure Appl. Math., vol. 27, no. 3, 1974, pp. 283-309.

54. Bisplinghoff, R.L.; Ashley, H.; and Halfman, R.L.: Aeroelasticity. Addison-Wesley Publishing Co., 1955, Chapter 5.

NASA
National Aeronautics and Space Administration

Report Documentation Page

1. Report No.	2. Government Accession No.	3. Recipient's Catalog No.
NASA TM-100163		

4. Title and Subtitle
Numerical Simulation of Subsonic and Transonic Propeller Flow

5. Report Date

6. Performing Organization Code

7. Author(s)
Aaron Snyder

8. Performing Organization Report No.
E-3725

10. Work Unit No.
505-62-21

9. Performing Organization Name and Address
National Aeronautics and Space Administration
Lewis Research Center
Cleveland, Ohio 44135-3191

11. Contract or Grant No.

13. Type of Report and Period Covered
Technical Memorandum

12. Sponsoring Agency Name and Address
National Aeronautics and Space Administration
Washington, D.C. 20546-0001

14. Sponsoring Agency Code

15. Supplementary Notes
This report was a dissertation submitted as partial fulfillment of the requirements of the Doctor of Philosophy Degree in Chemical Engineering to The University of Toledo, Toledo, Ohio in December 1987.

16. Abstract

The numerical simulation of three-dimensional transonic flow about a system of propeller blades is investigated. In particular, it is shown that the use of helical coordinates significantly simplifies the form of the governing equation when the propeller system is assumed to be surrounded by an irrotational flow field of an inviscid fluid. The unsteady small disturbance equation, valid for lightly loaded blades and expressed in helical coordinates, is derived from the general blade-fixed potential equation, given for an arbitrary coordinate system. The use of a coordinate system which inherently adapts to the mean flow results in a disturbance equation requiring relatively few terms to accurately model the physics of the flow. Furthermore, the helical coordinate system presented here is novel in that it is periodic in the circumferential direction while, simultaneously, maintaining orthogonal properties at the mean blade locations. The periodic characteristic allows a complete cascade of blades to be treated, and the orthogonality property affords straightforward treatment of blade boundary conditions. An ADI numerical scheme is used to compute the solution to the steady flow as an asymptotic limit of an unsteady flow. As an example of the method, solutions are presented for subsonic and transonic flow about a 5 percent thick bicircular arc blade of an eight bladed cascade. Both high and low advance ratio cases are computed, and include a lifting as well as nonlifting cases. The nonlifting solutions obtained are compared to solutions from an Euler code.

17. Key Words (Suggested by Author(s))	18. Distribution Statement
Propeller Numerical Transonic	Unclassified - Unlimited Subject Category 02

19. Security Classif. (of this report)	20. Security Classif. (of this page)	21. No of pages	22. Price*
Unclassified	Unclassified	190	A09

NASA FORM 1626 OCT 86

*For sale by the National Technical Information Service, Springfield, Virginia 22161